

The Search for the Emission of a CP-Violating E1
Photon in the $K_L \rightarrow \pi^+ \pi^- \gamma$ Decay

J. Shields

Contents

1	CP Violation and the $K_L \rightarrow \pi^+\pi^-\gamma$ Decay	1
1.1	Introduction and Motivation	1
1.2	Kaon Mixing and CP Violation	2
1.3	The $K_L \rightarrow \pi^+\pi^-\gamma$ Matrix Element	5
1.4	Evaluation of the Matrix Element in an Explicit Reference Frame	9
1.5	The $K_L \rightarrow \pi^+\pi^-\gamma$ Differential Decay Rate	11
2	The KTeV Experiment	14
2.1	Creation of the Neutral Kaon Beam	14
2.1.1	The Primary Proton Beam	17
2.1.2	The NM2 Beamline Enclosure	18
2.1.3	The Vacuum Decay Region	19
2.2	The KTeV Detector	19
2.2.1	The Calorimeter	19
2.2.2	The Magnetic Spectrometer	24
2.2.3	The Trigger Hodoscopes	26
2.2.4	The Hadron Anti	30
2.2.5	The Muon Vetoes	30
2.2.6	The Photon Vetoes	30

3	The KTeV Trigger System	35
3.1	The Level 1 and Level 2 Triggers	36
3.1.1	The Level 1 Trigger Decision	36
3.1.2	The Level 2 Trigger Decision	37
3.2	The Level 3 Trigger	38
4	Event Reconstruction	40
4.1	Track Reconstruction	40
4.1.1	hit pairing	40
4.1.2	Y Track Finding	41
4.1.3	X Track Finding	42
4.1.4	Vertex Determination	42
4.1.5	Track Momentum Determination	43
4.1.6	Neutral Particle Reconstruction	44
5	Data Reduction and Signal Extraction	47
5.1	The Level 1 and 2 Trigger Requirements	47
5.1.1	The Trigger Hodoscope Requirement	48
5.1.2	The DC-OR Requirement	49
5.1.3	The Veto Requirement	50
5.2	The Level 3 Trigger	50
5.3	Data Reduction	51
5.3.1	The Split	51
5.3.2	The Crunch	51
5.4	Signal Extraction	52
5.4.1	Reconstruction Quality Cuts	53
5.4.2	Fiducial and Resolution Cuts	53

5.4.3	Particle Identification and Rejection	54
5.4.4	Kinematic Cuts	56
6	The KTEV Monte Carlo	58
6.1	Kaon Production	58
6.2	Kaon Transport	59
6.3	Kaon Decay Tracing	60
6.4	Drift Chamber Simulation	60
6.5	Calorimeter Simulation	61
6.6	Accidental Activity	63
6.7	Trigger Simulation	64
7	Likelihood Extraction of Matrix Element Parameters	66
7.1	A Brief Overview of Likelihood Analysis	66
7.2	The Likelihood Function for a Generalized Decay	67
7.3	Application of the Likelihood Function to $K_L \rightarrow \pi^+\pi^-\gamma$	70
7.3.1	The $K_L \rightarrow \pi^+\pi^-\gamma$ Likelihood Maximization Procedure	70
7.3.2	Determination of the Baseline Monte Carlo Size	70
7.3.3	Extraction Procedure for the \tilde{g}_{M1} and $\frac{a_1}{a_2}$ Best Fit Values	73
8	Extraction of Fit Parameters with Statistical Uncertainty	89
8.1	Extraction of the Best-fit Parameters	89
8.2	Determination of the statistical G_{E1} Upper Limit	90
8.3	Verification of the Likelihood Fit Procedure	94
9	Systematics Studies	102
9.1	Systematic Uncertainty of the Likelihood Fit Program due to Different Baseline Monte Carlos	102

9.2	Systematic Error in the Kaon Momentum Slope	104
9.3	Systematic Error Due to Choice of Physics Analysis Cuts	106
9.4	Background Effects	109
9.4.1	Fraction of Background in the $K_L \rightarrow \pi^+\pi^-\gamma$ Event Sample	120
9.4.2	Effect of the Background on the Final Fit Result	120
9.4.3	Contributions to the Background	121
9.5	Effects of Variations over Time	124
9.6	Effects of K_S Contamination	126
9.7	Uncertainties on Constant Parameters Input In the Matrix Element	127
9.7.1	Effect of the Uncertainty in η_{+-}	128
9.7.2	Effect of the Uncertainty in the Pion Phase Shifts	128
9.8	Uncertainty in Event Reconstruction Resolution	129
9.9	Summary of Systematic Errors	130
10	Conclusion	133
A	Expressing the $\pi^+\pi^-$ Invariant Mass as a Function of the Phase	
	Space Variable ω	135
B	The Statistical Error on a Correlated Sample	137
B.0.1	Expressing the Parameter Shift in Terms of Statistically In- dependent Samples	138
B.0.2	Calculation of the Error on the Shift	139

List of Figures

1.1	Feynman diagrams of the processes contributing to the $K_L \rightarrow \pi^+\pi^-\gamma$ decay. Both the E1 and M1 decay contributions are direct emission processes.	7
2.1	Three-dimensional cutaway of the KTeV Detector. Components labeled “E799” were not used in this analysis	15
2.2	The E832 configuration of the KTeV Detector (plan view)	16
2.3	The NM2 beam enclosure	20
2.4	Schematic of the KTeV CsI Calorimeter	23
2.5	Top (y) view schematic of the field and sense wire arrangement within a drift chamber.	27
2.6	Close-up view of a charged particle passing through a pair of hexagonal drift chamber cells. The thin lines represent the drift paths of ionization electrons toward the sense wires.	28
2.7	Schematic of the V and V’ Trigger Hodoscope Plane Configurations	29
2.8	Schematic of Muon Trigger Planes. Dashed lines indicate the 1 cm counter overlaps in MU2	31
2.9	y view of the KTeV detector downstream of the CsI calorimeter	32
2.10	Schematics of typical photon veto detectors. RC10 is shown on the left, SA4 on the right	33

2.11	Schematic of the CA around the calorimeter beam hole	34
4.1	Calorimeter track and photon clusters for a typical $K_L \rightarrow \pi^+\pi^-\gamma$ event	46
5.1	Definition of the PP0KINE kinematic variable. It is defined as the square of the π^0 longitudinal momentum in the frame in which the longitudinal $\pi^+\pi^-$ momentum is zero.	56
7.1	$\frac{\sigma_{MC}^2}{\sigma_{TOT}^2}$ vs Q	72
7.2	$\pi^+\pi^-$ combined momentum distribution (data, Monte Carlo). Upper plot: $N_{events}/(1.8 \text{ GeV})$ vs. $P_{\pi^+\pi^-}$ (GeV/c). Crosses repre- sent data. Lower plot: Data/MC ratio vs. $P_{\pi^+\pi^-}$ (GeV/c).	75
7.3	$\pi^+\pi^-$ invariant mass distribution (data, Monte Carlo). Upper plot: $N_{events}/(2.5 \text{ MeV}/c)$ vs. $M_{\pi^+\pi^-}$ (GeV). Crosses repre- sent data. Lower plot: Data/MC ratio vs. $M_{\pi^+\pi^-}$ (GeV).	76
7.4	$\pi^+\pi^-\pi^0$ kinematic (“pp0kine”) distribution (data, Monte Carlo). Upper plot: $N_{events}/(6 \times 10^{-4}(\text{GeV}/c)^2)$ vs. pp0kine $(\text{GeV}/c)^2$. Crosses represent data. Lower plot: Data/MC ratio vs. pp0kine $(\text{GeV}/c)^2$	77
7.5	Two track hit illumination for Drift Chamber 1 (data, MC). Upper plot: $N_{events}/(2 \text{ cm})$ vs. DC y-intercept (m). Crosses rep- resent data. Lower plot: Data/MC ratio vs. DC y-intercept (m).	78

- 7.6 LAB frame photon energy distribution (data, Monte Carlo).
Upper plot: $N_{events}/(0.4 \text{ GeV})$ vs. E_γ (GeV). Crosses represent data.
Lower plot: Data/MC ratio vs. E_γ (GeV). 79
- 7.7 Photon X position in the Calorimeter (data, Monte Carlo).
Upper plot: N_{events}/cm vs. $|X|$ (m). Crosses represent data.
Lower plot: Data/MC ratio vs. $|X|$ (m). 80
- 7.8 Photon Y position in the Calorimeter (data, Monte Carlo).
Upper plot: N_{events}/cm vs. $|Y|$ (m). Crosses represent data.
Lower plot: Data/MC ratio vs. $|Y|$ (m). 81
- 7.9 Track-photon separation in the calorimeter (data, Monte Carlo).
Upper plot: $N_{events}/(1.3 \text{ cm})$ vs. separation distance (m). Crosses are data.
Lower plot: Data/MC ratio vs. separation distance (m). 82
- 7.10 Track separation in the calorimeter (data, Monte Carlo).
Upper plot: $N_{events}/(2 \text{ cm})$ vs. track separation (m). Crosses are data.
Lower plot: Data/MC ratio vs. track separation (m). 83
- 7.11 Vertex X position (data, Monte Carlo).
Upper plot: $N_{events}/(0.4 \text{ cm})$ vs. Vertex X (m). Crosses represent data.
Lower plot: Data/MC ratio vs. Vertex X (m). 84
- 7.12 Vertex Y position (data, Monte Carlo).
Upper plot: N_{events}/cm vs. Vertex Y (m). Crosses represent data.
Lower plot: Data/MC ratio vs. Vertex Y (m). 85

- 7.13 Vertex Z position (data, Monte Carlo).
- Upper plot:** $N_{events}/(0.9 \text{ cm})$ vs. Vertex Z (m). Crosses represent data.
- Lower plot:** Data/MC ratio vs. Vertex Z (m). 86
- 7.14 Kaon transverse momentum squared (data, Monte Carlo).
- Upper plot:** $N_{events}/(3 \times 10^{-6}(\text{GeV}/c)^2)$ vs. $p_T^2 (\text{GeV}/c)^2$. Crosses are data.
- Lower plot:** Data/MC ratio vs. $p_T^2 (\text{GeV}/c)^2$ 87
- 7.15 $\pi^+\pi^-\gamma$ combined momentum distribution (data, Monte Carlo).
- Upper plot:** $N_{events}/(1.8 \text{ GeV})$ vs. $P_{\pi^+\pi^-\gamma} (\text{GeV})$. Crosses represent data.
- Lower plot:** Data/MC ratio vs. $P_{\pi^+\pi^-\gamma} (\text{GeV})$ 88
- 8.1 A scatterplot representing the 2-D cross-section (\tilde{g}_{M1} vs $\frac{a_1}{a_2}$) of the 3-D "error ellipsoid" defined by parameter value combinations that produce log likelihoods within 0.5 of the maximum. An ellipse representing the approximate contour is drawn in for clarity. 91
- 8.2 Distribution of phase space variable ω (data, Monte Carlo).
- Upper plot:** $N_{events}/(1.8 \text{ MeV})$ vs. $\omega (\text{GeV})$. Crosses represent data.
- Lower plot:** Data/MC ratio vs. $\omega (\text{GeV})$ 92
- 8.3 Distribution of phase space variable $\cos\theta$ (data, Monte Carlo).
- Upper plot:** $N_{events}/0.02$ vs. $\cos\theta$. Crosses represent data.
- Lower plot:** Data/MC ratio vs. $\cos\theta$ 93

8.4	Feldman and Cousins upper limit plot of Measured G_{E1} vs Generated G_{E1} at 90% CL . Error bars plotted on individual points are 1.28σ in width.	95
8.5	Deviation (in σ) between input and measured values of \tilde{g}_{M1} for 18 data-sized trial Monte Carlos. Plot is Sigma Deviation vs. Monte Carlo file number (1-18).	98
8.6	Deviation (in σ) between input and measured values of $\frac{a_1}{a_2}$ for 18 data-sized trial Monte Carlos. Plot is Sigma Deviation vs. Monte Carlo file number (1-18).	99
8.7	Deviation (in σ) between input and measured values of G_{E1} for 18 data-sized trial Monte Carlos. Plot is Sigma Deviation vs. Monte Carlo file number (1-18).	100
9.1	$\pi^+\pi^-\gamma$ combined momentum distribution (data, Monte Carlo). Upper plot: $N_{events}/(1.8 \text{ GeV})$ vs. $P_{\pi^+\pi^-\gamma}$ (GeV). Crosses represent data. Lower plot: Data/MC ratio vs. $P_{\pi^+\pi^-\gamma}$ (GeV).	105
9.2	Fit parameter shift S vs. Fusion χ^2 Cut Selection (from top to bottom): \tilde{g}_{M1} , $\frac{a_1}{a_2}$, G_{E1} Dotted lines are nominal data stat errors (table 8.1), included for scale.	110
9.3	Fit parameter shift S vs. CsI Inner Fiducial Cut (from top to bottom): \tilde{g}_{M1} , $\frac{a_1}{a_2}$, G_{E1} Dotted lines are nominal data stat errors (table 8.1), included for scale.	111

- 9.4 Fit parameter shift S vs. CsI Outer Fiducial Cut
 (from top to bottom): \tilde{g}_{M1} , $\frac{a_1}{a_2}$, G_{E1}
 Dotted lines are nominal data stat errors (table 8.1), included for
 scale. 112
- 9.5 Fit parameter shift S vs. $P_{transverse}^2$ Cut $(GeV/c)^2$
 (from top to bottom): \tilde{g}_{M1} , $\frac{a_1}{a_2}$, G_{E1}
 Dotted lines are nominal data stat errors (table 8.1), included for
 scale. 113
- 9.6 Fit parameter shift S vs. PP0KINE Cut $(GeV/c)^2$
 (from top to bottom): \tilde{g}_{M1} , $\frac{a_1}{a_2}$, G_{E1}
 Dotted lines are nominal data stat errors (table 8.1), included for
 scale. 114
- 9.7 Fit parameter shift S vs. Kaon Momentum Cut (GeV)
 (from top to bottom): \tilde{g}_{M1} , $\frac{a_1}{a_2}$, G_{E1}
 Dotted lines are nominal data stat errors (table 8.1), included for
 scale. 115
- 9.8 Fit parameter shift S vs. Track-Photon Separation Cut (meters)
 (from top to bottom): \tilde{g}_{M1} , $\frac{a_1}{a_2}$, G_{E1}
 Dotted lines are nominal data stat errors (table 8.1), included for
 scale. 116
- 9.9 Fit parameter shift S vs. Vertex Z Cut (meters)
 (from top to bottom): \tilde{g}_{M1} , $\frac{a_1}{a_2}$, G_{E1}
 Dotted lines are nominal data stat errors (table 8.1), included for
 scale. 117

9.10 Fit parameter shift S vs. Lab Photon Energy Cut (GeV)

(from top to bottom): \tilde{g}_{M1} , $\frac{a_1}{a_2}$, G_{E1} Dotted lines are nominal data stat errors (table 8.1), included for
scale. 118

9.11 Fit parameter shift S vs. Pion Energy/Momentum Cut (c)

(from top to bottom): \tilde{g}_{M1} , $\frac{a_1}{a_2}$, G_{E1} Dotted lines are nominal data stat errors (table 8.1), included for
scale. 119

9.12 Left wing and right wing exponential fits to data.

Plot is $\log(N_{events}/0.8 \text{ MeV})$ vs. $M_{\pi^+\pi^-\gamma}$ (GeV).

The nominal kaon mass cuts are inhibited. 122

9.13 Variation of Parameter Values Over the Course of the 1997 Run . . 125

List of Tables

2.1	z positions and dimensions of KTEV spectrometer	25
8.1	Best-fit Parameter Values	90
8.2	Generated parameter values for the 18 trial Monte Carlo files used in the initial likelihood fitter verification study. The absolute difference between the generated and measured values of these test Monte Carlos are plotted in figures 8.5through 8.7. . .	96
8.3	Comparison of input & generated values at 4 different selections of input values.	101
8.4	Sigma Deviation of Monte Carlo sample sets described in table 8.3.	101
9.1	Likelihood fit results for data fit by four Monte Carlo files generated at “nominal” input values that differ <u>only</u> by a random seed.	103
9.2	Shift in fit parameter values due to the change in the baseline Monte Carlo used in the likelihood fit.	103
9.3	Systematic error on the kaon momentum slope	106
9.4	Number of events for each kaon momentum and vertex Z cut variation.	109
9.5	Effects of modified ΔS procedure on P_{kaon} and vertex Z	109
9.6	Systematic errors assigned from the variation of cuts	120
9.7	Effect of the addition of 800 wing events to the final data sample . .	121
9.8	Summary of kaon contamination study results	127

9.9	Effect of the uncertainty of Monte Carlo input constants on the final result	130
9.10	Deviation between generated and reconstructed parameter values for a given Monte Carlo file. Monte Carlo sample sets are the same as those used in table 8.3.	131
9.11	Statistical errors on the four trial Monte Carlo sets from table 9.10	131
9.12	Summary of Systematic Errors	132

Abstract

A search for the CP-violating electric dipole (E1) direct emission contribution to the $K_L \rightarrow \pi^+\pi^-\gamma$ decay is performed using data from the 1997 KTeV/E832 experiment. Because the $K_L \rightarrow \pi^+\pi^-\gamma$ decay mode is massively dominated by the CP-violating inner bremsstrahlung (IB) and the CP-conserving magnetic dipole (M1) direct emission processes, previous analyses have neglected the E1 contribution. Therefore, this measurement is the first attempt to directly quantify the size of the E1 decay process. This E1 transition is one of the very few CP-violating processes that is accessible to experiment and, in principle, will produce new insights into the structure of the neutral kaon.

The result of this analysis is that the E1 contribution is below the threshold of sensitivity, and therefore an upper bound of $|g_{E1}| < 0.14$ (90% CL) is reported.

In the process of obtaining this upper limit, high resolution measurements of fit parameters (\tilde{g}_{M1} and $\frac{a_1}{a_2}$) associated with the size and shape of the M1 direct emission peak are also extracted. The fit results for these parameters:

$$\tilde{g}_{M1} = 1.229 \pm 0.035 \text{ (stat)} \pm 0.087 \text{ (syst)}$$

$$\frac{a_1}{a_2} = -0.733 \pm 0.007 \text{ (stat)} \pm 0.014 \text{ (syst)}$$

are in strong agreement with previous measurements.

Chapter 1

CP Violation and the $K_L \rightarrow \pi^+ \pi^- \gamma$ Decay

1.1 Introduction and Motivation

The field of high energy physics is a relatively young science. Although it is technically said to have begun with the discovery of the electron at the end of the 19th century, the field of particle physics did not really take off until the advent of particle accelerators in the 1950s.

Suddenly, a veritable menagerie of particles were being produced, and it proved quite challenging to make sense of them all. One powerful method of grouping these seemingly-disparate particles was to exploit the symmetries (which, by Noether's theorem, corresponded to physical conservation laws) that they obeyed.

As the field matured, theoretical and experimental efforts shifted from focusing on the large groups of particles that did obey the symmetries to focusing on those few and far between specimens that apparently did not, since it was clear that such particles held the key to newer and better understanding.

Two particularly important symmetries during this time were charge conjugation (C) and parity (P). Charge conjugation transformed a particle into its anti-particle "partner"; for example, the transformation from an electron to a positron.

Parity performed the spatial inversion transformation $\vec{X} \rightarrow -\vec{X}$ and was often referred to as the “mirror inversion” transformation.

Although weak decays were known to violate these symmetries individually, it was originally thought that the combination of C and P together was a valid symmetry. This was dramatically disproved in the 1964 experiment by Christenson, Cronin, Fitch, and Turley [1] that eventually lead to the important idea of kaon mixing¹. Insights such as these would ultimately culminate, in the early 1970s, into the so-called “Standard Model” of high energy physics.

However, for all its many successes, the Standard Model is still not the entire story. Although it has now been 40 years since the Cronin and Fitch experiment, the mystery of CP violation has yet to be fully explained. As a result, the study of CP violation continues to be one of the most fertile grounds to search for new physics beyond the Standard Model. Moreover, CP violation appears to have extremely profound cosmological consequences, as it is a leading candidate to help explain the observed matter, anti-matter disparity in the universe.

1.2 Kaon Mixing and CP Violation

The strong force eigenstates of the K meson are given as

$$|K^0\rangle = |\bar{s}d\rangle \quad (1.1)$$

$$|\bar{K}^0\rangle = |\bar{d}s\rangle \quad (1.2)$$

where K^0 is the $S = +1$ strangeness eigenstate and \bar{K}^0 is the $S = -1$ eigenstate. However, it was noted experimentally that the K^0 decayed with two different lifetimes:

$$\tau[K^0_{(short)} \rightarrow 2\pi] = 0.9 \times 10^{-10} \text{ sec}$$

¹this will be described in more detail later in the chapter

$$\tau[K_{(long)}^0 \rightarrow 3\pi] = 0.5 \times 10^{-7} \text{ sec}$$

In other words, the strong interaction K^0 particle suddenly seemed to become two separate particles (defined as K_1 and K_2) under weak interaction decays [2].

The fact that the \bar{K}^0 particle behaved similarly led Gell-Mann [3] to realize that the K_1 and K_2 could be written as CP eigenstates if they were comprised of admixtures of K^0 and \bar{K}^0 states. Specifically:

$$|K_1 \rangle = \frac{1}{\sqrt{2}}(|K^0 \rangle - |\bar{K}^0 \rangle) \quad , \quad CP|K_1 \rangle = (+1)|K_1 \rangle \quad (1.3)$$

$$|K_2 \rangle = \frac{1}{\sqrt{2}}(|K^0 \rangle + |\bar{K}^0 \rangle) \quad , \quad CP|K_2 \rangle = (-1)|K_2 \rangle \quad (1.4)$$

If CP were a perfect symmetry, the decays $K_1 \rightarrow 2\pi$ and $K_2 \rightarrow 3\pi$ would be allowed and $K_1 \rightarrow 3\pi$ and $K_2 \rightarrow 2\pi$ would be forbidden.

When a landmark experiment [1] demonstrated that the long-lived kaon violated CP conservation by decaying into a two pion state, it became clear that even the K_1 and K_2 states were not sufficient to perfectly describe the neutral kaon system. Instead, new states $|\psi(t) \rangle$ should be described as

$$|\psi(t) \rangle = A(t)|K^0 \rangle + B(t)|\bar{K}^0 \rangle \quad (1.5)$$

which, as we shall see allows for the possibility of mixing between the K_1 and K_2 states. Using a matrix formulation in which

$$|K^0 \rangle = \begin{pmatrix} 1 \\ 0 \end{pmatrix} \quad |\bar{K}^0 \rangle = \begin{pmatrix} 0 \\ 1 \end{pmatrix} \quad (1.6)$$

we can express the final state $|\psi(t) \rangle$ as

$$|\psi(t) \rangle = \begin{pmatrix} A(t) \\ B(t) \end{pmatrix} \quad (1.7)$$

The non-Hermitian net effective Hamiltonian for this system H_{eff} is given by

$$H_{eff} = H_0 + H_{Weak} \quad (1.8)$$

where H_0 is the (strangeness conserving) strong and electromagnetic Hamiltonian and H_{Weak} is the weak decay Hamiltonian (which violates strangeness by $|\Delta S| = 2$) [4]. Since H_{eff} is not Hermitian, it can be expressed as a linear combination of two separate Hermitian matrices: a “mass matrix” M and a “decay matrix” Γ [5].

$$H_{eff} = M - \frac{i}{2}\Gamma = \begin{pmatrix} M_{11} - \frac{i}{2}\Gamma_{11} & M_{12} - \frac{i}{2}\Gamma_{12} \\ M_{21} - \frac{i}{2}\Gamma_{21} & M_{22} - \frac{i}{2}\Gamma_{22} \end{pmatrix} \quad (1.9)$$

CPT invariance of H_{eff} ² implies that

$$\begin{aligned} M_{11} &= M_{22} \equiv M_0 \\ \Gamma_{11} &= \Gamma_{22} \equiv \Gamma_0 \end{aligned} \quad (1.10)$$

where $M_0 = M_{K^0} = M_{\bar{K}^0}$, and Γ_0 is identified with the decay width of K^0 and \bar{K}^0 . In addition, since M and Γ are Hermitian by construction, then M_0 and Γ_0 are both real and $M_{21} = M_{12}^*$ and $\Gamma_{21} = \Gamma_{12}^*$. Thus equation (1.9) becomes

$$H_{eff} = \begin{pmatrix} M_0 - \frac{i}{2}\Gamma_0 & M_{12} - \frac{i}{2}\Gamma_{12} \\ M_{12}^* - \frac{i}{2}\Gamma_{12}^* & M_0 - \frac{i}{2}\Gamma_0 \end{pmatrix} \quad (1.11)$$

Diagonalization of (1.11) immediately gives the explicit form of the physically observed $|K_S\rangle$ and $|K_L\rangle$ states as

$$|K_L\rangle = \frac{1}{\sqrt{1+|\epsilon|^2}} \left(\frac{|K^0\rangle + |\bar{K}^0\rangle}{\sqrt{2}} + \epsilon \frac{|K^0\rangle - |\bar{K}^0\rangle}{\sqrt{2}} \right) \quad (1.12)$$

$$|K_S\rangle = \frac{1}{\sqrt{1+|\epsilon|^2}} \left(\frac{|K^0\rangle - |\bar{K}^0\rangle}{\sqrt{2}} + \epsilon \frac{|K^0\rangle + |\bar{K}^0\rangle}{\sqrt{2}} \right) \quad (1.13)$$

$$\text{where } \epsilon = \frac{\sqrt{M_{12} - \frac{i}{2}\Gamma_{12}} - \sqrt{M_{12}^* - \frac{i}{2}\Gamma_{12}^*}}{\sqrt{M_{12} - \frac{i}{2}\Gamma_{12}} + \sqrt{M_{12}^* - \frac{i}{2}\Gamma_{12}^*}} \quad (1.14)$$

The appellations “ K_L ” and “ K_S ” are derived from the differing decay lifetimes of the two states. K_L is the “long-lived” ($\tau_L \approx 5 \cdot 10^{-8}$ s) kaon, and K_S is the “short-lived” ($\tau_S \approx 9 \cdot 10^{-11}$ s) kaon.

²It is possible to expand the derivation to account for CPT-violating effects, but for simplicity we will confine our discussion to assuming CPT conservation.

$|K_L \rangle$ and $|K_S \rangle$ can also be expressed in terms of the CP eigenstates as

$$|K_L \rangle = \frac{1}{\sqrt{1 + |\epsilon|^2}} (|K_2 \rangle + \epsilon |K_1 \rangle) \quad (1.15)$$

$$|K_S \rangle = \frac{1}{\sqrt{1 + |\epsilon|^2}} (|K_2 \rangle - \epsilon |K_1 \rangle) \quad (1.16)$$

Note that the above equations explicitly demonstrate CP violation in K_L and K_S . If CP were conserved, then all of the M and Γ matrix elements would be real (i.e. $M_{12}^* = M_{12}$ and $\Gamma_{12}^* = \Gamma_{12}$), and ϵ would vanish in equation (1.14). Hence, $|K_S \rangle$ would then exactly equal $|K_1 \rangle$, and $|K_L \rangle$ would exactly equal $|K_2 \rangle$. In practice, however, ϵ is small ($\sim 2 \cdot 10^{-3}$), but definitely non-zero, thus allowing the CP-violating $K_S \rightarrow 3\pi$ and $K_L \rightarrow 2\pi$ decays to be observed.

Finally, for completeness, it is also important to note that all CP-violation discussed in this chapter is the *indirect* CP-violation due to $|K_1 \rangle$ and $|K_2 \rangle$ mixing. However, there is also a separate phenomenon known as *direct* CP-violation in which the “forbidden” $K_1 \rightarrow 3\pi$ and $K_2 \rightarrow 2\pi$ decays explicitly occur. In this particular decay, the direct CP violation contributions are expected to be much smaller than the indirect contributions. As a result, any such direct CP violation contributions are expected to be far beyond the sensitivity of this measurement and will henceforth be neglected.

1.3 The $K_L \rightarrow \pi^+ \pi^- \gamma$ Matrix Element

The decay amplitudes for the decay $K_L(P) \rightarrow \pi^+(p^+) \pi^-(p^-) \gamma(k, \epsilon)$ can be classified [6] into 3 groups

$$\frac{(p^+ \cdot \varepsilon)(p^- \cdot k) - (p^- \cdot \varepsilon)(p^+ \cdot k)}{(p^+ \cdot k)(p^- \cdot k)} \quad (1.17a)$$

$$\epsilon_{\mu\nu\rho\sigma} p_+^\rho p_-^\sigma k^\nu \varepsilon^\mu \quad (1.17b)$$

$$(p^+ \cdot \varepsilon)(p^- \cdot k) - (p^- \cdot \varepsilon)(p^+ \cdot k) \quad (1.17c)$$

where ε is the photon polarization vector, and P , p_+ , p_- , and k are the 4-vector momenta of the kaon, π^+ , π^- , and photon, respectively.

These 3 forms (and their equivalents after kinematic substitution) are the only possible ones that, up to third order in momenta, satisfy gauge invariance. Forms 1.17a and 1.17c correspond to first order electric transitions, while 1.17b corresponds to first order magnetic transitions. From this, the complete matrix element amplitude can be written [7, 8]

$$\mathcal{M} = \frac{ef_s \varepsilon^\mu}{M_K^4} (I_\mu + \overline{G}_\mu + M_\mu) \quad (1.18)$$

where

$$I_\mu = E_{IB} [(p_- \cdot k) p_{+\mu} - (p_+ \cdot k) p_{-\mu}] \quad (1.19)$$

$$\overline{G}_\mu = g_{E1} [(P \cdot k) p_{+\mu} - (p_+ \cdot k) P_\mu] \quad (1.20)$$

$$M_\mu = g_{M1} \epsilon_{\mu\nu\rho\sigma} k^\nu p_+^\rho p_-^\sigma \quad (1.21)$$

$$E_{IB} = \frac{\eta_\pm M_K^4 f_S}{(p_+ \cdot k)(p_- \cdot k) |f_S|} \quad (1.22)$$

where f_s is the $K_S \rightarrow \pi^+ \pi^-$ coupling constant, and η_{+-} is a CP-violation parameter related to the quantity ϵ defined in equation 1.14 by³

$$\eta_{+-} = \epsilon \left(1 + \frac{\epsilon'}{\epsilon} \right) \approx \epsilon \quad (1.23)$$

³For completeness, the quantity ϵ' is the direct CP violation counterpart to ϵ , where $\epsilon' \sim 10^{-4}\epsilon$

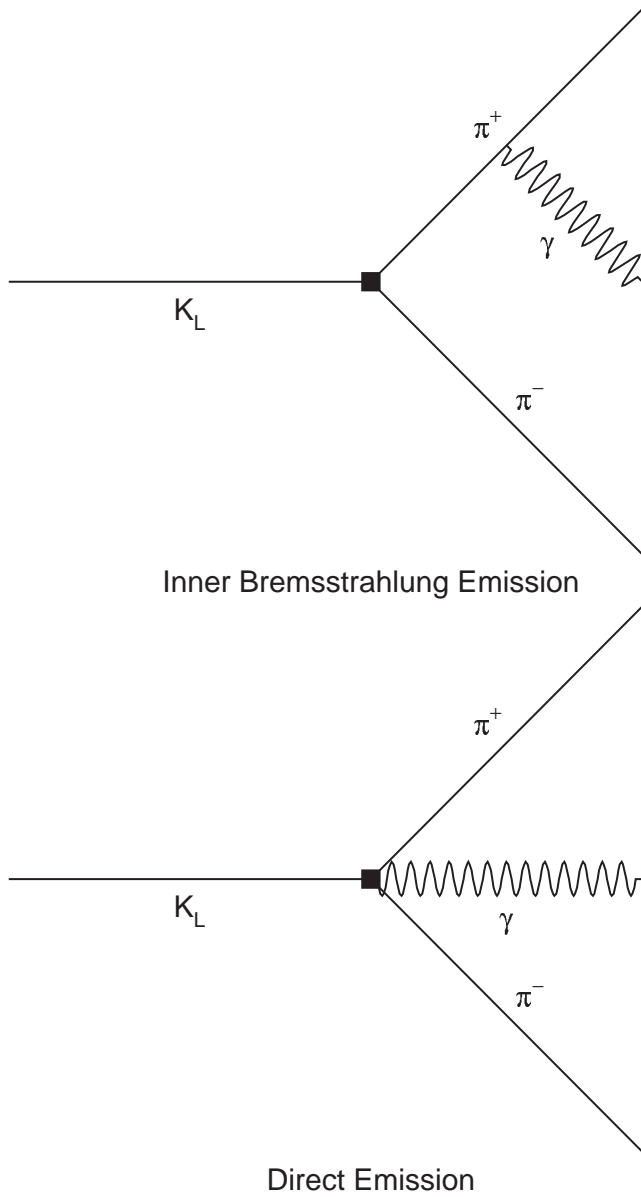


Figure 1.1: Feynman diagrams of the processes contributing to the $K_L \rightarrow \pi^+\pi^-\gamma$ decay. Both the E1 and M1 decay contributions are direct emission processes.

We can reexpress The E1 term, \overline{G}_μ , using $P = p_+ + p_- + k$ and noting that $k^2 = M_\gamma^2 = 0$, which gives

$$\overline{G}_\mu = G_\mu + H_\mu \quad (1.24)$$

where

$$G_\mu \equiv g_{E1}[(p_- \cdot k)p_{+\mu} - (p_+ \cdot k)p_{-\mu}] \quad (1.25)$$

$$H_\mu \equiv g_{E1}(p_+ \cdot k)k_\mu \quad (1.26)$$

However, since it can easily be shown⁴ that

$$I^\mu H_\mu = G^\mu H_\mu = M^\mu H_\mu = H^\mu H_\mu = 0 \quad (1.27)$$

it implies that the H_μ term makes no contribution to the final decay rate and hence we can set $H_\mu = 0$ in equation 1.24 with no loss of generality. Therefore we will use G_μ in place of \overline{G}_μ for the remainder of the derivation.

Note that the G_μ E1 term now manifestly has the same form as the (E0) inner bremsstrahlung term (I_μ) defined in equation 1.19. This allows us to now conveniently reexpress the matrix element in terms of an electric (J_μ) and a magnetic (M_μ) component

$$\mathcal{M} = \frac{ef_s \varepsilon^\mu}{M_K^4} (J_\mu + M_\mu) \quad (1.28)$$

where

$$J_\mu \equiv I_\mu + G_\mu = (E_{IB} + g_{E1})[(p_- \cdot k)p_{+\mu} - (p_+ \cdot k)p_{-\mu}] \quad (1.29)$$

Thus the matrix element squared can be written

$$|\mathcal{M}|^2 = \left| \frac{ef_s}{M_K^4} \right|^2 \sum_\varepsilon [\varepsilon^\mu (J_\mu + M_\mu)]^* [\varepsilon^\nu (J_\nu + M_\nu)] \quad (1.30)$$

⁴see next section

Using the Ward Identity $\sum_{\epsilon} \epsilon^{\mu*} \epsilon^{\nu} \rightarrow -g_{\mu\nu}$ to sum over the polarizations [9] and recalling that $J_{\mu} M^{\mu} = 0$, the expression becomes

$$|\mathcal{M}|^2 = \left| \frac{ef_s}{M_K^4} \right|^2 (|J_{\mu}|^2 + |M_{\mu}|^2) \quad (1.31)$$

1.4 Evaluation of the Matrix Element in an Explicit Reference Frame

In order to calculate the differential decay rate, $|\mathcal{M}|^2$ has been evaluated in terms of the two kinematic variables for this decay: ω (the photon energy in the $\pi^+\pi^-\gamma$ center of mass frame) and θ (the angle between the photon and the π^+ in the $\pi^+\pi^-$ center of mass).

The choice of the $\pi^+\pi^-$ center of mass frame, in which $\vec{p}_+ + \vec{p}_- \equiv 0$, and the alignment of the z-axis with the momentum of the original kaon, is particularly convenient for evaluating the decay rate. With the further choice of coordinates such that the X-Z plane aligns with the \vec{p}_+ momentum vector, many of the components⁵ of vectors p_+^i , p_-^i , and k^i are zero. Specifically,

$$k^1 = k^2 = p_+^2 = p_-^2 = 0 \quad (1.32)$$

In addition, since $|\vec{p}_+| = |\vec{p}_-|$ in this frame, the π^+ and π^- energies are related by

$$E_+ = E_- = \frac{1}{2} M_{\pi\pi} \quad (1.33)$$

Moreover, if we evaluate the 4-vector invariant $P \cdot k$ in both the kaon and $\pi^+\pi^-$ center of mass frames, we get

⁵where $i = (1,2,3)$ follows the usual convention of (x, y, z)

$$P \cdot k = M_K \omega \quad (1.34)$$

for the kaon CM frame and

$$P \cdot k = M_{\pi\pi} E_\gamma \quad (1.35)$$

for the $\pi^+\pi^-$ CM frame.

Setting 1.34 equal to 1.35, we immediately arrive at the following expression for the photon energy (E_γ) in the $\pi^+\pi^-$ CM frame:

$$E_\gamma = \frac{\omega M_K}{M_{\pi\pi}} \quad (1.36)$$

Combining equation 1.36 with the fact that e.g.

$$|\vec{p}_+| = \sqrt{E_+^2 - M_+^2} = \left[\left(\frac{M_{\pi\pi}}{2} \right)^2 - M_\pi^2 \right]^{\frac{1}{2}} = \frac{\beta M_{\pi\pi}}{2} \quad (1.37)$$

we can write the invariant dot products $p_\pm \cdot k$ in equation 1.29 as

$$p_\pm \cdot k = \left(\frac{M_K \omega}{2} \right) (1 \mp \beta \cos \theta) \quad (1.38)$$

where

$$\beta \equiv \left(1 - \frac{4M_\pi^2}{M_{\pi\pi}^2} \right)^2 = \left(1 - \frac{4M_\pi^2}{M_K^2 - 2\omega M_K} \right)^2 \quad (1.39)$$

The electric term can then be expressed

$$J_\mu = (E_{IB} + g_{E1}) \left(\frac{M_K \omega}{2} \right) [(1 + \beta \cos \theta) p_{+\mu} - (1 - \beta \cos \theta) p_{-\mu}] \quad (1.40)$$

where

$$E_{IB} = \frac{f_s}{|f_s|} \left(\frac{2M_K}{\omega} \right)^2 \frac{\eta_{+-}}{1 - \beta^2 \cos^2 \theta} \quad (1.41)$$

For the magnetic component, we expand the summation over k^ν in equation 1.21 to obtain

$$M_\mu = g_{M1} p_+^\rho p_-^\sigma (\epsilon_{\mu 0 \rho \sigma} k^0 + \epsilon_{\mu 1 \rho \sigma} k^1 + \epsilon_{\mu 2 \rho \sigma} k^2 + \epsilon_{\mu 3 \rho \sigma} k^3) \quad (1.42)$$

From equation 1.32, we know that the second and third terms are both zero. In addition, since $k^0 = k^3 = E_\gamma$, we can rewrite equation 1.42 as

$$M_\mu = g_{M1} E_\gamma p_+^\rho p_-^\sigma (\epsilon_{\mu 0 \rho \sigma} + \epsilon_{\mu 3 \rho \sigma}) \quad (1.43)$$

Performing a similar expansion over e.g. p_+^ρ and exploiting the properties⁶ of the totally anti-symmetric tensor $\epsilon_{\mu\nu\rho\sigma}$, equation 1.42 reduces to the extremely compact form

$$M_\mu = (2g_{m1} E_\gamma p_+^0 p_+^1) \bar{\delta}_\mu^2 \quad (1.44)$$

where $\bar{\delta}_\beta^\alpha$ is the Kronecker delta function⁷.

Note that equations (1.32) and (1.44), along with the fact that $k \cdot k = 0$ in any frame make it manifestly apparent that our assertion (1.27) in the previous section must hold true.

1.5 The $K_L \rightarrow \pi^+ \pi^- \gamma$ Differential Decay Rate

The differential decay rate formula for a general 3-body decay with phase space variables z_1 and z_2 is given by [10]

$$\frac{d\Gamma}{dz_1 dz_2} = \left(\frac{1}{32\pi^3} \right) |\mathcal{M}(z_1, z_2)|^2 \quad (1.45)$$

Substituting ω and $\cos \theta$ for z_1 and z_2 , this becomes

$$\frac{d\Gamma}{d\omega d \cos \theta} = \left(\frac{1}{32\pi^3} \right) |\mathcal{M}(\omega, \cos \theta)|^2 \quad (1.46)$$

⁶for example the fact that: $\epsilon_{\mu 30\sigma} = -\epsilon_{\mu 03\sigma} = \bar{\delta}_\mu^1 \bar{\delta}_\sigma^2 - \bar{\delta}_\mu^2 \bar{\delta}_\sigma^1$

⁷Note the use of the bar over the “ δ ” of the Kronecker delta function, in order to distinguish it from the pion phase shift angles δ_0^0 and δ_1^1 in the next section.

Inserting equation 1.31 in for $|\mathcal{M}(\omega, \cos \theta)|^2$, this becomes

$$\frac{d\Gamma}{d\omega d \cos \theta} = \left(\frac{1}{32\pi^3} \right) \left| \frac{ef_s}{M_K^4} \right|^2 (|J_\mu|^2 + |M_\mu|^2) \quad (1.47)$$

Finally, we insert equations 1.36 , 1.40, and 1.44 to obtain the relatively simple expression [11, 12]

$$\frac{d\Gamma}{d\omega d \cos \theta} = \frac{1}{512\pi^3} \left(\frac{\omega}{M_K} \right)^3 \beta^3 \left(1 - \frac{2\omega}{M_K} \right) \sin^2 \theta [|E_{IB} + g_{E1}|^2 + |g_{M1}|^2] \quad (1.48)$$

Ironically, however, the same lack of a $g_{E1}, M1$ interference term that gives 1.48 its compact form also reduces the E1 contribution to the final decay distribution. Since theoretical estimates of g_{E1} imply that it is a very small ($< 2.5\%$) correction [7] to E_{IB} , the IB,E1 interference term is expected to be the dominant E1 correction term. Hence, the explicit form of $|E_{IB} + g_{E1}|$ becomes crucial. The phases of the three matrix element contributions are given by

$$\delta_{IB} = \Phi_\pm + \delta_0^0(M_K^2) \quad (1.49)$$

$$\delta_{E1} = \Phi_\pm + \delta_{M1} \quad (1.50)$$

$$\delta_{M1} = \delta_1^1(M_{\pi\pi}^2) \quad (1.51)$$

where Φ_\pm is the phase of η_{+-} , and δ_0^0 and δ_1^1 are the standard pion scattering phase shifts⁸ computed from experimental measurements of $K_L \rightarrow \pi^0 \pi^\pm e^\mp \nu$ decays.

This leads to

$$\begin{aligned} |E_{IB} + g_{E1}|^2 &= |g_{E1}|^2 + |E_{IB}|^2 + 2|g_{E1}||E_{IB}| \cos [\delta_{M1} - \delta_0^0(M_K^2)] \\ &= |g_{E1}|^2 + |E_{IB}|^2 \left[1 + \frac{2|g_{E1}| \sin[\delta_0^0(M_K^2) - \delta_1^1(M_{\pi\pi}^2)]}{|E_{IB}|} \right] \end{aligned} \quad (1.52)$$

⁸see section 9.7.2 for more details

The M1 term will be expressed in terms of an amplitude \tilde{g}_{m1} and a vector form factor as follows

$$|g_{M1}| = \tilde{g}_{M1} \left[1 + \frac{\frac{a_1}{a_2}}{M_\rho^2 - M_K^2 + 2M_K\omega} \right] \quad (1.53)$$

Note that equation 1.52 clearly illustrates the difficulty in measuring $|g_{E1}|$ in the $K_L \rightarrow \pi^+\pi^-\gamma$ decay mode. Since $|g_{E1}|^2$ is predicted to be well below the experimental sensitivity, then the measurement of $|g_{E1}|$ will hinge critically on the ability of the likelihood fitter to resolve the $\frac{2|g_{E1}|\sin[\delta_0^0(M_K^2)-\delta_1^1(M_{\pi\pi}^2)]}{|E_{IB}|}$ term relative to 1.

Note that because $|g_{E1}|$ is a magnitude, the measured quantity in this analysis is constrained to be greater than or equal to zero.

Henceforth, to avoid writing explicit absolute value symbols, we will use the quantity “ G_{E1} ” where

$$G_{E1} \equiv |g_{E1}| \quad (1.54)$$

to denote the measured E1 amplitude.

Chapter 2

The KTeV Experiment

2.1 Creation of the Neutral Kaon Beam

The KTeV experiment was located on a new beamline on the east side of the existing Neutrino-Muon (NM) beamline at Fermi National Accelerator Laboratory (Fermilab). The 1997 E832 run, which is the run relevant to this analysis, took data from April to July 1997.

The name "KTeV" is an acronym for "kaons at the Tevatron" and actually encompasses two separate, but closely related, experiments: E799 and E832. The primary objective of E832 was to measure the direct CP-violation parameter $\text{Re}(\epsilon'/\epsilon)$, while E799 focused on measuring rare decays of the K_L particle, such as $K_L \rightarrow \pi^0 e^+ e^-$. The two experiments were conducted in the same experimental hall and used most of the same detectors.

The KTeV beam time was divided roughly equally between the two experiments. The primary differences between the E799 and the E832 configurations were that the E832 configuration included the regenerator and beryllium absorbers, and E799 had transition radiation detectors (TRDs)¹ installed downstream of the drift cham-

¹these detectors used "transition radiation" (i.e. the radiation released by a charged particle as it transitions across a boundary of two different indices of refraction) as a method of charged particle discrimination. As mentioned above, they are not used in the E832 version of the experiment.

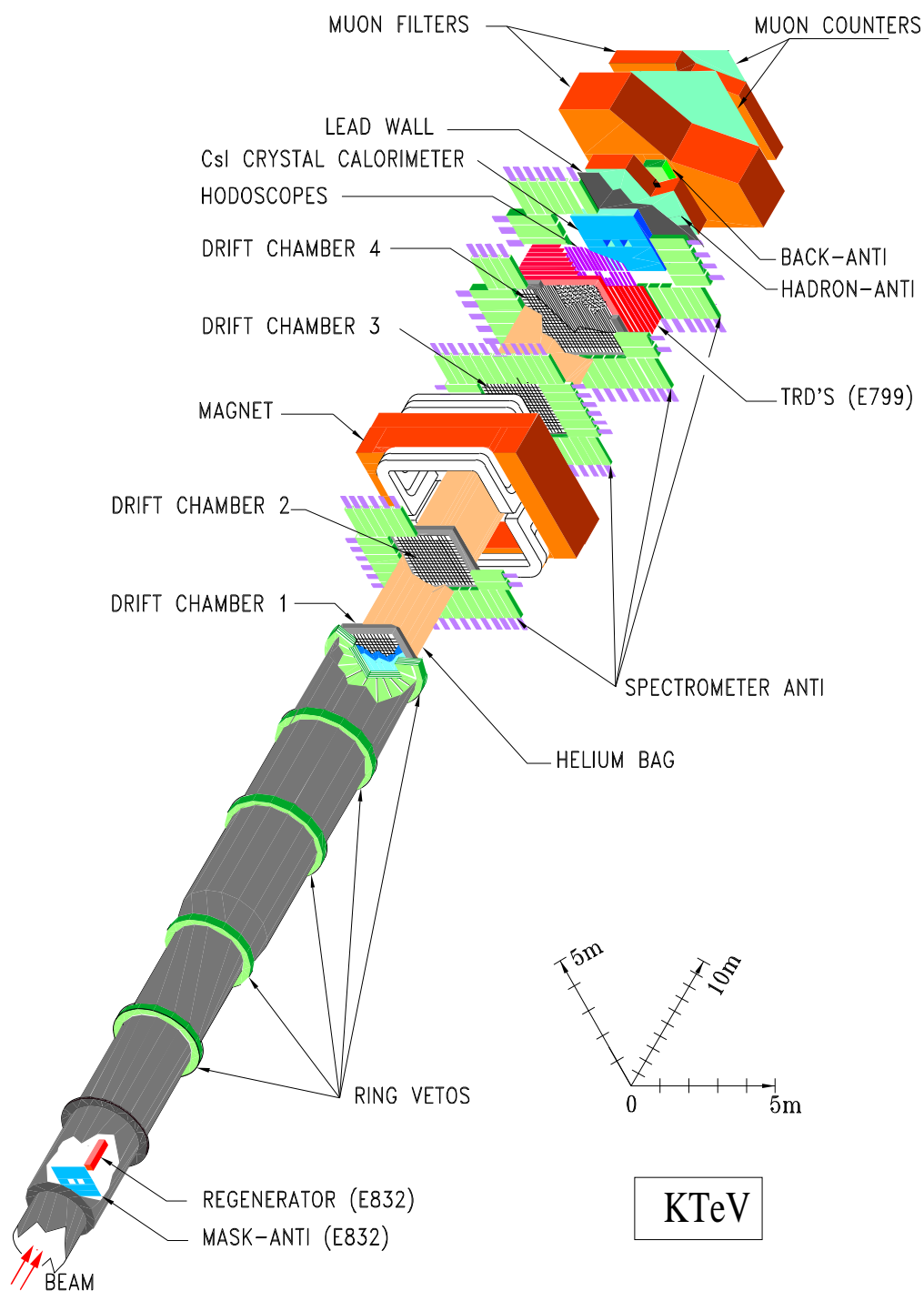


Figure 2.1: Three-dimensional cutaway of the KTeV Detector. Components labeled “E799” were not used in this analysis

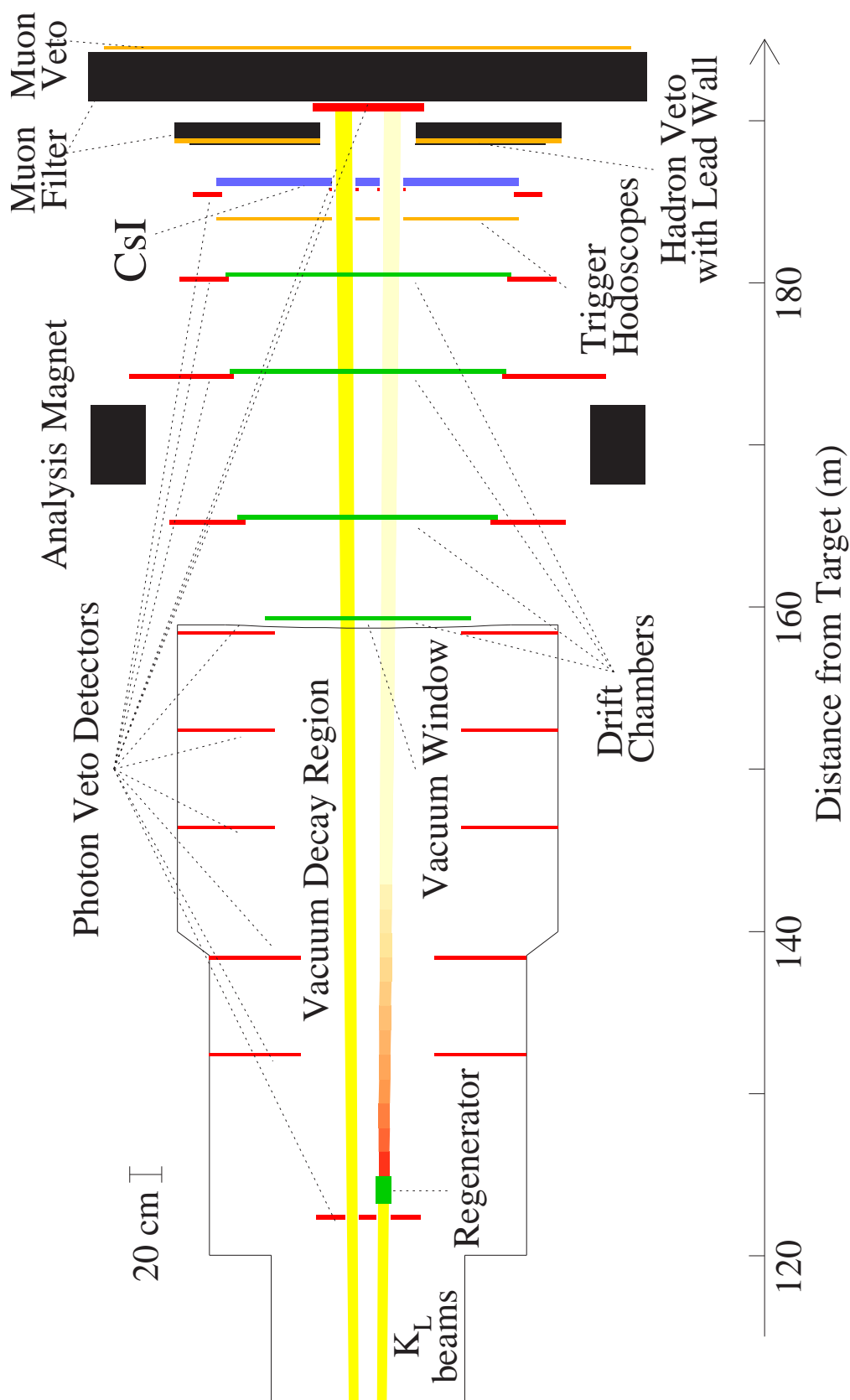


Figure 2.2: The E832 configuration of the KTeV Detector (plan view)

bers.

2.1.1 The Primary Proton Beam

The heart of the Fermilab proton beam is the Tevatron, a circular proton-antiproton ring roughly 6 km in circumference. The Tevatron delivered "spills" of 5×10^{12} 800 GeV protons to the NM beamline in 1 minute cycles. The first 40 seconds of the cycle were used to accelerate the proton bunch in the Tevatron and was referred to as "off spill". The beam was then extracted from the Tevatron, and sent to the NM beamline for the remaining ("on spill") 20 seconds.

Each spill had an additional microstructure imposed by a 53 MHz RF signal of the Tevatron such that on-spill protons arrived in 1-2 ns "buckets" once every 19 ns. A derivative of the RF timing signal was also sent to KTeV to synchronize the triggers with the incoming beam.

Once the proton beam was extracted from the Tevatron, the NM "primary beamline" magnets diverted the beam to the KTeV neutral beam production target. The final focusing quadrupole magnets and steering dipoles focused the proton beam size to $\sim 250 \mu\text{m}$ in both x and y and tilted the primary beam at a 4.9 mrad downward angle (with respect to the secondary beam, as defined by the collimator system). This beam angle was chosen to optimize the kaon-neutron ratio in the neutral beam and to maximize the final kaon flux.

The KTeV neutral beam production target was a 3 mm square beryllium oxide (BeO) rod, 30 cm long (1.1 interaction lengths). The center of the target defined the origin for the z coordinate of the experiment. The z axis was aligned with the collimated neutral kaon beam, the y axis was aligned with the vertical direction, and the right-handed coordinate system was completed by defining the positive x direction to be horizontal and to the left (as viewed by an observer gazing down-

stream).

2.1.2 The NM2 Beamline Enclosure

The NM2 Beamline Enclosure consists of a series of "sweeper" magnets, absorbers, and collimators that are used to produce the final neutral beam from the secondary beam produced by the interactions of the proton beam with the BeO target.

The first NM2 element encountered by the secondary beam was the "target sweeper", a magnet centered about 2 m downstream of the target that imparted a 3800 MeV/c transverse momentum kick to the primary proton beam and deflected it into a 4.5 m water-cooled copper block (the "primary proton dump"). Just downstream of the target sweeper was a second sweeper magnet, μ sweep 1, that deflected muons out of the beamline. Two more sweepers, μ sweeps 2 and 3, were used for similar purposes farther downstream.

The two common absorbers, the Beryllium absorber (Be absorber) and the lead absorber (Pb absorber), removed undesired neutral particles. The Be absorber was a 20 inch thick Be wall that attenuated neutrons, since neutrons have a higher interaction cross-section in Be than kaons, while the 3 inch Pb absorber removed photons.

Once the beam passed through the absorbers, it was defined by three collimators. The first and most important of the three was the "primary" collimator, located at $z = 20\text{m}$, which was comprised of a 2m long brass and steel block with square tapered holes. The holes produced two separate neutral beams with their centers separated by 1.6 mrad relative to the target. The second ("slab") collimator was a 2m tapered stainless steel block positioned between the parallel beams about 18 m farther downstream. Its primary function was to prevent scattered particles from crossing from one beam to another.

The third collimation element, at $z = 85\text{m}$, was the “defining” collimator. This was a tungsten block with tapered square holes that set the final beam shape. The combination of all these elements produced a neutral beam with a final beam divergence of 0.5 mrad and a 3:1 neutron/ K_L ratio [14].

The final NM2 element that should be mentioned is the regenerator, which regenerated K_S from K_L . It was 40 m downstream of the defining collimator (at $z = 125\text{m}$) and alternated between the two neutral beams on each spill. However, since this analysis used vacuum beam only, the regenerator was irrelevant to the events in the particular data sample analyzed in this thesis².

2.1.3 The Vacuum Decay Region

The kaon decay region was a 65m airtight steel enclosure operated at an internal pressure of 1.0×10^{-6} torr. It was 45 cm in diameter at the upstream ($z = 94\text{ m}$) end and 2.4m in diameter at the downstream ($z = 158.9\text{m}$) end. To withstand the 222kN of integrated force exerted by atmospheric pressure outside the decay volume, the vacuum window on the downstream end was made from a 7.6mm (0.00016 radiation length) Kevlar weave. A layer of aluminized Mylar was laminated on the Kevlar to minimize air permeability.

2.2 The KTeV Detector

2.2.1 The Calorimeter

The calorimeter [15] was one of the centerpieces of the KTeV experiment and was essential to the $K_L \rightarrow \pi^+\pi^-\gamma$ analysis, as it is the only component capable of

²except in the rare cases when regenerator events were scattered into the adjacent vacuum beam. This effect will be discussed in section 9.4 along with the other backgrounds.

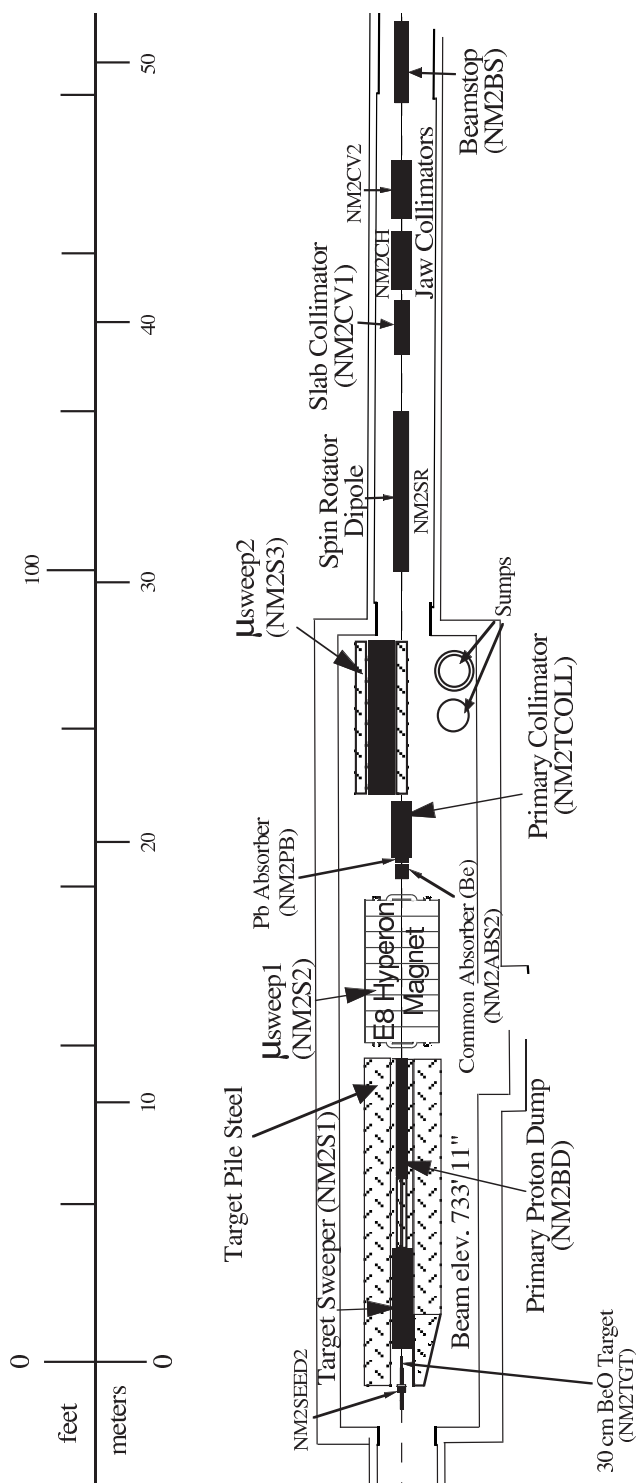


Figure 2.3: The NM2 beam enclosure

measuring photon energies and position. It consisted of 3100 blocks of pure Cesium Iodide, arranged in a 1.9m x 1.9m square array. As a cost-savings measure, in both crystal manufacture and in the accompanying electronic channels, two different CsI block sizes were used.

The inner region of the detector, where resolution of position and cluster separation are most critical, was composed of 2232 small (2.5cm x 2.5 cm) blocks, while the outer region used 868 larger (5 cm x 5 cm) blocks. There were also two 15 cm square holes in the center of the detector (see figure 2.4) that allowed the primary kaon beams to pass through without damaging the crystals.

Each block, large or small, was 50 cm long (27 radiation lengths), so essentially all photon energy was contained by the crystals. To compensate [16] for variations in longitudinal scintillation response from block to block, each crystal was individually wrapped in 13 μm black or aluminized mylar, resulting in a block scintillator response uniformity of about 5 percent. Since 50 cm of CsI corresponds to 1.4 nuclear interaction lengths, pions and muons typically deposited only a small fraction of their energies in the calorimeter.

The light yield in a crystal was about 20 photoelectrons per MeV of deposited energy. There were two components to the scintillation light: a "fast" contribution that peaked at 305 nm and fell off with a decay time of about 25 ns, and a "slow" contribution that peaked at 480 nm and decayed in about 1 μs . The CsI crystals proved to be an excellent choice for the calorimeter, allowing it to attain a resolution of

$$\frac{\sigma_E}{E} = 0.0045 + \frac{0.02}{\sqrt{E}} \quad (2.1)$$

where E is measured in GeV.

Nevertheless, the crystals were not without disadvantage. Pure CsI, while possessed of exceptional scintillation and radiation hardness properties, is also fairly soft and somewhat hygroscopic. Therefore, the calorimeter was contained in a sealed metal enclosure called the "blockhouse" that had its own air conditioning and dehumidifier units to protect the crystals and cool the electronics.

The Calorimeter Readout

Each crystal was optically coupled to a photo-multiplier tube (PMT) via a glass "cookie" and a disk of Schott UG-11 filter glass, which filtered out most of the slow component of light. The large crystals were coupled to a 6-stage Hamamatsu 1.5 R5330 PMT, while the smaller crystals used 5-stage 0.75 R5364 Hamamatsu tubes. The tubes ran at 900-1500V with a typical gain of about 5000.

The PMT dynode signal was shunted to the E_{total} system in the L1 trigger, while the anode signal was digitized and buffered locally by the digital photo-multiplier tube (DPMT) board. The DPMT was comprised of an 8-bit flash analog-to-digital converter (ADC) and two custom chips: the charge integrator and encoder (QIE) and the driver-buffer-clock (DBC). The QIE divided the PMT signal current among 8 capacitors, each receiving a different fraction of the current ($I/2$, $I/4$, $I/8$, ..., $I/256$). The charge across each capacitor was integrated and compared to a reference voltage. This voltage was then digitized by the flash ADC and stored as a mantissa, along with a 3-bit exponent for the voltage range. The QIE contained 4 such circuits that were filled in round-robin fashion for each RF bucket.

The mantissa, exponent, and QIE circuit number ("cap ID") were all written to a FIFO (first-in-first-out) buffer in the DBC. The buffer had a depth of 32 words and was only read out if the L1 trigger was satisfied.

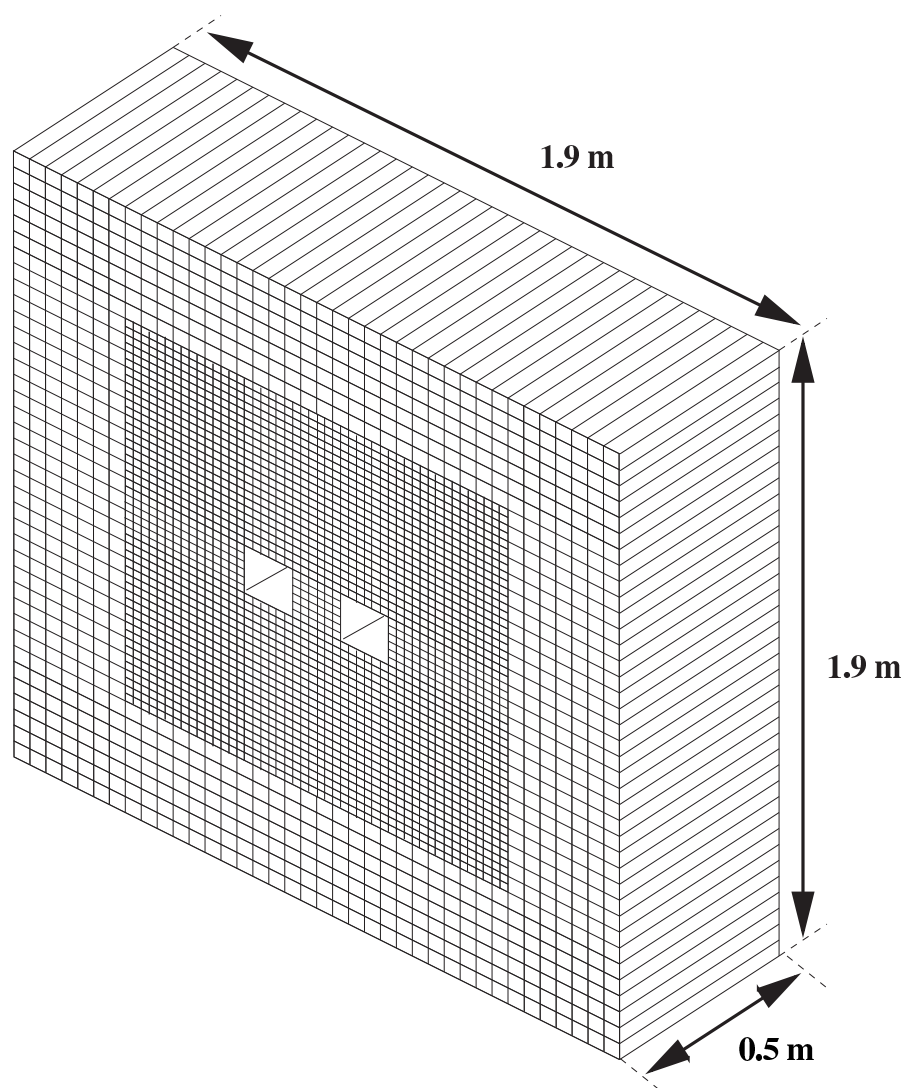


Figure 2.4: Schematic of the KTeV CsI Calorimeter

Calorimeter Calibration

A dye laser, capable of producing shaped pulses of UV light, was connected to each individual crystal via optical fibers. During special runs [17] known as "laser scans", the entire DPMT dynamic range was scanned by slowly turning a variable filter wheel in front of the laser. The flashes were also sent to several highly linear and stable PIN photodiodes, which provided an independent measure of the stability of laser light amplitude.

The channel gains were calibrated using electrons from K_{e3} events³. Since the ratio of energy to momentum (E/p) is approximately 1.0 for electrons, the charge to energy ratio (Q/E) for each channel could be determined via an iterative process using electron momentum information from the spectrometer.

2.2.2 The Magnetic Spectrometer

The spectrometer consisted of an analysis magnet and 4 drift chambers (DC 1-4), with 2 chambers upstream of the magnet and 2 chambers downstream. A helium bag was placed between each element to reduce the probability of multiple scattering, photon conversions, and beam interactions in air. The relative positions and dimensions of the components is summarized in table 2.1.

This configuration resulted in a resolution [13] of

$$\frac{\sigma_p}{p} = (0.38 + 0.016P)\% \quad (2.2)$$

where P was measured in GeV/c.

³ K_{e3} is a commonly used "short-hand" term for the $K_L \rightarrow \pi^\pm e^\pm \nu$ decay

Spectrometer Element	z (m)	Dimensions, x × y (m)
DC1	159.4	1.3 × 1.3
DC2	165.6	1.5 × 1.5
Analysis Magnet	170.0	2.9 × 2.0
DC3	174.6	1.6 × 1.6
DC4	180.5	1.8 × 1.8

Table 2.1: z positions and dimensions of KTEV spectrometer

The Analysis Magnet

The analysis magnet was a large dipole magnet that drew 1600 A of current and generated a field strength of 2 kG in the vertical (y) direction. This produced a 412 MeV/c transverse momentum "kick" along the horizontal (x) axis. The magnet polarity was flipped once every one to two days to minimize any geometrical biases in the detector.

The Drift Chambers

The drift chambers [18] were constructed using 100 μm diameter gold-plated aluminum for the cathode (field) wires and 25 μm diameter gold-plated tungsten for the anode (sense) wires. The x and y views of each of the 4 chambers consisted of parallel sense wires with a 12.7 mm wire separation. The first plane of sense wires in a given view was followed by a second plane with a wire spacing offset by half a wire-separation distance in order to resolve left-right ambiguity. This "plane pair" arrangement produced hexagonal cells 12.7 mm in diameter (see figures 2.5 and 2.6). Each chamber contains two plane-pairs parallel to x (the "x-view") and two plane-pairs parallel to y (the "y-view").

The chambers were filled with 50/50 Argon/Ethane gas, with a small amount ($\sim 1\%$) of isopropyl alcohol added to absorb the UV light that caused deposition

on the wires. Incoming charged particles ionized the gas, releasing electrons and producing a current in the sense wire. The signals from the chambers were then recorded by time-to-digital converters (TDCs), and the drift time information was used to calculate the position of the original ionizing particle. The field wires were kept at a potential difference of 2450-2600 V relative to the sense wires, which corresponded to an electron drift speed of $50 \mu\text{m}/\text{ns}$ and a drift time less than 200 ns.

Drift Chamber Calibration

In order to produce precise mappings from TDC time information to track position (XT maps), special "muon runs" were performed every couple of days. During these runs, the beam stop was inserted into the beam line, the analysis magnet was turned off, and the sweeper magnet settings in NM2 were adjusted to allow charged particles. Since muons were essentially the only charged particles that penetrated the beam stop, this configuration produced a relatively clean beam of straight-trajectory muons. Chamber alignment was then achieved by comparing the track-hits in each chamber. In addition, an offline calibration using K_{e3} vertexing information was done to measure rotational variations of DC 2, 3, and 4 relative to DC 1.

2.2.3 The Trigger Hodoscopes

The trigger hodoscopes were two back-to-back 1.9 m square scintillator arrays placed at $z = 184$ m that provided the Level 1 trigger with charged particle tracking information on timescales much faster than the 200 ns drift times needed for the

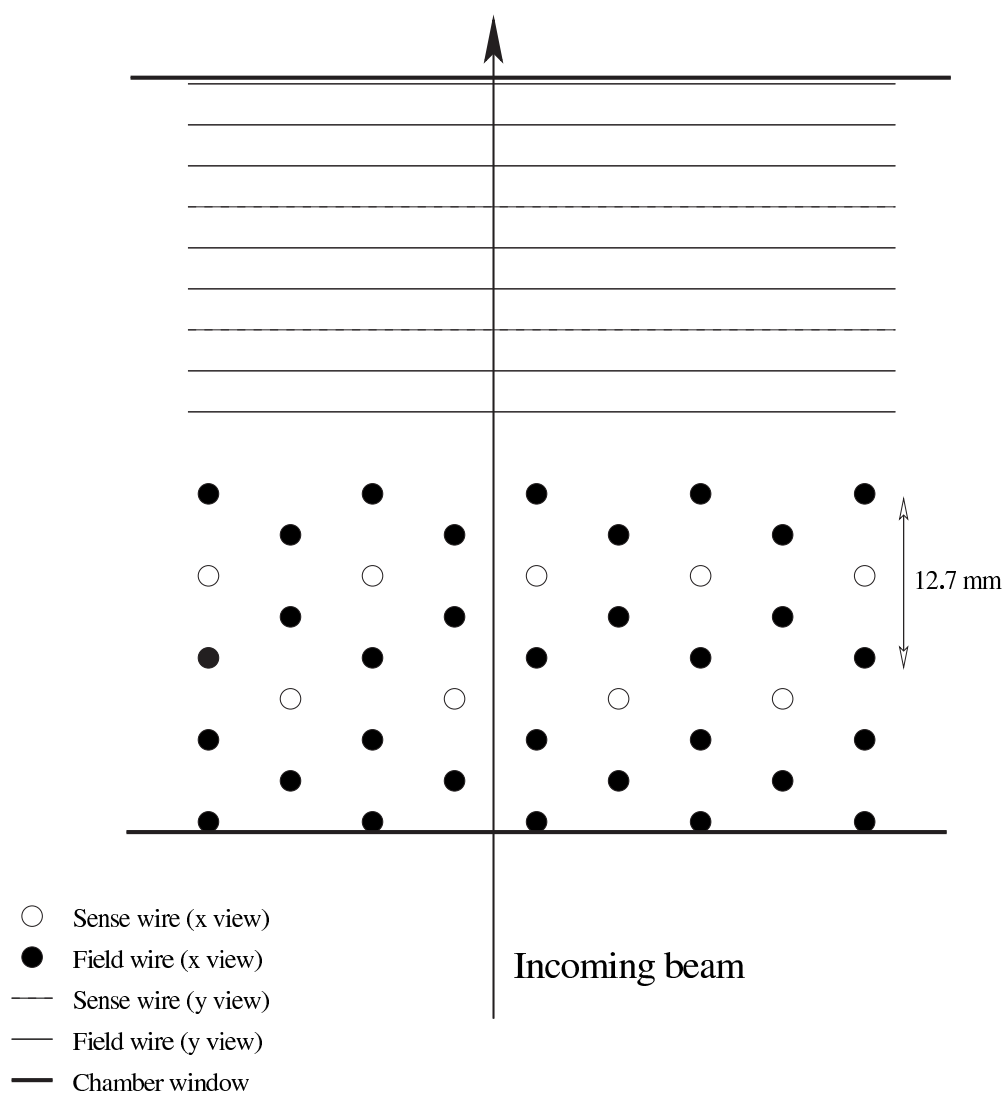


Figure 2.5: Top (y) view schematic of the field and sense wire arrangement within a drift chamber.

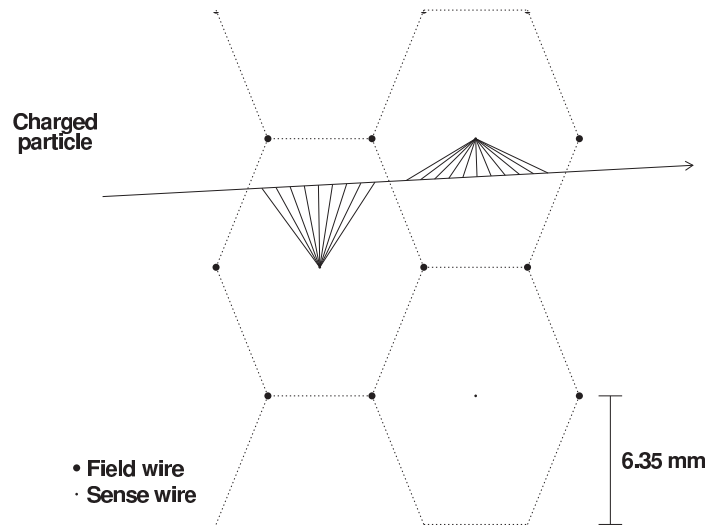


Figure 2.6: Close-up view of a charged particle passing through a pair of hexagonal drift chamber cells. The thin lines represent the drift paths of ionization electrons toward the sense wires.

drift chambers. The upstream (V) counter consisted of sixteen 88 cm scintillator paddles above the beam and sixteen 110 cm paddles below the beam. The downstream (V') counter had fifteen 110 cm paddles above the beam and fifteen 88 cm long paddles below the beam. Each scintillator was connected to a photo-multiplier tube that sent a signal to the L1 trigger.

In order to reduce the effects of the cracks between scintillators, the V and V' counters were offset from one another through the use of 5 different widths (9.92, 11.82, 13.74, 15.63, and 17.76 cm) of paddles. In addition, 14 cm square beam holes were cut into each plane to reduce trigger rates and minimize shower material in the beamline.

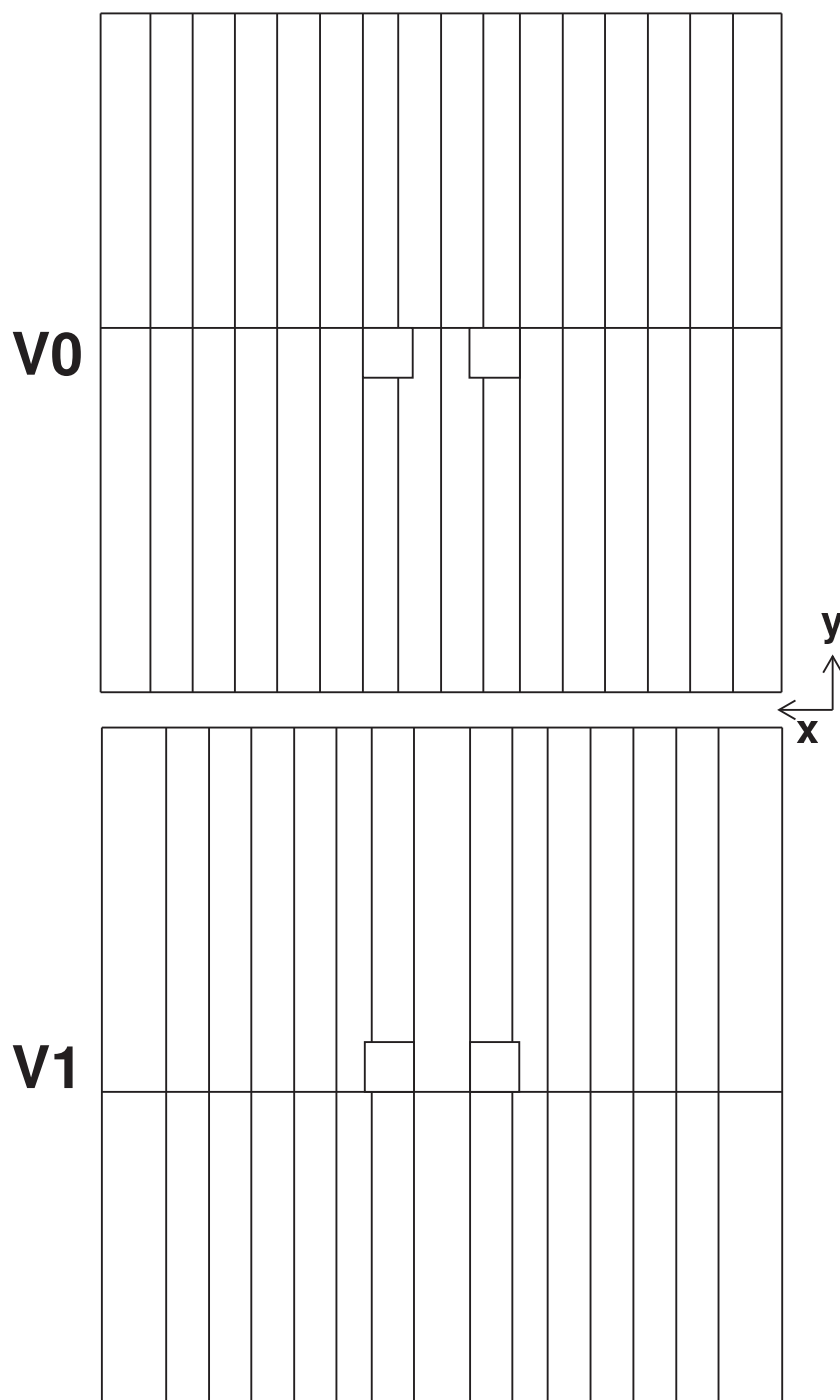


Figure 2.7: Schematic of the V and V' Trigger Hodoscope Plane Configurations

2.2.4 The Hadron Anti

A 15 cm (0.9 nuclear interaction length) lead brick wall was constructed just downstream of the calorimeter. It served a dual purpose: it absorbed EM shower leakage from the back of the calorimeter, and it induced hadronic showers that could be measured by the Hadron Anti (HA).

The HA was a 2.24 m x 2.24m array of scintillator counters. It consisted of 28 scintillator paddles, 14 above the beamline and 14 below, with a 64 cm x 34 cm beamhole. The HA counter readout was used in the triggers.

2.2.5 The Muon Vetoes

The muon vetoes [19] consisted of a 1m thick steel muon filter (MF1), and two muon filter-counter arrays. MF1 was placed directly behind the Hadron Anti, and Muon Filter 2 (MF2) was about two meters farther downstream. MF2, which doubled as the neutral beam stop was the largest of the three muon filters, measuring 4.3m across, 3.4 m high, and a full 3 m thick- 44 cubic meters of solid steel in all. Directly downstream of MF2 was the 3m x 4m MU2 scintillator array.

Less than half a meter behind MU2 was the second filter-counter array, consisting of another 1m thick steel wall (Muon Filter 3- MF3) and another muon counter array (Muon Counter 3- MU3). MU3 consisted of two 3m x 3m scintillator planes, MU3X and MU3Y. MU3X had 40 scintillator paddles oriented vertically, while MU3Y had 40 paddles oriented horizontally. Together the two planes produced a muon hit resolution of less than 15 cm. MU3 was not used in this analysis.

2.2.6 The Photon Vetoes

A number of detectors were used to veto on high-angle photons that exited the fiducial volume of the experiment before reaching the spectrometer or calorimeter.

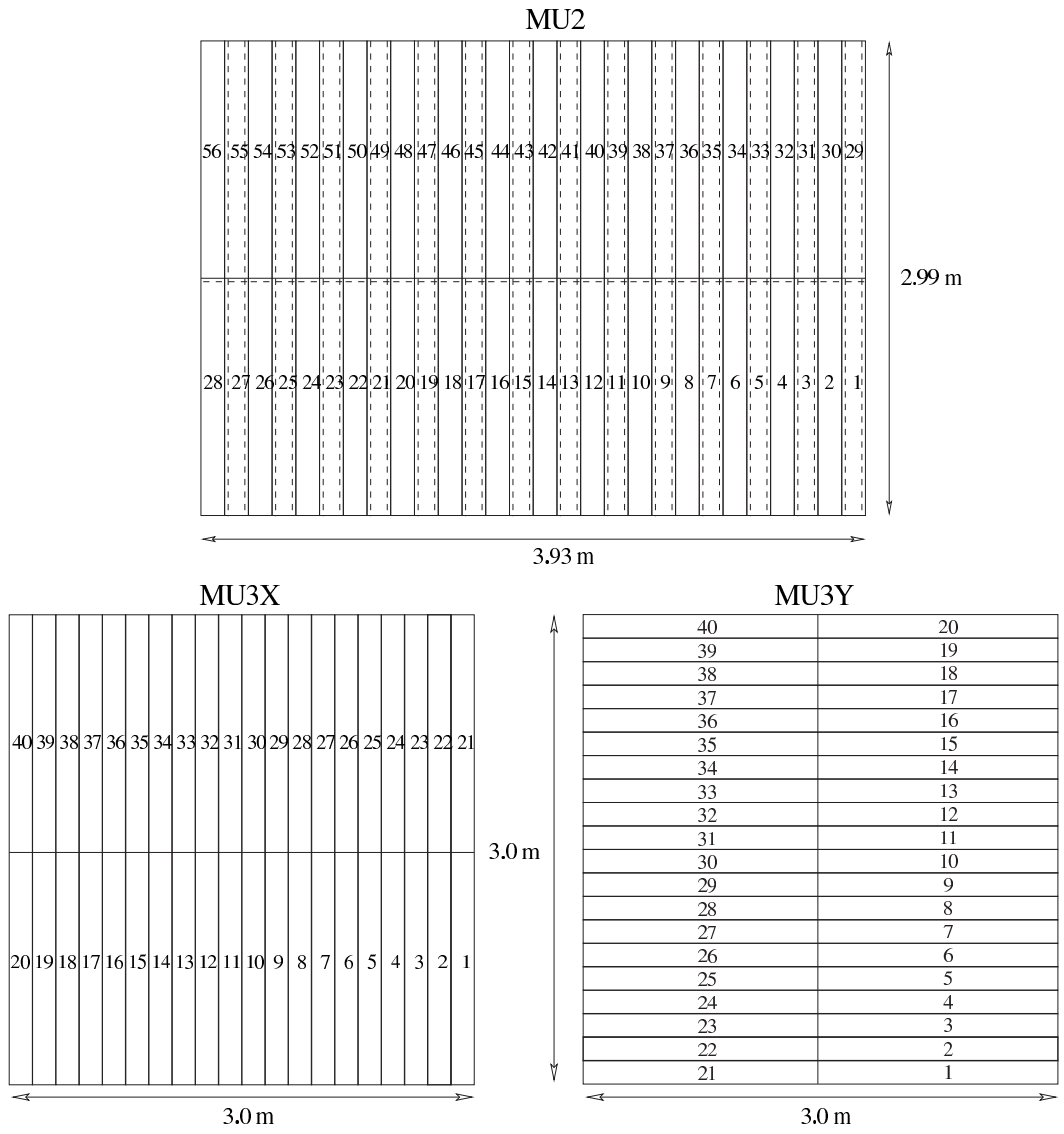


Figure 2.8: Schematic of Muon Trigger Planes. Dashed lines indicate the 1 cm counter overlaps in MU2

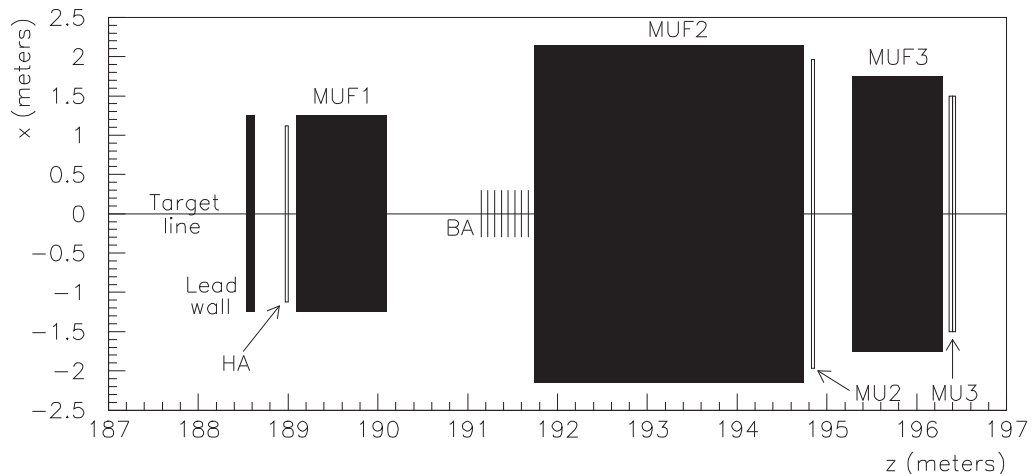


Figure 2.9: y view of the KTeV detector downstream of the CsI calorimeter

The first of these were the five ring counters (RC6-10), which were each composed of 16 overlapping scintillator paddles arranged in an azimuthal ring around the inner edge of the vacuum decay region at different z positions. Although the outer edge of each RC was circular, the paddles were cut so that the inner edge was square, defining the fiducial region of the experiment. Each individual paddle had 24 lead-scintillator layers (corresponding to 16 radiation lengths) and was connected to a PMT whose pulse height was digitized by a LeCroy 4300 ADC.

Farther downstream were the spectrometer anti counters (SA2-4) and the CsI Anti (CIA). SA2-4 framed the outer edges of drift chambers 2-4, while the CIA framed the outer edge of the calorimeter. These rectangular scintillator arrays were 16 radiation lengths thick and were useful for detecting photons as well as charged particles that were "kicked" out of the detector region by the analysis magnet. If at least 0.5 GeV of in-time energy was deposited into any RC, SA, or CIA paddle, a signal was sent to the L1 trigger to veto the event.

The calorimeter also had a second type of veto, the Collar Anti (CA), that was

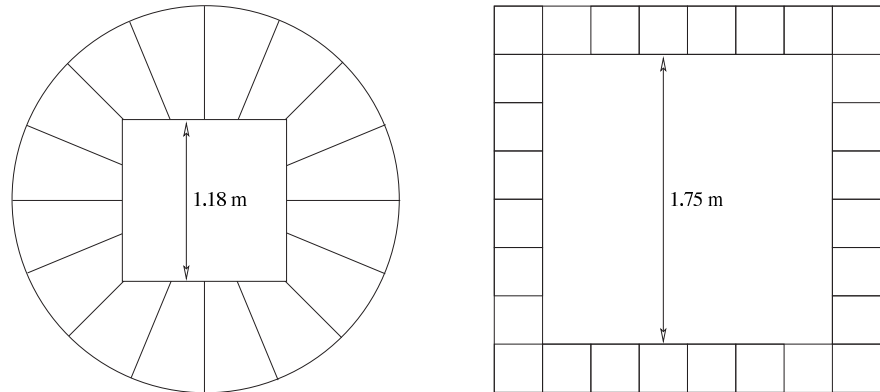


Figure 2.10: Schematics of typical photon veto detectors. RC10 is shown on the left, SA4 on the right

used to veto particles that struck the calorimeter too close to the beam hole and would thus only have a fraction of their energy recorded by the CsI crystals. Each beam hole was overlapped by a square CA ring that consisted of 4 scintillators. Each counter was 1.5 cm wide and was constructed from tungsten-scintillator layers 9.7 radiation lengths in depth. If at least 14 GeV of in-time energy was deposited in any segment, a veto signal was sent to the L1 trigger.

The final veto was the Back Anti (BA), a 30 cm x 60 cm counter designed to veto particles travelling into either of the two beam holes in the CsI detector. The BA consisted of 30 layers of lead-scintillator sandwich (30 radiation lengths or 1 nuclear interaction length) that were placed directly in the beamline, just in front of MUF2. It was divided into three longitudinal modules to distinguish between electromagnetic and hadronic particles, based on shower shape. The BA was not used in this analysis.

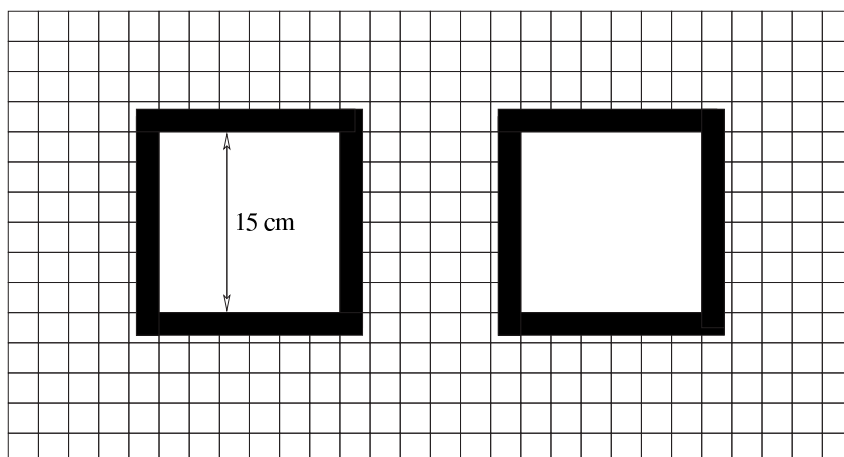


Figure 2.11: Schematic of the CA around the calorimeter beam hole

Chapter 3

The KTeV Trigger System

The Tevatron sent 3000 protons to the KTeV target in a 19 ns bucket, which translated to roughly 3×10^{12} protons in each 18-20 second spill. Therefore, even though a proton only had a 1 in 10^5 chance of producing a kaon, it still meant that 30 million kaons were produced each spill. Since roughly only 5% of these 30 million kaons would decay within the fiducial volume of the detector [19] and only a small fraction of those decays were interesting, it became imperative to design an efficient trigger capable of preferentially selecting specific categories of decays.

The KTeV trigger system [20] had three decision levels, each with different dead-time limits and correspondingly different selection strategies. The level 1 trigger was a deadtime-less trigger using commercial electronics, fast signals, and simple lookup tables. The level 2 trigger was a set of custom processors that evaluate numbers and patterns of drift wires and CsI channels, and the level 3 trigger used software running on 24 parallel CPUs that reconstructed events and made loose kinematic cuts.

In general, the triggers were designed to be as loose as possible, in an attempt to gain essentially 100% efficiency for the primary $\pi\pi$ signal mode. More details about specific trigger elements will be discussed in Chapter 4.

3.1 The Level 1 and Level 2 Triggers

The Level 1 and Level 2 triggers [22, 23] used fast Boolean digital signals ("sources") to produce trigger decisions. The detector sources (usually from photomultiplier tubes) were divided into 12 groups of 8 sources each and were timed to the beam. Each group of sources was fed into a LeCroy 4413 memory lookup unit (MLU), which, in turn, sent out a 16 bit word to an array of LeCroy 4508 programmable logic units (PLUs). Cable delays were employed to ensure that the array received the MLU inputs simultaneously, and the final trigger signal was the AND of all 12 groups. The PLUs, which contained CAMAC-programmed memory lookup tables, compared the combined trigger signal to the lookup tables to determine whether the trigger criteria had been satisfied.

3.1.1 The Level 1 Trigger Decision

An "accept" decision at Level 1 began the digitization of the detector via ADC, TDC, and latch modules and stored the calorimeter information in FIFO ("first in-first out") Buffers.

Trigger stations could be as much as 62 m from the original feed-through, so "hard-line" RF waveguides were used to reduce trigger processing times. These hard-lines had a signal propagation speed of $0.88c$, which was significantly faster than the $0.64c$ propagation rate of standard coaxial cable. To reduce the trigger rate further, the level 1 process was inhibited by hit signals from the fast photon vetoes. The downside of the fast vetoing, however, was that accidental activity in various detectors could cause otherwise good events to fail the triggering criteria.

These innovations, along with the fast signals and relatively simple pattern-matching logics, allowed the Level 1 trigger to be efficient enough to complete

processing within the 19 ns bucket window without downtime¹. The raw L1 trigger rate was about 60 kHz under normal operating conditions.

3.1.2 The Level 2 Trigger Decision

The Level 2 trigger [24] was composed of primarily custom electronics designed to do pattern matching at a more sophisticated level than the L1 trigger. One of the primary level 2 elements was the Drift Chamber Hit Counter (DCHC) system, which was designed to take fast signals from each drift chamber wire and count the number of hits that occurred on different plane-pairs to determine if they were "in time" (i.e. if they came from the same track).

The DCHC system [25] was itself composed of two subsystems: the "bananas" (an name derived from the curved plots it produced), which were used for chambers 1 and 2, and (in keeping the fruit theme going) the "kumquats", which were used for chambers 3 and 4. The kumquat boards simply required that latch hits occur within an 220 ns time interval, while the banana boards technically had more functionality in that they could correlate time information between hits and essentially cut on the "sums of distances" (SODs) position measurement. In practice, however, concerns over possible trigger inefficiencies caused the bananas to be used in "wide open" mode for the $\eta\pm$ trigger, which made them functionally equivalent to the kumquats. In this configuration, the DCHC system had a decision time of 800 ns.

Another key Level 2 element was the y track finder (YTF) [26], a commercial programmable logic unit that was used to determine whether hits in the drift chamber system were consistent with two straight tracks in the y view. It was optimized for the $K_L \rightarrow \pi^+\pi^-$ decay, so it searched for one track in the upper region of the chambers, and one track in the lower region. To increase acceptance, the central

¹ignoring detector-level downtime such as the drift chamber reset time

part of the chamber was counted as both "upper" and "lower". The inputs to the YTF were coarse signals from the DCHC system, and its output, which was usually produced a few hundred nanoseconds before the DCHC decision, was a 4-bit word containing the number and location of found tracks.

The final Level 2 element of note, although not used in the $K_L \rightarrow \pi^+\pi^-\gamma$ trigger decision, was the hardware cluster counter (HCC), which was designed to count calorimeter "clusters" (i.e. sets of contiguous channels that all had energy deposited above some common threshold, nominally 1 GeV). The HCC [27, 28] counted the clusters based on the patterns of energy deposited in 2x2 groups of crystals.

The HCC proved extremely useful at reducing the rate of the neutral mode trigger, which, at Level 1, only required a certain amount of total energy in the calorimeter, and therefore accepted copious numbers of K_{e3} and $3\pi^0$ decays. It also had the longest decision time of any L2 element (1.5 μ s).

If an event passed the Level 2 decision, digitization of the calorimeter continued to completion, and the front-end detector modules were read out. If the event failed the Level 2 criteria, the front-end modules were cleared and the trigger system was re-enabled within a few microseconds. The combination of the front-end readout and the module clearing together produce a deadtime of roughly 35% under normal running conditions. The standard Level 2 trigger rate was 10 kHz [29].

3.2 The Level 3 Trigger

If the Level 2 trigger was satisfied, the entire detector was read into computer memory. The level 1 and level 2 selection criteria reduced the event rate enough that there was sufficient memory to store data from the entire 20 second spill.

This meant that the 24 Level 3 CPUs had the entire minute (20 seconds "on spill" and an additional 40 seconds "off spill") to process the spill data without incurring deadtime. The Level 3 software [30, 31] applied a minimal set of kinematic and particle identification cuts to categorize events by their final decay products. The software began by reconstructing track and vertex candidates. The calorimeter information, which was much more CPU intensive than the tracking and vertexing, would then only be unpacked if one or more suitable vertex candidates were found. This was important aspect of the trigger, since there was not enough time within the one minute window to automatically run clustering on all events.

Because the Level 3 cuts depended on the preliminary "on-line" detector calibrations, they were designed to be extremely lenient, and particles were allowed to receive multiple Level 3 tags. This way, all potential vertex candidates were saved and could later be analyzed more carefully off-line. For many high-rate decay types (such as $K_L \rightarrow \pi^+\pi^-\pi^0$ and K_{e3}) only a fraction of events were desired and the Level 3 trigger only tagged a prescaled subset of them. In addition, a fraction of all input events were tagged to be saved as "random accept", regardless of Level 3 processes, so that possible Level 3 software biases could later be studied.

Any event tagged as part of one or more decay types was written to digital linear tape (DLT). At nominal beam intensity, the level 3 trigger had a processing rate of roughly 0.7 kHz.

Chapter 4

Event Reconstruction

4.1 Track Reconstruction

The track reconstruction process began with the unpacking of the time-to-digital converter (TDC) information from the drift chambers. The tracking algorithm then used the XT maps (described in section 2.2.2) to convert the drift times into distances. Drift chamber "hits" were classified as "in-time" if they fell within a window of 235 ns in width.

4.1.1 hit pairing

If a charged particle that struck a given drift chamber plane also left a hit in the complementary plane (i.e. the parallel plane offset by half the sense wire spacing) in the same chamber, the 2 hits were grouped together as a "hit pair" for that chamber. The drift distances for the 2 individual hits of a hit pair were combined to form "sums of distances" (SODs) for each track. In theory, the SOD value should correspond to the spacing of the sense wires (6.35 mm). A SOD that was within ± 1 mm of this value (± 1.5 mm for the X-views of DC 3 and 4) was considered a "good" SOD. The position resolution was typically $100 \mu\text{m}$, so the combined SOD resolution was $\sqrt{2}$ times this, or $140 \mu\text{m}$. The track position was computed as the

average of the two position measurements.

SOD values that deviated from the sense wire width by more than 1mm were known as "high" and "low" SODs. High SODs generally occurred when a charged track passed too close to a particular sense wire. When this occurred, the electrons did not have enough time to avalanche before striking the wire and therefore did not rise above the threshold immediately, resulting in a delayed time measurement. Because of this, the other position measurement of such a hit pair was usually more accurate.

Low SODs were generally the result of two tracks hitting the same drift chamber cell. Therefore, each cell would register 2 in-time hits.

It was also possible to have "isolated hits"– i.e. a hit that registered in only one of the two planes of a drift chamber. In such a case, it is not possible to determine which side of the wire the track was on, and hence both permutations were considered.

To aid in the track selection, a "track quality" value was assigned to each hit pair. Single hits were given a quality value of 1, low and high SODs were given a value of 2, and good SODs were assigned a quality value of 4.

4.1.2 Y Track Finding

The tracking algorithm began by looking for y-view track candidates. This was because the tracks were not bent by the magnet in the y direction, and hence the track identification in the y-view was simpler than in the x-view. Hit pairs in chamber 1 were matched with hit pairs in chamber 4 and a straight line was drawn between them. The tracking program then searched for hit pairs in the two intervening chambers (DC2 and DC3) that were within 5mm of the line.

If matching hits were found in all four chambers, the quality values for all candi-

date hit pairs (and/or isolated singles) were summed. A "perfect" track candidate would have a quality rating of 16 (4 quality points \times 4 chambers), a candidate with 3 good SODs and one isolated hit would be rated at 13, and so on. The tracking criteria required a minimum quality rating of 12, which meant that no track candidate with more than one isolated hit would be accepted.

A track χ^2 was then calculated for all candidates that survived the quality cut, and only candidates with a track $\chi^2 < 4$ were accepted.

4.1.3 X Track Finding

Once the y tracks were calculated, the algorithm performed a similar search for x-view track candidates, with the added complication that the analysis magnet bent the x-view tracks between drift chambers 2 and 3. Hit pairs were produced in a manner analogous to the y tracks, but instead of producing a track trajectory between drift chambers 1 and 4, the x-view tracking algorithm produced two "track segments", with one segment connecting DC1 and DC2 and the other segment connecting DC3 and DC4. All possible candidates for track segments were looped over, and then the complete-track candidates were produced by connecting candidate track segments at the mid-plane of the magnet.

Upstream segments (from DC1 and DC2) were allowed 2 bad SOD hit pairs (quality value > 3), while the downstream segments (from DC3 and DC4) were only allowed one bad SOD (quality value > 4).

4.1.4 Vertex Determination

Once the best track candidates were determined, their trajectories were extrapolated upstream to find the z positions of track pair intersections. All possible combinations of y-view track pairs were calculated first, followed by all combina-

tions of x-view pairs. A vertex candidate was then defined as a matched set of an x-track intersection and a y-track intersection that was consistent with the tracks originating from the same z position (i.e. consistent with being the decay products of the same parent kaon). Not surprisingly, this often produced a relatively large number of vertex candidates.

The first method of reducing this number was to require that the individual x-view tracks of a given vertex candidate bend in opposite directions, hence requiring that the vertex be produced by a pair of oppositely charged particles. Any x-y track combinations that remain are then extrapolated downstream to the face of the calorimeter.

This so-called "track-cluster matching" required that a vertex candidate must have a calorimeter cluster within 7 cm of the extrapolated track position in order to be accepted. Note that this matching was critical to the tracking regime, since the orthogonal nature of the x and y views make it impossible to match x and y tracks using the drift chambers alone.

Finally, after some fine-tuning corrections [18] to the track positions, χ^2 fits were applied to the surviving vertex candidates. The best vertex was then selected from this Vertex χ^2 calculation, the segment-matching χ^2 at the magnet, and the number of good SOD pairs (i.e. the track "quality value") in the candidate tracks.

4.1.5 Track Momentum Determination

Once a vertex had been calculated for a given event, the momentum of the constituent tracks was determined by the bending of their trajectories in the analysis magnet between drift chambers 2 and 3.

The momentum (p) of a given charged particle of charge q is related to its bending angle $\Delta\theta$ by

$$p = \frac{p_{kick}}{\Delta\theta} \quad (4.1)$$

where the momentum kick (p_{kick}) is given by

$$p_{kick} = \int \vec{B} \cdot d\vec{l} \quad (4.2)$$

where \vec{l} is the particle trajectory vector and \vec{B} is the magnetic field at each point.

4.1.6 Neutral Particle Reconstruction

Neutral particles like the photon or π^0 were not detected by the drift chambers and therefore needed to be reconstructed from the calorimeter "clustering" routines alone. Figure 4.1 shows the calorimeter display of clusters for typical $K_L \rightarrow \pi^+\pi^-\gamma$ event.

Hardware and Software Clusters

The clustering algorithm [17, 36] began by using the hardware cluster counter (HCC) bit information from the ETOT trigger to find local maximum in the amount of energy deposited in the crystal array. A local maxima with greater than 0.1 GeV was designated the center, or "seed", of a hardware cluster. The complete cluster was defined as a square block of crystals centered on this seed-either 7x7 small crystals or 3x3 large crystals. The "raw" energy of the cluster was defined as the sum of all the energies in the grid of crystals.

However, since low-energy photons and minimum-ionizing particles (MIPs) such as pions or muons left too little energy in the calorimeter to trigger HCC bits, there was a second class of clusters, known as "software clusters", that were determined without the HCC information. The software cluster algorithm defined any non-hardware-cluster crystal that had an energy above a certain threshold, nominally

50 MeV, as a software cluster seed. The raw energy of each cluster was then computed in a manner similar to the hardware clusters. Software clusters with net raw energies of less than 100 MeV were dropped.

Cluster Position

The x position of a cluster was determined by summing the crystal energy in the central column (i.e. the one containing the seed block) and comparing to the energy sums of the adjacent columns. The ratios of the column energies were then compared to pre-determined lookup tables (produced from studies of $K_L \rightarrow \pi^0\pi^0$ and K_{e3}) that outputted the cluster x position. The y position was produced in a totally analogous way, except using the cluster rows instead of columns. This method resulted in a position resolution of ~ 1 mm for clusters in small blocks and ~ 1.8 mm for clusters in large blocks [16].

KTEV Event Display

/beauty1b/ronquest/pmgdata/k
tev99raw1/tapes1and2vac.dat

Run Number: 13602
Spill Number: 279
Event Number: 21584707
Trigger Mask: 3
All Slices

Track and Cluster Info

HCC cluster count: 2

ID Xcsi Ycsi P or E

T 1: -0.5194 -0.8033 -10.38
C 4: -0.5278 -0.8082 1.57

T 2: 0.5018 0.4753 +20.02

C 1: 0.5226 0.4737 9.53

C 3: 0.1966 -0.1837 5.08

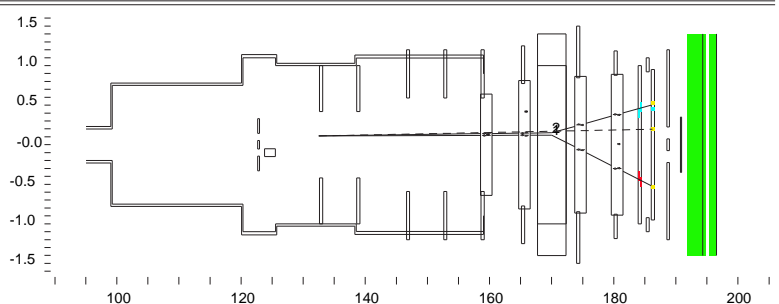
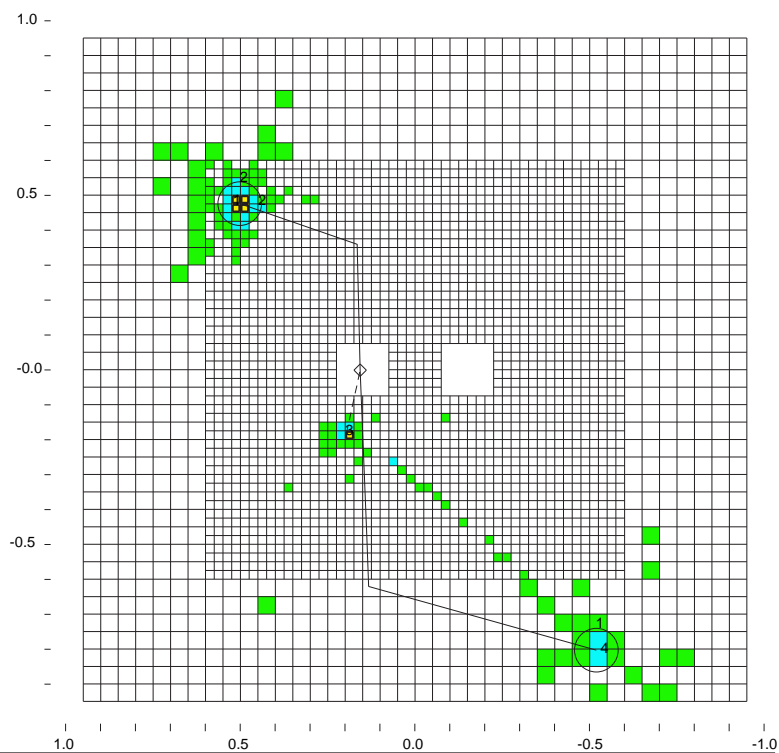
C 2: 0.4508 0.4725 0.88

Vertex: 2 tracks, 1 clusters

X Y Z
0.1120 -0.0009 132.469

Mass=0.4923 (assuming pions)

Chisq=1.05 Pt2v=0.000006



- - Cluster
- - Track
- - 10.00 GeV
- - 1.00 GeV
- - 0.10 GeV
- - 0.01 GeV

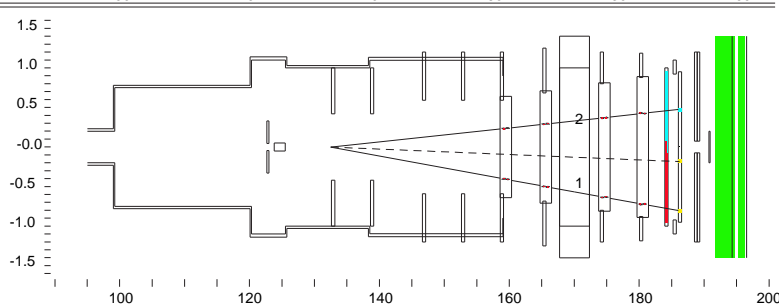


Figure 4.1: Calorimeter track and photon clusters for a typical $K_L \rightarrow \pi^+ \pi^- \gamma$ event

Chapter 5

Data Reduction and Signal Extraction

5.1 The Level 1 and 2 Trigger Requirements

There were sixteen beam triggers defined for E832: the two primary $\pi^+\pi^-$ triggers plus 14 others. Most of the 14 remaining triggers were looser, pre-scaled versions of the signal triggers designed to collect data for trigger inefficiency studies, but others were used to select rare kaon and hyperon decay events. Trigger 16, the accidental trigger, was especially important, since it recorded data on the underlying detector activity for use in the Monte Carlo simulation. The $K_L \rightarrow \pi^+\pi^-\gamma$ data sample was collected using the η_{+-} trigger (trigger 1), the same trigger used to select the $K_L \rightarrow \pi^+\pi^-$ data for the ϵ'/ϵ analysis. The η_{+-} trigger was unprescaled and had a trigger definition abbreviated as:

Level 1: SPILL * 2V * VEWUD * DC12 * VETO_CHRG

Level 2: 2HCY_LOOSE * YTF_UDO_M

Where

- SPILL = beam delivered from Tevatron.
- 2V = VV' hit counting: 2 hits in V, 1 hit in V' (or vice versa).

- VEWUD = VV' East-West-Up-Down: 1 track in the East side of the hodoscope, and 1 in the West. Plus, 1 track must be in the upper portion and the other in the lower portion.
- DC12 = 3 "DC-OR" hits in the 4 possible views.
- VETO_CHRG = No appreciable energy in regenerator, SA, CIA, or MU2 veto counters.
- 2HCY_LOOSE = Drift Chamber hit counting: Require 2 in-time DC hits in at least 3 of the 4 y views.
- YTF_UDO_M = YTF records 1 upward-going and 1 downward-going y track, with overlap in the center region of the chamber. Marginal quality of 1 track was accepted.

A few of these trigger requirements will be described in more detail in the upcoming sections. Note, however, that none of the trigger requirements listed above required calorimetry information. This will become significant in the upcoming discussion of the level 3 trigger definitions.

5.1.1 The Trigger Hodoscope Requirement

The trigger hodoscope banks (VV') were the primary Level 1 element. An event must be recorded with 2 tracks in one bank and at least one in the other. This definition was chosen over the more restrictive 2-tracks-in-each-bank requirement in order to accept events that might have passed through a crack between paddles in one of the two banks.

The East-West-Up-Down requirement was designed to cut $\pi^+\pi^-$ tracks that had scattered somewhere between the target and the decay vertex (i.e. events with

non-zero transverse momentum).

5.1.2 The DC-OR Requirement

The DC-OR requirement [32] was another critical element of the level 1 trigger. Since the hodoscope banks were downstream of the drift chambers, it was possible for a kaon to decay downstream of the drift chamber and still produce charged decay tracks that satisfied the trigger hodoscope requirements. These events were exceedingly difficult to reconstruct and it was therefore desirable to remove them from the fiducial sample at trigger level. The difficulty lay in the fact that the lengthy 200 ns maximum drift time of the drift chambers made it fairly impractical to process chamber hits in a fast trigger.

The key to the success of the DC-OR requirement was the recognition that a particle passing between two adjacent sense wires must leave a hit in one of the two wires in less than half the maximum drift time (i.e. in under 100 ns)¹. Therefore, by taking the logical OR of the two wires, the hit information could be passed to the Level 1 trigger decision on a sufficiently rapid timescale. The final trigger definition required receipt of hit signals from drift chambers 1 and 2 (DC3 and DC4 were not used in Level 1) within 90 ns of a trigger hodoscope hit.

In order to produce the DC-OR signal, the two drift chambers were represented as a collection of "paddles" that were eight and a half cells wide and contained 16 sense wires apiece. The logical OR of each paddle was taken and sent to a central controller that counted the number of hits in each view. Both the x and y views were instrumented, and the trigger required that there be fired paddles in 3 of the 4 possible views.

The DC-OR logic reduced the Level 1 output rate by greater than a factor of

¹In fact, the average particle drift time was only ~ 60 ns.

two.

5.1.3 The Veto Requirement

A η_{+-} trigger event was vetoed at Level 1 if at least 0.5 GeV of in-time energy was deposited into any Ring Counter (RC), Spectrometer Anti (SA), or Cesium Iodide Anti (CIA) paddle. This requirement was useful in reducing the acceptance rate of $K_L \rightarrow \pi^+\pi^-\pi^0$ events into the final $K_L \rightarrow \pi^+\pi^-\gamma$ sample.

5.2 The Level 3 Trigger

The Level 3 trigger (as previously discussed in section 3.2) was a software filter that reconstructs events from the on-line values and "tags" events that appear to fit the description of one or more decay modes of interest. Tagging requirements were generally fairly loose and events were allowed to be tagged as more than one decay. The primary requirements for the $K_L \rightarrow \pi^+\pi^-\gamma$ tag in the η_{+-} trigger (trigger 1) was that the event should have 2 tracks with an energy/momentum ratio less than 0.9, at least one good vertex candidate, at least one photon cluster candidate with energy greater than 1.0 GeV, and a combined $\pi^+\pi^-\gamma$ invariant mass of at least 450 MeV. In addition, since the calorimeter was not automatically unpacked in trigger 1 (in order to speed the trigger rate), any events that otherwise would have been rejected by the non-calorimeter information alone were given an additional "on-line pp0kine" cut that cut against the kinematics of the $K_L \rightarrow \pi^+\pi^-\pi^0$ decay mode² in order to avoid throwing away good $K_L \rightarrow \pi^+\pi^-\gamma$ events unnecessarily.

However, many of the $K_L \rightarrow \pi^+\pi^-\gamma$ tagged events also satisfied the very similar, but slightly looser (and 1/7 pre-scaled) trigger 2 in addition to trigger one. Therefore, since the calorimeter was always unpacked for trigger 2 events, at least

²the pp0kine cut kinematics are discussed in more detail in section 5.4.4

1/7 of the $K_L \rightarrow \pi^+\pi^-\gamma$ events passed the level 3 trigger during the data run without ever having the special "on-line pp0kine" cut applied.

To deal with this, an off-line level 3 job was (much) later run on the $K_L \rightarrow \pi^+\pi^-\gamma$ tag events a second time to ensure that the pp0kine cut was applied to all events. This meant that, in order to correctly reproduce this, all Monte Carlo also needed to be run through the Level 3 filter code two separate times, slowing the event processing considerably.

5.3 Data Reduction

By the end of the 1997 run, 4.9 billion events had been written to 2645 separate 15 GB magnetic tapes. However, since the events were written in the order that they were processed, that meant that all decay modes were spread out over all 2645 tapes. Therefore, it was necessary to reprocess the tapes before analysis could begin.

5.3.1 The Split

The first step in the data reduction process was to sort the events by their level 3 tag and rewrite them to separate tapes. This data "split" took 5 months to complete and required an additional 2897 tapes. The ~ 430 million events that were tagged as $K_L \rightarrow \pi^+\pi^-\gamma$ during the 1997 run were written to 293 separate tapes (labeled KZG097-KZG389).

5.3.2 The Crunch

Even 293 tapes was far too many to make analysis practical, so a second level of data reduction, called the "crunch", was done. The crunch code made loose, preliminary cuts on a number of the analysis cuts and can be summarized [33] as

follows:

- The Z component of the vertex was between 100 and 160 m.
- The track energy/momentum ratio was less than 0.9
- Pp0kine was less than -0.002
- Calorimeter cluster energy was at least 0.9GeV
- The separation between the track and photon clusters in the calorimeter was at least 18 cm
- The combined $\pi^+\pi^-\gamma$ momentum was at least 10 GeV
- The combined $\pi^+\pi^-\gamma$ invariant mass was between 0.460 and 0.540 GeV
- The transverse momentum squared of the combined $\pi^+\pi^-\gamma$ particle was less than 0.005

The exact definition and usefulness of each of these cut variables will be discussed at greater length in section 5.4. Roughly 2% of events with level 3 $K_L \rightarrow \pi^+\pi^-\gamma$ tags were written to 4 crunch tapes (KQH460-KQH463).

5.4 Signal Extraction

Extracting the desired signal events from all the other events that received the same tag required a very specialized set of requirements that were each tailored to a specific purpose. These requirements can be grouped into four general categories: reconstruction quality, fiducial and resolution constraints, particle identification and rejection, and signal mode kinematics. Each requirement will be discussed in detail, and plots of the agreement between the data and Monte Carlo in some these variables are shown in figures 7.6 through 7.5.

5.4.1 Reconstruction Quality Cuts

The analysis routine begins by checking the database to remove all "bad spill" events-i.e. events during runs or spills in which beam quality or detector performance were known to be poor. The tracking and calorimeter clustering information was then reconstructed and all signals from the veto detectors were checked with final calibrations to determine if any event in the sample should have triggered the veto counters even if they obviously had not during the original data-taking.

After reconstruction, exactly two tracks were required for acceptance, and, as mentioned in section 4.1.4, they needed to have x trajectories in opposing directions. In addition, the χ^2 agreements for both the vertex position and the x-trajectory offset at the magnet needed to be less than 50.

5.4.2 Fiducial and Resolution Cuts

A number of fiducial cuts were made to ensure that events in the final data sample struck the detector in regions where they could be reconstructed accurately. Events projected near the apertures of the veto detectors, or near the edges of drift chambers or trigger counters were all removed. In addition, x tracks were required to be well-separated (separation > 3 cm) at the calorimeter to avoid the chance of mis-pairing the x and y components of the tracks.

Strict requirements were also imposed on clusters in the calorimeter. Clusters with seeds near the outer edge or beam holes of the calorimeter were removed in order to ensure that all energy was recorded. Track and photon cluster candidate clusters were required to be separated by a minimum of 30 cm, which minimized both potential cluster overlaps and the effects of hadronic showering around the pion track clusters.

Photon clusters were also required to have a minimum energy of 1.5 GeV, well

above the calorimeter threshold of ~ 1 GeV. This cut had the added bonus of further cutting against the (generally low-energy) pion shower photons that might otherwise have been mistaken for a signal-mode photon. Clusters were additionally required to have a cluster shape χ^2 agreement of 48 or better (i.e. they needed to be symmetric around the seed crystal, rather than "blotchy", etc).

It is important to note that, even with all these restrictions on clustering, it was very common for events to have more than one photon cluster candidate. In order to choose the correct cluster, all candidate clusters were considered, and the one that satisfied all analysis cuts was selected. Moreover, any event that had more than one cluster that satisfied all cuts was removed from the sample.

5.4.3 Particle Identification and Rejection

Particle identification cuts were made to specifically target and remove events from background modes. Requiring that the ratio of the energy/momentum for the charged tracks be less than 0.85 was highly effective at removing events with electron tracks (such as $K_L \rightarrow \pi^\pm e^\pm \nu$), since electrons tend to have E/p values near 1.0.

In a similar vein, modes containing muon tracks (such as $K_L \rightarrow \pi^\pm \mu^\pm \nu$) were cut on by requiring that the momentum of each track be at least 8 GeV. This ensured that the muon tracks had sufficient energy to penetrate all the way to the muon vetoes and could thus be correctly detected and removed from the final event sample.

The $K_L \rightarrow \pi^+ \pi^-$ decay mode events could also potentially have mimicked the signal, provided a given event was paired with an accidental photon that just happened to have the right energy to meet the signal mode kinematic criteria. Therefore, since the combined invariant mass of the two pions alone should add up to the kaon mass (~ 0.498 GeV) for these decays, a cut was added to exclude any

events with a 2-pion invariant mass greater than 0.492 GeV.

In order to reduce the flux of the early-decaying K_S events, the z position of the vertex was required to be greater than 120.0 meters. There was also a high cut on the vertex z position, at 158.0 meters, that was actually a fiducial cut that ensured that the parent kaon decayed before reaching the vacuum decay window. The requirement that the combined $\pi^+\pi^-\gamma$ momentum (i.e. the momentum of the reconstructed kaon) should fall between 25.0 and 160.0 GeV was also useful in removing unwanted K_S events.

Perhaps the most important of the rejection cuts, however, was the so-called "pp0kine" cut, which was specifically designed to cut against $K_L \rightarrow \pi^+\pi^-\pi^0$ events, which were the primary background events to this analysis. It is defined as the square of the longitudinal momentum of the reconstructed π^0 in the frame in which the longitudinal momentum component of the $\pi^+\pi^-$ pair is zero, and is given by

$$p_{\pi^0}^2 \equiv \frac{(M_K^2 - M_{\pi^0}^2 - M_{\pi\pi}^2)^2 - 4M_{\pi^0}^2 M_{\pi\pi}^2 - 4M_K^2 (p_T^2)_{\pi\pi}}{4[(p_T^2)_{\pi\pi} + M_{\pi\pi}^2]} \quad (5.1)$$

where M_K^2 is the invariant mass-squared of the kaon mass, $M_{\pi^0}^2$ is the invariant mass-squared of the π^0 , $M_{\pi\pi}^2$ is the invariant mass-squared of the $\pi^+\pi^-$ pair, and $(p_T^2)_{\pi\pi}$ is the square of the transverse momentum of the $\pi^+\pi^-$ pair (relative to the kaon line of flight). A diagram illustrating the definition of PP0KINE is shown in figure 5.1.

Since it is the square of the momentum, this quantity should be greater than zero for all true $K_L \rightarrow \pi^+\pi^-\pi^0$ decays. However, since it was generally negative for $K_L \rightarrow \pi^+\pi^-\gamma$ events, it proved to be an extremely powerful method of discriminating against $K_L \rightarrow \pi^+\pi^-\pi^0$ in the final sample.

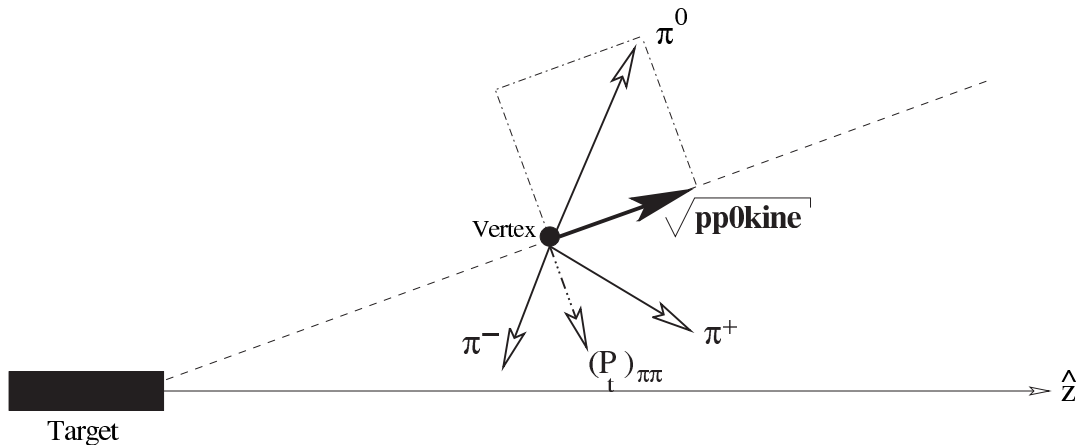


Figure 5.1: Definition of the PP0KINE kinematic variable. It is defined as the square of the π^0 longitudinal momentum in the frame in which the longitudinal $\pi^+\pi^-$ momentum is zero.

5.4.4 Kinematic Cuts

Kinematic cuts were those cuts made to specifically select on the distinguishing characteristics of the $K_L \rightarrow \pi^+\pi^-\gamma$ decay events. Probably the most obvious (and useful) of these cuts was the kaon mass cut. This cut required that, once the best photon cluster had been selected, the combined invariant mass of the three daughter particles in the decay— the π^+ , the π^- , and the photon - should reproduce the mass of the original parent kaon. In order to be accepted into the final sample, this $\pi^+\pi^-\gamma$ combined mass needed to fall between 0.48967 and 0.50567 GeV (i.e. $M_K \pm 0.008$ GeV).

Another important cut was the requirement that net transverse $\pi^+\pi^-\gamma$ momentum be less than $2.5 \times 10^{-4} (GeV/c)^2$. This cut took advantage of the fact that the combined momentum of the daughter particles (in this case, the π^+ , π^- , and γ) should align with the original kaon trajectory³. Therefore, discriminating against

³which was computed by drawing a line from the vertex back to the center of the production target

events with unusually large transverse components, relative to the kaon flight path, was an excellent way of removing unwanted events.

Finally, the photon energy in the kaon center of mass (i.e. the phase space variable " ω ") was required to be greater than 20 MeV, in accordance with the standard ω cutoff value used in the literature to avoid theoretical uncertainties at low photon energies.

It is worth noting at this point that the value of ω can be determined solely from the tracking information alone, according to the relation⁴

$$\omega = \frac{M_K^2 - M_{\pi\pi}^2}{2M_K} \quad (5.2)$$

In other words, the measurement of this critical phase space variable was obtained entirely independently of the calorimeter information! This was extremely advantageous, due to the fact that the pion tracking information was calibrated very accurately using data from the $K_L \rightarrow \pi^+\pi^-$ decay sample.

⁴see Appendix B for a derivation

Chapter 6

The KTeV Monte Carlo

The Monte Carlo simulation of the KTeV experiment was performed by a detailed custom generation program called KTEVMC. To make this work, models were created for each aspect of the detector and then calibrated using actual data events. As a result, a high level of agreement between real and simulated $K_L \rightarrow \pi^+\pi^-\gamma$ events was achieved (see figures 7.6 through 7.5).

6.1 Kaon Production

The kaon spectrum simulation was generated based on an extrapolation of the Malensek [34] parameterization of K^+ and K^- production by 450 GeV protons on a BeO target to higher energies. In this parameterization, the number of kaons (\mathbf{N}) with lab momentum \mathbf{P} into a solid angle $\mathbf{\Omega}$ is given by

$$\frac{d^2N}{dPd\Omega} = \frac{B}{400} \left[\frac{x(1-x)^A(1+5e^{-Dx})}{(1+P_t^2/M^2)^4} \right] \quad (6.1)$$

where \mathbf{x} is the ratio of \mathbf{P} to the momentum of the incoming proton beam, \mathbf{P}_t is the kaon transverse momentum relative to the incident beam direction, and parameters A, B, D, and M were all fit using the the experimental data.

Using the valence quarks in the incoming protons as a guide, the distribution

probabilities for K^0 and \bar{K}^0 were extrapolated as

$$K^0 \sim \frac{1}{2}(K^+ + K^-) \quad (6.2)$$

$$\bar{K}^0 \sim K^- \quad (6.3)$$

This model predicted the observed kaon energy spectrum to within $\sim 8\%$. It was then refined with a polynomial correction obtained using $K_L \rightarrow \pi^+\pi^-$ data.

6.2 Kaon Transport

The initial transverse position of the kaon in the production BeO target was based on measurements of the finite size of the incoming proton beam. The longitudinal production position was determined from an exponential profile of the interaction probability of protons on beryllium. Once the initial K^0 and \bar{K}^0 particles were produced, they were expressed as vectors in the K_L, K_S eigenstate basis. In vacuum, the transformation matrix was diagonal, with terms that simply represent the decay probabilities of the K_L and K_S states. In matter, the transformation matrices contained both off-diagonal and diagonal elements in order to correctly account for the differing K^0 and \bar{K}^0 material interaction properties.

As a practical matter, however, the K_S particles decayed extremely rapidly in the vacuum beam. Therefore, the vacuum kaon beam that reached the detector was almost entirely composed of pure K_L particles, except at very high neutral kaon energy (> 200 GeV).

After leaving the target, the kaons were propagated down the beamline. As they passed through the absorbers, there was a finite probability that the kaons would scatter. To simulate this, an exponential distribution based on lead or beryllium scattering probabilities was used to assign the appropriate transverse momentum

to the scattered kaons. Once through the absorbers, the generated kaons would pass through the neutral collimators.

6.3 Kaon Decay Tracing

The z position of the kaon decay was determined from decay probability distributions inputted into KTeVMC. Once the kaon decayed, all daughter particles except neutrinos were traced through the detector to the back-anti (BA). Muons were traced past the BA, through the filter steel, and all the way through the muon counters. Particles with trajectories that exited the fiducial region of the detector were no longer traced. In addition, the simulation program included an option to cease tracing an event when a daughter photon hit a photon veto counter and deposited enough energy to trigger the veto.

Secondary decays (such as $\pi \rightarrow \mu\nu$) and multiple scattering of daughter charged particles were accounted for. Electromagnetic interactions such as bremsstrahlung photon emission from electrons, and photon to e^+e^- pair conversion were also simulated.

6.4 Drift Chamber Simulation

Drift chamber hits were simulated by calculating the distance from the generated particle to the closest sense wire plane and then smearing it with a Gaussian distribution in order to simulate the position resolution of the chamber ($\sim 100 \mu\text{m}$). The resulting distance was then converted into a time using the known time vs. distance relationships measured from the data. However, this model was not sufficient to precisely simulate the observed data.

The two effects that required the most corrections were "high SODs" and "hit

inefficiencies”. High SODs (sums of distances)¹ occurred when the recorded SOD distance exceeded the size of drift cell. Hit inefficiencies occurred when particles passing through a drift cell failed to register as hits. Both of these effects turned out to be localized to specific regions in each chamber and to vary over the course of the run. Therefore ”DC maps” that accounted for these effects were saved into the database for each chamber and run.

Accidental events also required additional corrections. Accidentals that triggered a drift chamber cell prior to the ”in-time” window could obscure a hit from the simulated event particle. The drift chamber discriminator cards were designed to function with a 50 ns deadtime, but it turned out that these accidental events could occasionally produce very broad analog pulses that remained above the discriminator threshold for longer than 50 ns.

”Delta rays” (scattered electrons) could also produce spurious hits in the drift chamber. A study of the data showed that this effect was only relevant above a certain cutoff in secondary electron energy, and a model of this was added to the simulation.

6.5 Calorimeter Simulation

Since electromagnetic showers involve thousands of particles, the simulation of even a single shower was time-consuming. Therefore, running through the full simulation of each shower for many millions of kaon decays was impractical. Instead the GEANT particle simulation software package [37] was used to generate a library of several thousand simulated showers that was saved to the KTEVMC database [35, 36]. This library simulated a 13x13 array of small (2.5 cm x 2.5 cm) CsI crystals. This corresponded to a total transverse area of 32.5 cm x 32.5 cm that was divided

¹i.e. poor drift chamber tracking. See section 4.1.1 for more details on SOD calculations.

into $500 \mu\text{m} \times 500 \mu\text{m}$ bins. The larger (outer region) crystals were treated as conglomerates of 4 small crystals. The showers libraries included six generated energies (2, 4, 8, 16, 32, and 64 GeV) and 25 values of the mean longitudinal shower position, \bar{z} .

During generation, the Monte Carlo selected a shower based on the incident particle's initial energy (which was Gaussian smeared to simulate calorimeter resolution) and position in the 3×3 array. The generated \bar{z} was treated slightly different for photons and electrons and was produced according to

$$\bar{z}_e = 0.11 + 0.18 \ln E_e \quad (6.4)$$

$$\bar{z}_\gamma = 0.12 + 0.18 \ln E_\gamma \quad (6.5)$$

In order to produce a roughly continuous distribution, KTEVMC "interpolated" between the discrete shower energies in the library by randomly selecting a shower with either higher or lower energy than the generated particle and then reweighting between the two levels.

A separate library was used to simulate the approximately 30% of pions that showered in the calorimeter. The non-interacting pions were treated as minimally ionizing particles (MIPs) and were assumed to uniformly leave 320 MeV in the CsI. The pion showers were generated using GEANT (augmented by the FLUKA package for hadronic interactions) [37] to model a 41×41 array of small crystals. This array, with a transverse size of $102.5 \text{ cm} \times 102.5 \text{ cm}$, was considerably larger than the one used for photons and electrons, since pions generate much larger showers. Aside from the larger array size, and the correspondingly coarser transverse binning, hadronic showers were generated in manner very similarly to the electromagnetic ones.

The pion shower library contained approximately 900,000 shower events, separated into records of 3200 events apiece. Each shower record included the amount of energy deposited into each of the 1681 crystals as well as the type of primary interaction and whether hadronic secondaries were produced.

6.6 Accidental Activity

The high flux of the KTeV neutral beam made it natural to expect some level of underlying (“accidental”) activity. Stray particles from upstream kaon or hyperon decays, cosmic rays, and beam interactions with detector or target material were all likely sources of accidental events. Although most of these interactions simply caused the triggering systems to veto the events, there were some that arrived at the detector a few buckets later than the vetoed event. These could then have been reconstructed as early or in-time contributors to a later real event. They could manifest themselves in the data as drift chamber inefficiencies (ie early triggering, resulting in DC deadtime), spurious drift chamber hits, or additional particle energy in the calorimeter.

This effect was accounted for in the Monte Carlo by overlaying events from the “accidental trigger” on top of good generated events. The accidental trigger consisted of a counter telescope that was in close proximity to the neutral kaon production target, but oriented at a 90 degree angle. This configuration of the accident trigger provided a record of accidental activity directly from the data. The resulting distribution of accidental events was thus expected to closely resemble that found in the final real-event samples, since the flux in the accidental trigger was directly correlated to beam activity (which would not have been the case if a random trigger been used).

Since accidentals in the data could lead to spurious or inefficient triggering, it was important to accurately model the effect in the Monte Carlo when an accidental was superimposed upon a generated event. Therefore, the drift chamber TDC hits, veto and hodoscope counts, and CsI crystal energies from the accidental activity were all directly added to the generated event information prior to the evaluation of any trigger sources.

6.7 Trigger Simulation

The KTeV Monte Carlo simulated all elements of the trigger— including the hit-counting system (bananas and kumquats), the Hardware Cluster Counter (HCC), and the y-track finder (YTF)— and used the same binary trigger-definition maps that were used on-line during data taking. The only difference was that the memory-lookup algorithms that were originally done on hardware were now performed by software.

The output of the Monte Carlo triggers had a format identical to the real data; drift chamber TDC information, Level 1 source bits, and trigger bits were all included. This meant that the reconstruction code (i.e. the Level 3 trigger code) could be run on both data and Monte Carlo without changes and ensured that Monte Carlo events that passed Level 3 would be written to disk in the exact same format as the data.

Inputs to the DC-OR, banana, and kumquat logics used sources simulated from recorded digital drift chamber hits, with the hit counters assumed to be perfectly efficient. The Etotal and HCC simulations were slightly more complicated, since data-obtained threshold curves and high-energy inefficiencies for each individual calorimeter channel were used as inputs to the Monte Carlo model.

To save time, the trigger sources for photon vetoes were evaluated during particle tracing, and the generation would stop as soon as a particle failed a veto or a trigger decision.

Chapter 7

Likelihood Extraction of Matrix Element Parameters

7.1 A Brief Overview of Likelihood Analysis

The likelihood function is an extremely powerful tool for particle physics analysis. In fact, it is perhaps the single most accurate way to extract the best fit values of a given parameter set $\vec{\alpha}$; yet it is a surprisingly simple concept.

The likelihood function $L(\vec{\alpha})$ is defined as a product of individual probability functions $P_i(\vec{\alpha})$, specifically

$$L(\vec{\alpha}) = \prod_{i=1}^N P_i(\vec{\alpha}) \quad (7.1)$$

where N is the number of events.

This implies that the likelihood is the net probability over all individual probability functions. To extract the best fit values of $\vec{\alpha}$, one then simply maximizes $L(\vec{\alpha})$ with respect to $\vec{\alpha}$. In other words, one finds the value of $\vec{\alpha}$ that corresponds to the highest net probability.

7.2 The Likelihood Function for a Generalized Decay

We begin by defining a function $f(\vec{x}, \vec{\alpha})$ that describes the final decay probability density for any given set¹ of phase space variables \vec{x} and any set of fit parameters $\vec{\alpha}$. The function $f(\vec{x}, \vec{\alpha})$ can then, in turn, be described by

$$f(\vec{x}, \vec{\alpha}) = \mu(\vec{x}, \vec{\alpha})a(\vec{x}) \quad (7.2)$$

where $\mu(\vec{x}, \vec{\alpha})$ is the decay probability distribution and $a(\vec{x})$ is the function that describes the final detector acceptance (including detector constraints, triggering, and analysis cuts).

However, since $f(\vec{x}, \vec{\alpha})$ is not normalized, we introduce a new function

$$P(\vec{x}, \vec{\alpha}) \equiv \frac{f(\vec{x}, \vec{\alpha})}{\int_{V(\vec{x})} f(\vec{x}, \vec{\alpha}) d\vec{x}} \quad (7.3)$$

that is intrinsically normalized by construction according to

$$\int_{V(\vec{x})} P(\vec{x}, \vec{\alpha}) = 1 \quad (7.4)$$

Therefore, the corresponding likelihood function for N_d events in a given data set is

$$L(\vec{\alpha}) = \prod_{i=1}^{N_d} P(\vec{x}_i, \vec{\alpha}) = \prod_{i=1}^{N_d} \frac{f(\vec{x}_i, \vec{\alpha})}{\int_{V(\vec{x})} f(\vec{x}, \vec{\alpha}) d\vec{x}} \quad (7.5)$$

Taking the natural log of both sides, this becomes

$$\log L(\vec{\alpha}) = \sum_{i=1}^{N_d} \log \left[\frac{f(\vec{x}_i, \vec{\alpha})}{\int_{V(\vec{x})} f(\vec{x}, \vec{\alpha}) d\vec{x}} \right] \quad (7.6)$$

Using equation 7.2, this becomes

¹in this particular analysis $\vec{x} = \{\omega, \cos \theta\}$ and $\vec{\alpha} = \{\tilde{g}_{M1}, a_1/a_2, Ge1\}$

$$\log L(\vec{\alpha}) = \left\{ \sum_{i=1}^{N_d} \log [\mu(\vec{x}_i, \vec{\alpha})] + \sum_{i=1}^{N_d} \log [a(\vec{x}_i)] \right\} - N_d \log \left[\int_{V(\vec{x})} f(\vec{x}, \vec{\alpha}) d\vec{x} \right] \quad (7.7)$$

Monte Carlo techniques of numerical integration are then used to re-express the integral in the third term in a more useful form, specifically²:

$$\int_{V(\vec{x})} f(\vec{x}, \vec{\alpha}) d\vec{x} = V \langle f \rangle \quad (7.8)$$

where

$$\langle f \rangle \equiv \frac{1}{N_{uni}} \sum_{j=1}^{N_{uni}} f(\vec{x}_j, \vec{\alpha}) \quad (7.9)$$

and N_{uni} is the number of events uniformly distributed over the phase space V , and $f(\vec{x}_j, \vec{\alpha})$ is the weight of the j th event.

Now consider the specific case when the fit parameters are chosen at a given “baseline” value of $\vec{\alpha} = \vec{\alpha}_0$ and, after reweighting by the probability distribution function $f(\vec{x}_i, \vec{\alpha}_0)$, there are $N_{MC}(\vec{\alpha}_0) \equiv N_0$ Monte Carlo events. The original number of uniformly distributed events (N_{uni}) that was used to produce this sample can then be inferred as

$$N_{uni} = \sum_{i=1}^{N_0} \frac{1}{f(\vec{x}_i, \vec{\alpha}_0)} \quad (7.10)$$

Inserting 7.9 and 7.10 back into 7.8 gives

$$\int_{V(\vec{x})} f(\vec{x}, \vec{\alpha}) d\vec{x} = \left(\frac{V}{\sum_{i=1}^{N_0} \frac{1}{f(\vec{x}_i, \vec{\alpha}_0)}} \right) \sum_{j=1}^{N_{uni}} f(\vec{x}_j, \vec{\alpha}) \quad (7.11)$$

In addition, from equation 7.10 it can be seen that the sum over $j = 1, 2, 3, \dots, N_{uni}$ events in 7.11 can be replaced by a sum over $i = 1, 2, 3, \dots, N_0$ events if each event is given a reweighting factor of $\frac{1}{f(\vec{x}_i, \vec{\alpha}_0)}$ such that

$$\sum_{j=1}^{N_{uni}} f(\vec{x}_j, \vec{\alpha}) = \sum_{i=1}^{N_0} \left[\frac{1}{f(\vec{x}_i, \vec{\alpha}_0)} \right] f(\vec{x}_i, \vec{\alpha}) \quad (7.12)$$

²Note that this is essentially just the extension of the familiar “Second Fundamental Theorem of Integral Calculus”, $\langle f \rangle = \frac{1}{(b-a)} \int_a^b f(x) dx$, to multiple dimensions.

So, by inserting equation 7.12 into equation 7.11, the integral over any arbitrary $\vec{\alpha}$ can be expressed as

$$\int_{V(\vec{x})} f(\vec{x}, \vec{\alpha}) d\vec{x} = \left(\frac{V}{\sum_{i=1}^{N_0} \frac{1}{f(\vec{x}_i, \vec{\alpha}_0)}} \right) \sum_{i=1}^{N_0} \frac{f(\vec{x}_i, \vec{\alpha})}{f(\vec{x}_i, \vec{\alpha}_0)} \quad (7.13)$$

However, from equation 7.2 we know

$$\frac{f(\vec{x}_i, \vec{\alpha})}{f(\vec{x}_i, \vec{\alpha}_0)} = \frac{\mu(\vec{x}_i, \vec{\alpha})a(\vec{x}_i)}{\mu(\vec{x}_i, \vec{\alpha}_0)a(\vec{x}_i)} = \frac{\mu(\vec{x}_i, \vec{\alpha})}{\mu(\vec{x}_i, \vec{\alpha}_0)} \quad (7.14)$$

and therefore equation 7.13 reduces to

$$\int_{V(\vec{x})} f(\vec{x}, \vec{\alpha}) d\vec{x} = \left(\frac{V}{\sum_{i=1}^{N_0} \frac{1}{f(\vec{x}_i, \vec{\alpha}_0)}} \right) \sum_{i=1}^{N_0} \frac{\mu(\vec{x}_i, \vec{\alpha})}{\mu(\vec{x}_i, \vec{\alpha}_0)} \quad (7.15)$$

Inserting 7.15 back into 7.7 produces

$$\log L(\vec{\alpha}) = \left\{ \sum_{i=1}^{N_d} \log [\mu(\vec{x}_i, \vec{\alpha})] + \sum_{i=1}^{N_d} \log [a(\vec{x}_i)] \right\} - N_d \log \left[\left(\frac{V}{\sum_{i=1}^{N_0} \frac{1}{f(\vec{x}_i, \vec{\alpha}_0)}} \right) \sum_{i=1}^{N_0} \frac{\mu(\vec{x}_i, \vec{\alpha})}{\mu(\vec{x}_i, \vec{\alpha}_0)} \right] \quad (7.16)$$

With a little bit of algebra, we finally arrive at the desired form

$$\log L(\vec{\alpha}) = \sum_{i=1}^{N_d} \log [\mu(\vec{x}_i, \vec{\alpha})] - N_d \log \left[\sum_{i=1}^{N_0} \frac{\mu(\vec{x}_i, \vec{\alpha})}{\mu(\vec{x}_i, \vec{\alpha}_0)} \right] + Q(\vec{x}) \quad (7.17)$$

where

$$Q(\vec{x}) \equiv N_d \log \left[\frac{1}{V} \sum_{i=1}^{N_0} \frac{1}{f(\vec{x}_i, \vec{\alpha}_0)} \right] + \sum_{i=1}^{N_d} \log [\log a(\vec{x}_i)] \quad (7.18)$$

Note, however, that since $Q(\vec{x})$ has no $\vec{\alpha}$ dependence, it is convenient to define a new function \mathcal{L} such that

$$\mathcal{L}(\vec{\alpha}) \equiv \log[L(\vec{\alpha})] - Q(\vec{x}) = \sum_{i=1}^{N_d} \log [\mu(\vec{x}_i, \vec{\alpha})] - N_d \log \left[\sum_{i=1}^{N_0} \frac{\mu(\vec{x}_i, \vec{\alpha})}{\mu(\vec{x}_i, \vec{\alpha}_0)} \right] \quad (7.19)$$

The advantage of maximizing the sub-function \mathcal{L} instead of the complete $\log[L(\vec{\alpha})]$ is that we can determine the best-fit values of $\vec{\alpha}$ — with no loss of generality — without the need to undertake the (often very difficult) task of determining an explicit expression for the detector acceptance function $a(\vec{x})$.

7.3 Application of the Likelihood Function to $K_L \rightarrow \pi^+\pi^-\gamma$

7.3.1 The $K_L \rightarrow \pi^+\pi^-\gamma$ Likelihood Maximization Procedure

To do the $K_L \rightarrow \pi^+\pi^-\gamma$ analysis, equation (7.19) was coded into a Fortran 77 program that used the Powell Method of minimization/maximization given in *Numerical Recipes* [38] to determine a maximum likelihood values and a corresponding set of best-fit parameter values for $\vec{\alpha} = \{\tilde{g}_{M1}, \frac{a_1}{a_2}, G_{E1}\}$. This code included, among other things, the explicit expression for the $K_L \rightarrow \pi^+\pi^-\gamma$ differential decay rate function, given by equation (1.48).

There were only two required inputs to this program: a file containing the final event-by-event phase space distribution of the data, and a similar file (with all cuts made identical to the data) for the baseline Monte Carlo file. In order to improve statistical accuracy, the baseline Monte Carlo was generated to be fifty times as large as the actual data sample³.

A given likelihood fit using baseline Monte Carlos of this size (~ 6 million final events!) usually required 1-2 days of CPU time on a single 2.4 GHz node in the UVa HEP computer farm.

7.3.2 Determination of the Baseline Monte Carlo Size

Before the fit procedure could be run, the size of the “baseline” Monte Carlo needed to be ascertained. In principle a very large Monte Carlo sample was desirable, so that statistical variations between samples that differed only by a random seed would be very small. However, since the likelihood function (7.19) is a sum over the events, the computer CPU time is essentially directly proportional to the size

³see section 7.3.2 for further discussion on why this particular size of baseline Monte Carlo sample was chosen.

of the event sample. It was therefore important to strike a very careful balance between reducing the statistical error on the baseline sample (σ_{MC}) and keeping the CPU requirement at a somewhat reasonable level.

In practice, this meant finding a value of $Q \equiv N_{MC}/N_{Data}$ that essentially made $\sigma_{MC}^2/\sigma_{TOT}^2 \ll 1$. Noting that $\sigma_{TOT}^2 = \sigma_{MC}^2 + \sigma_{Data}^2$, the ratio of the statistical error of the baseline Monte Carlo to the total statistical error can be expressed as

$$\frac{\sigma_{MC}^2}{\sigma_{TOT}^2} = \frac{\sigma_{MC}^2}{\sigma_{MC}^2 + \sigma_{Data}^2} \quad (7.20)$$

Note that, in general, the statistical error (assuming a Gaussian distribution) falls off as $1/\sqrt{N}$, and therefore

$$\sigma_{MC}(Q) = \frac{\sigma_{MC}(Q=1)}{\sqrt{Q}} \equiv \frac{\sigma_0}{\sqrt{Q}} \quad (7.21)$$

where $\sigma_0 \equiv \sigma_{MC}(Q=1)$.

Finally, since, by definition, $N_{MC} = N_{Data}$ when $Q = 1$, the statistical error on the data sample should be roughly the same as that for a sample of size $N_{MC}(Q=1)$. That is

$$\sigma_{Data} \sim \sigma_{MC}(Q=1) \equiv \sigma_0 \quad (7.22)$$

Plugging (7.21) and (7.22) into (7.20), we get

$$\frac{\sigma_{MC}^2}{\sigma_{TOT}^2} \sim \frac{\frac{\sigma_0^2}{Q}}{\frac{\sigma_0^2}{Q} + \sigma_0^2} \quad (7.23)$$

which reduces to the very simple final expression of

$$\frac{\sigma_{MC}^2}{\sigma_{TOT}^2} \sim \frac{1}{Q+1} \quad (7.24)$$

From figure 7.1 we can see that our model suggested that little improvement of the final statistical error could be gained by using Q values greater than 40 or 50.

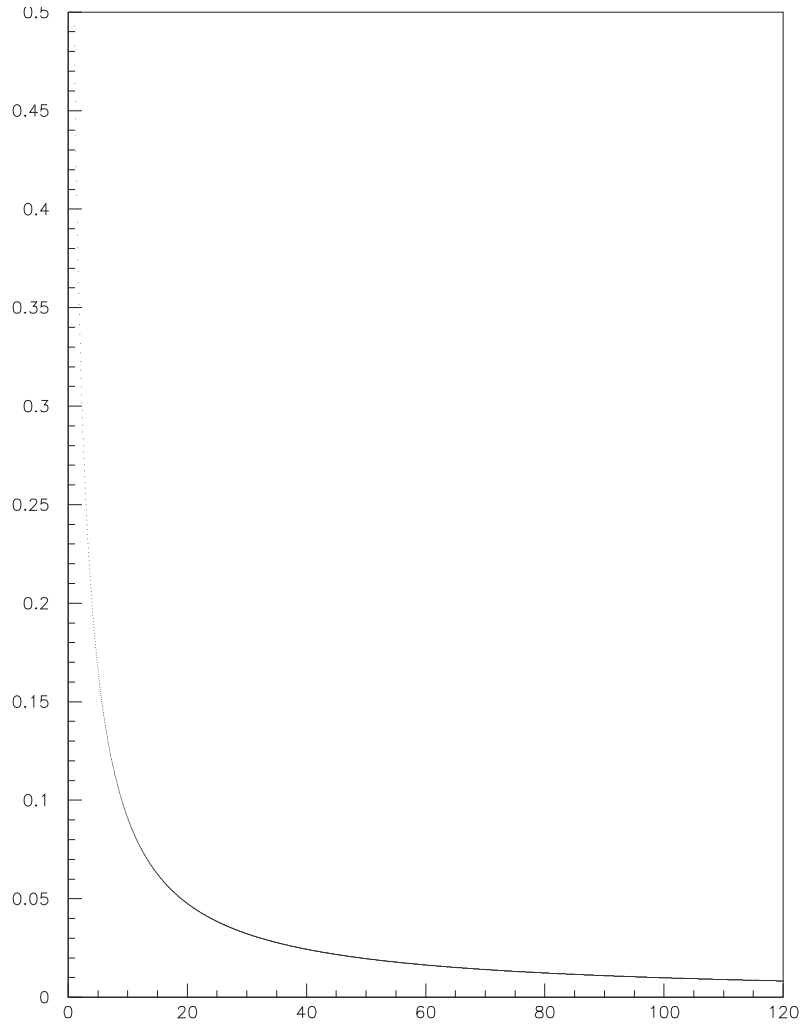


Figure 7.1: $\frac{\sigma_{MC}^2}{\sigma_{TOT}^2}$ vs Q

As a result, we chose to generate a baseline Monte Carlo that was 50 times the size of the data sample (i.e. $Q = 50$), which meant that the statistical fluctuations in the baseline were expected to contribute $\sim 1/(50 + 1) \cdot 100\% \sim 2\%$ to the total statistical error, while the fluctuations associated with the data were expected to contribute the remaining $\sim 98\%$.

7.3.3 Extraction Procedure for the \tilde{g}_{M1} and $\frac{a_1}{a_2}$ Best Fit Values

Once the maximum log-likelihood, $\mathcal{L}_{max}(\vec{\alpha})$, had been determined, a second program was run that iterated through a three dimensional grid of parameter values, centered on the maximum. The 1-sigma deviation from the maximum [39] was defined as the 3-D “error ellipsoid” that bounded all values of $\vec{\alpha}$ that produced a log likelihood value that was within 0.5 of the maximum. The 1-sigma statistical errors—adjusted for errors due to finite grid bin width—for parameters \tilde{g}_{M1} and $\frac{a_1}{a_2}$ were determined directly from this procedure.

An approximate best-fit value and upper limit for G_{E1} was also produced, though it was later refined using the method of Feldman and Cousins [40]⁴. The preliminary upper limit for G_{E1} proved to be useful, however, as an initial benchmark to determine the importance of systematic errors relative to statistical sensitivity.

Note that running a 3-D grid around the maximum likelihood value was extremely CPU intensive. It generally required 1-4 weeks of CPU per job, depending on the coarseness of the binning.

Once the best-fit values of the parameters had been extracted, a new Monte Carlo was generated at those values and compared to the data. This comparison demonstrated a high level of agreement in both spectrometer momentum resolution

⁴see section 8.2 for a full discussion

(figures 7.2 through 7.4) and track position (figure 7.5). Similar agreement was also seen in calorimeter cluster energy and position resolution (figures 7.6 through 7.10), and vertex determination (figures 7.11 through 7.13). The kaon flight trajectory (figure 7.14), and the overall kaon momentum spectrum (figure 7.15) were also modeled with a high degree of accuracy. Note that the data/Monte Carlo plots include linear best fits with the fit values and error for the slope (A1) and y-intercept (A0). In most cases, these values indicate that the best-fit line is within $\sim 1\sigma$ of flatness.

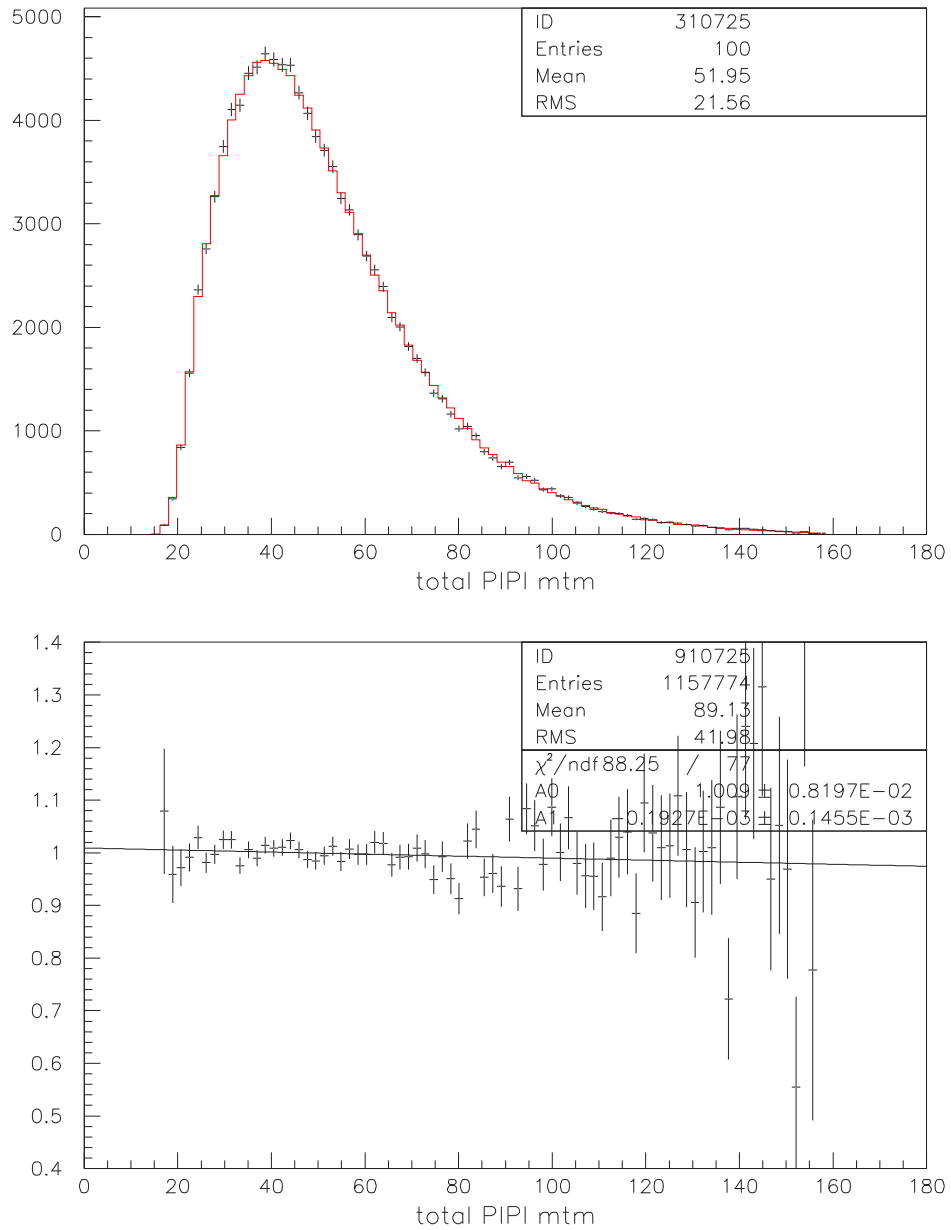


Figure 7.2: $\pi^+\pi^-$ combined momentum distribution (data, Monte Carlo).
Upper plot: $N_{events}/(1.8 \text{ GeV})$ vs. $P_{\pi^+\pi^-}$ (GeV/c). Crosses represent data.
Lower plot: Data/MC ratio vs. $P_{\pi^+\pi^-}$ (GeV/c).

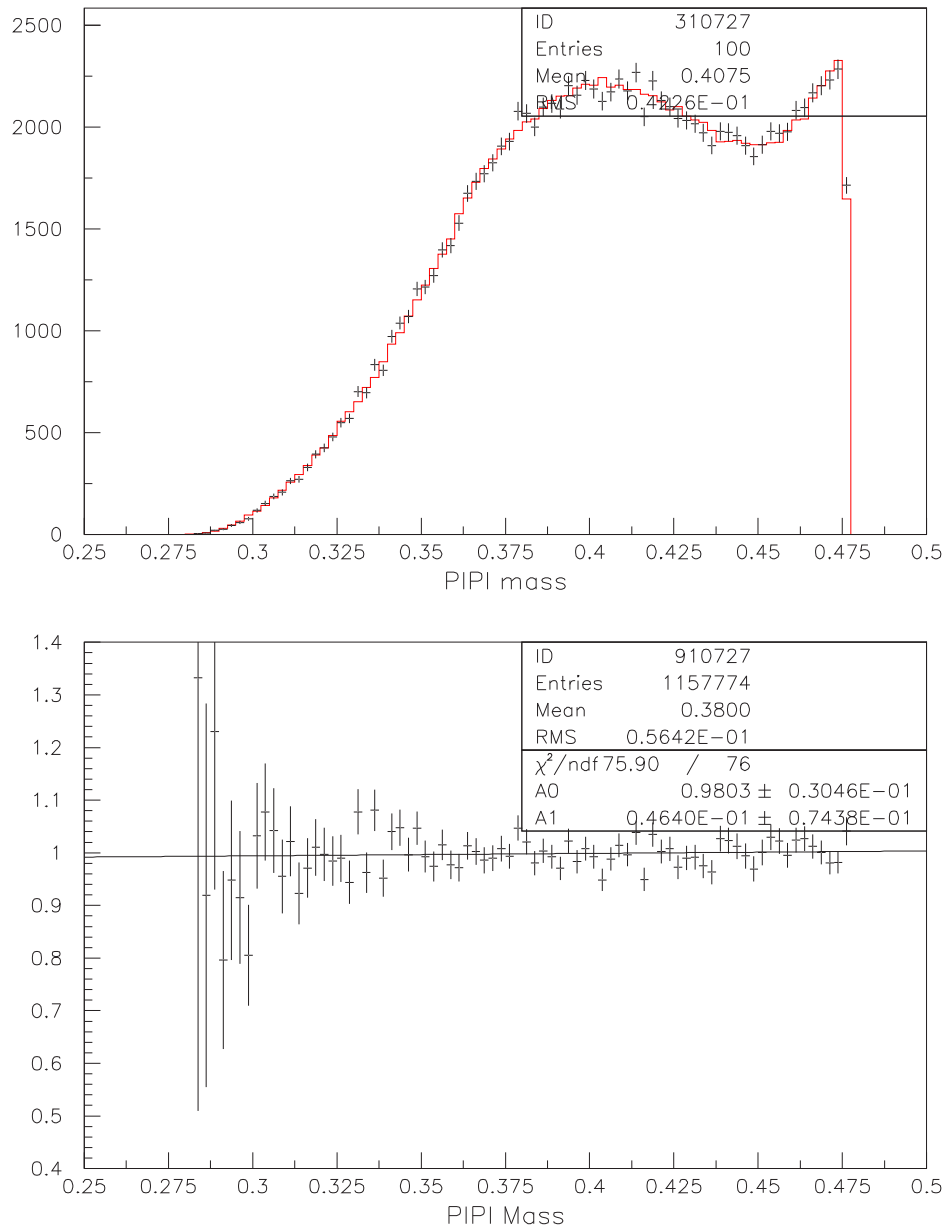


Figure 7.3: $\pi^+\pi^-$ invariant mass distribution (data, Monte Carlo).

Upper plot: $N_{events}/(2.5\text{MeV}/c)$ vs. $M_{\pi^+\pi^-}$ (GeV). Crosses represent data.

Lower plot: Data/MC ratio vs. $M_{\pi^+\pi^-}$ (GeV).

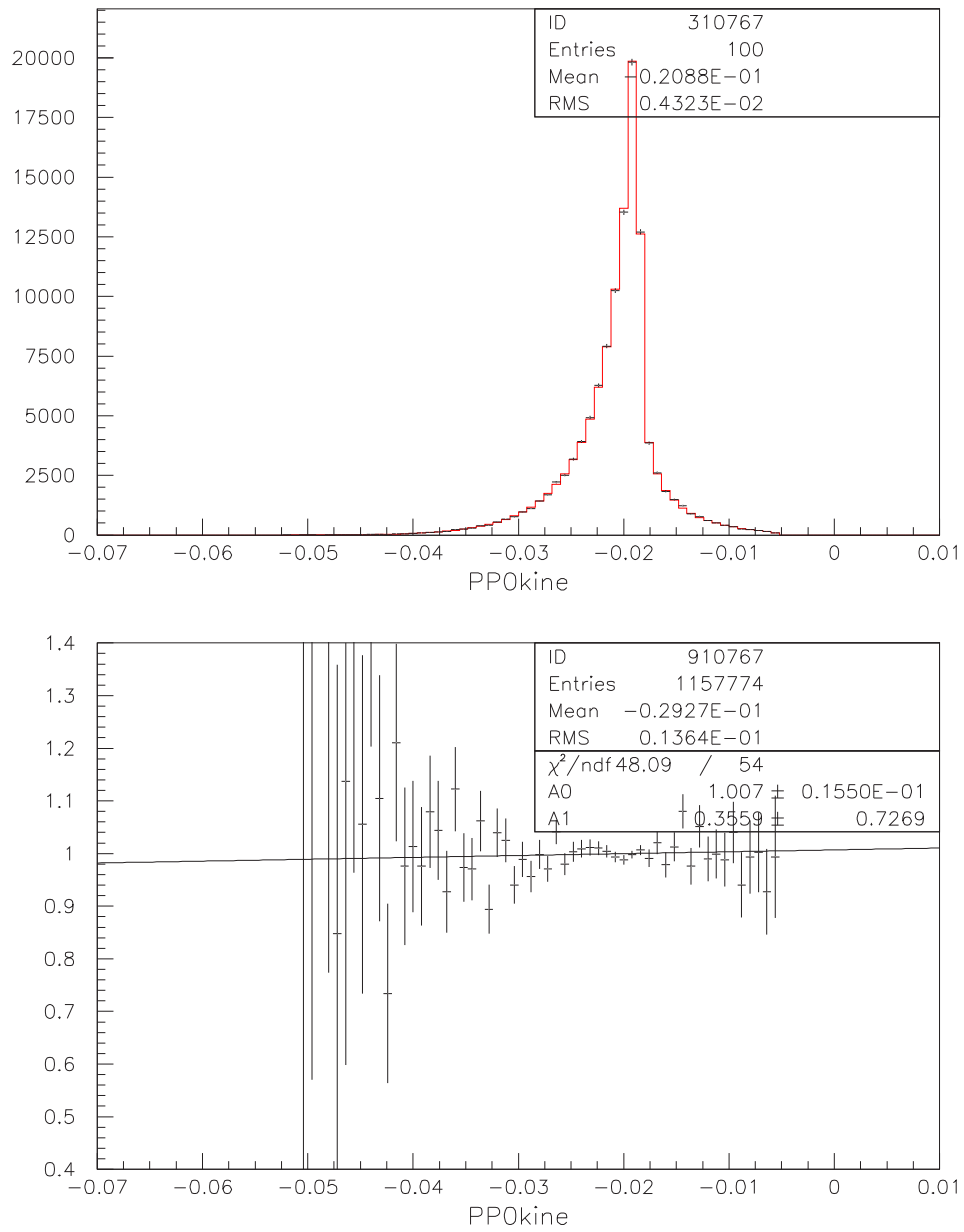


Figure 7.4: $\pi^+\pi^-\pi^0$ kinematic (“pp0kine”) distribution (data, Monte Carlo).

Upper plot: $N_{events}/(6 \times 10^{-4}(GeV/c)^2)$ vs. $pp0kine (GeV/c)^2$. Crosses represent data.

Lower plot: Data/MC ratio vs. $pp0kine (GeV/c)^2$.

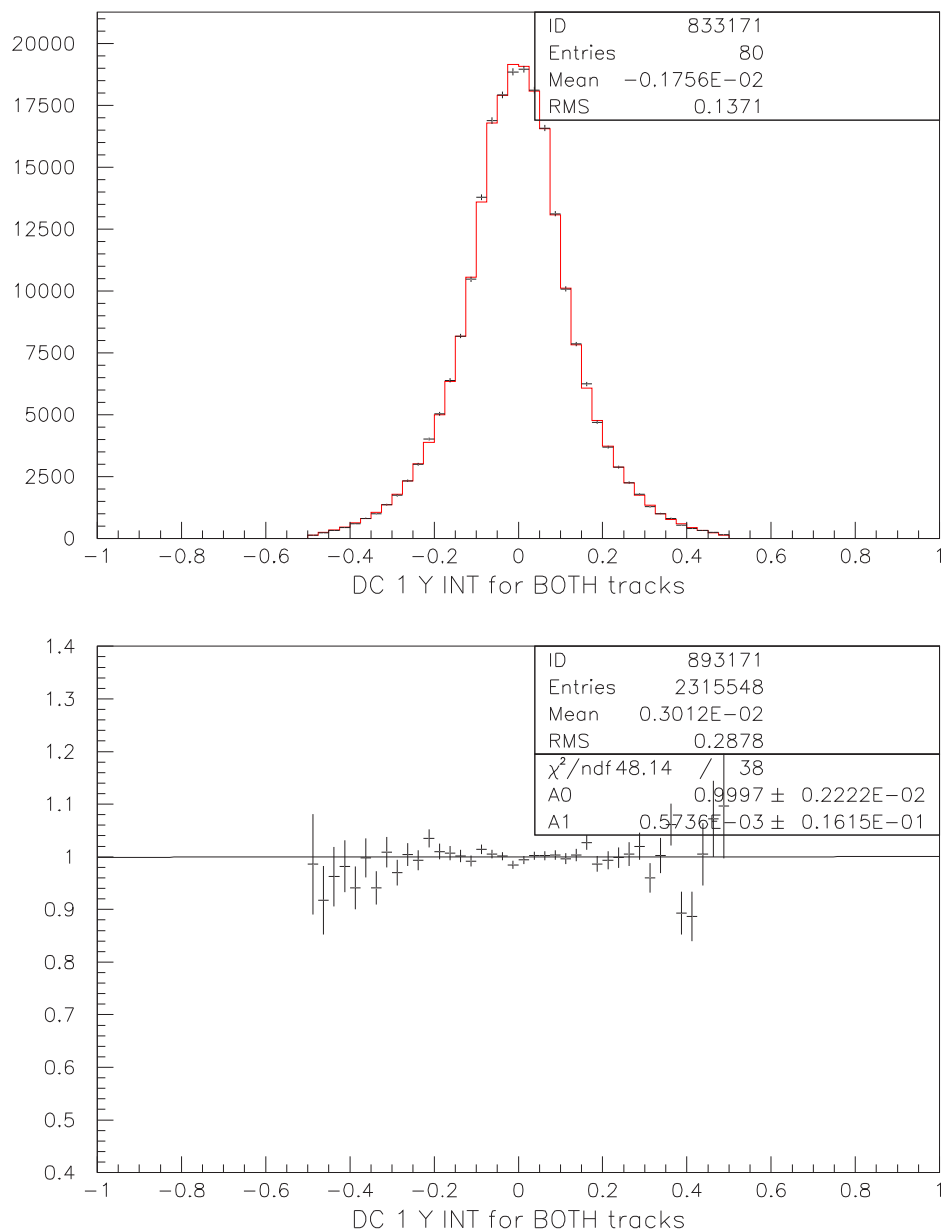


Figure 7.5: Two track hit illumination for Drift Chamber 1 (data, MC).
Upper plot: $N_{events}/(2 \text{ cm})$ vs. DC y-intercept (m). Crosses represent data.
Lower plot: Data/MC ratio vs. DC y-intercept (m).

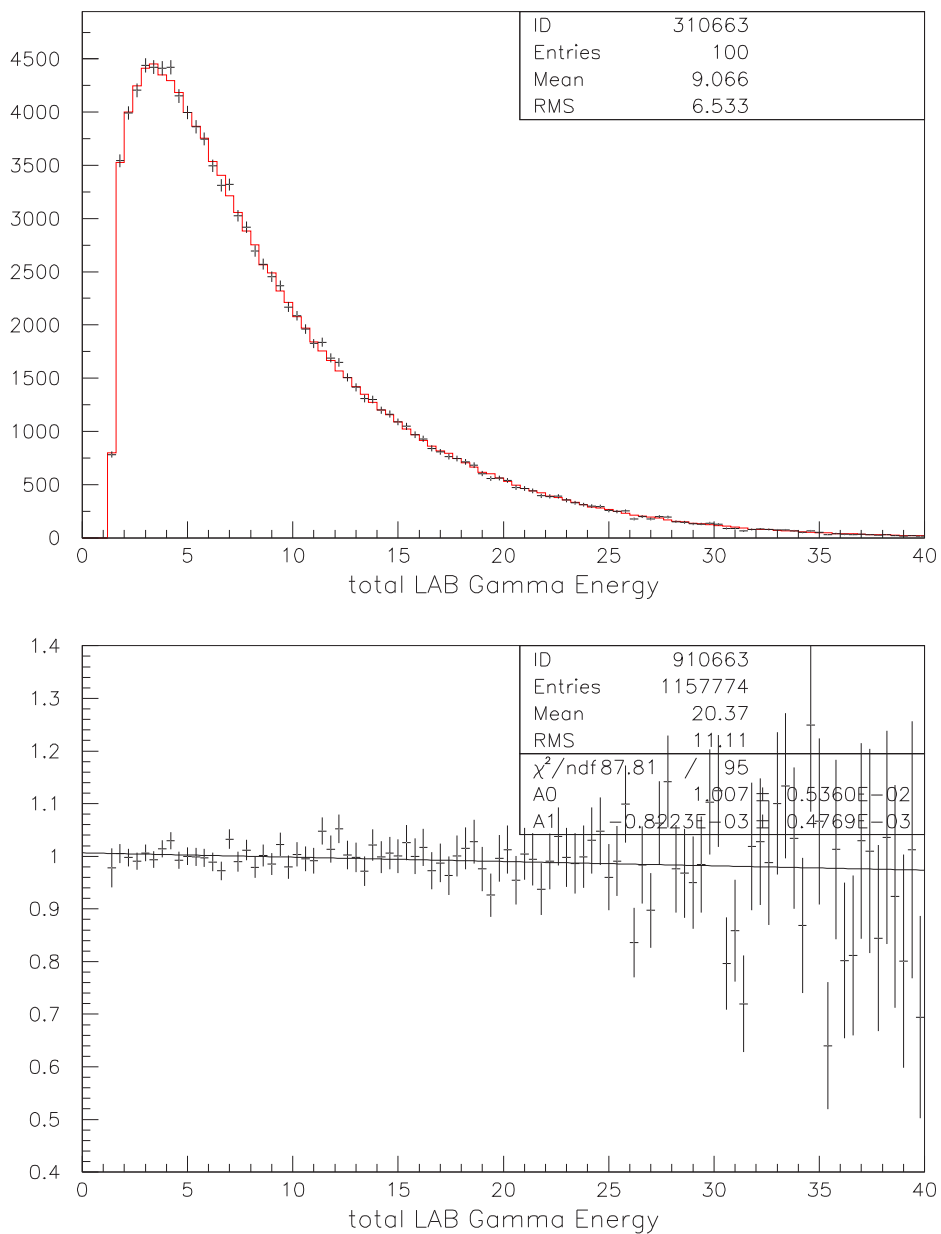


Figure 7.6: LAB frame photon energy distribution (data, Monte Carlo).
Upper plot: $N_{events}/(0.4 \text{ GeV})$ vs. E_γ (GeV). Crosses represent data.
Lower plot: Data/MC ratio vs. E_γ (GeV).

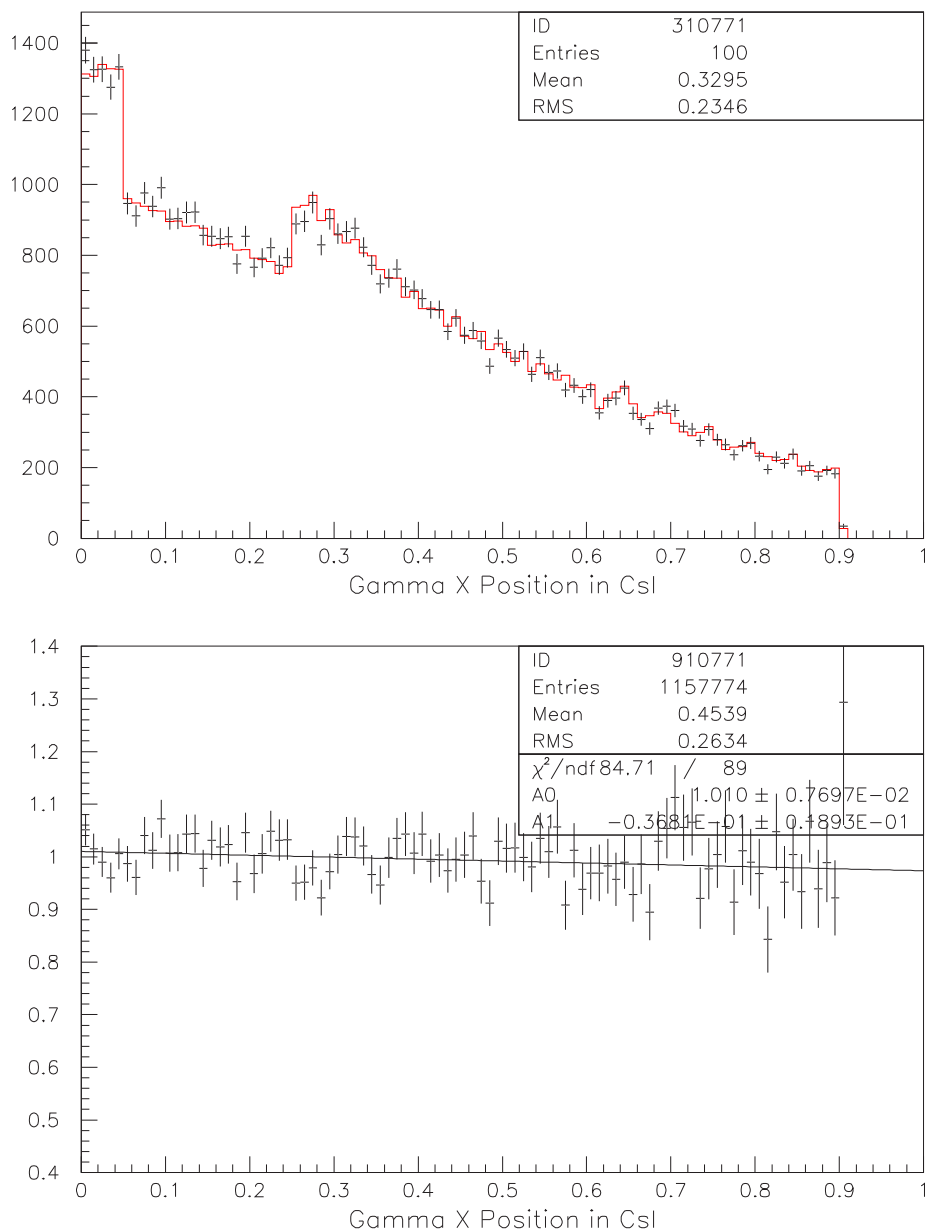


Figure 7.7: Photon X position in the Calorimeter (data, Monte Carlo).
Upper plot: N_{events}/cm vs. $|X|$ (m). Crosses represent data.
Lower plot: Data/MC ratio vs. $|X|$ (m).

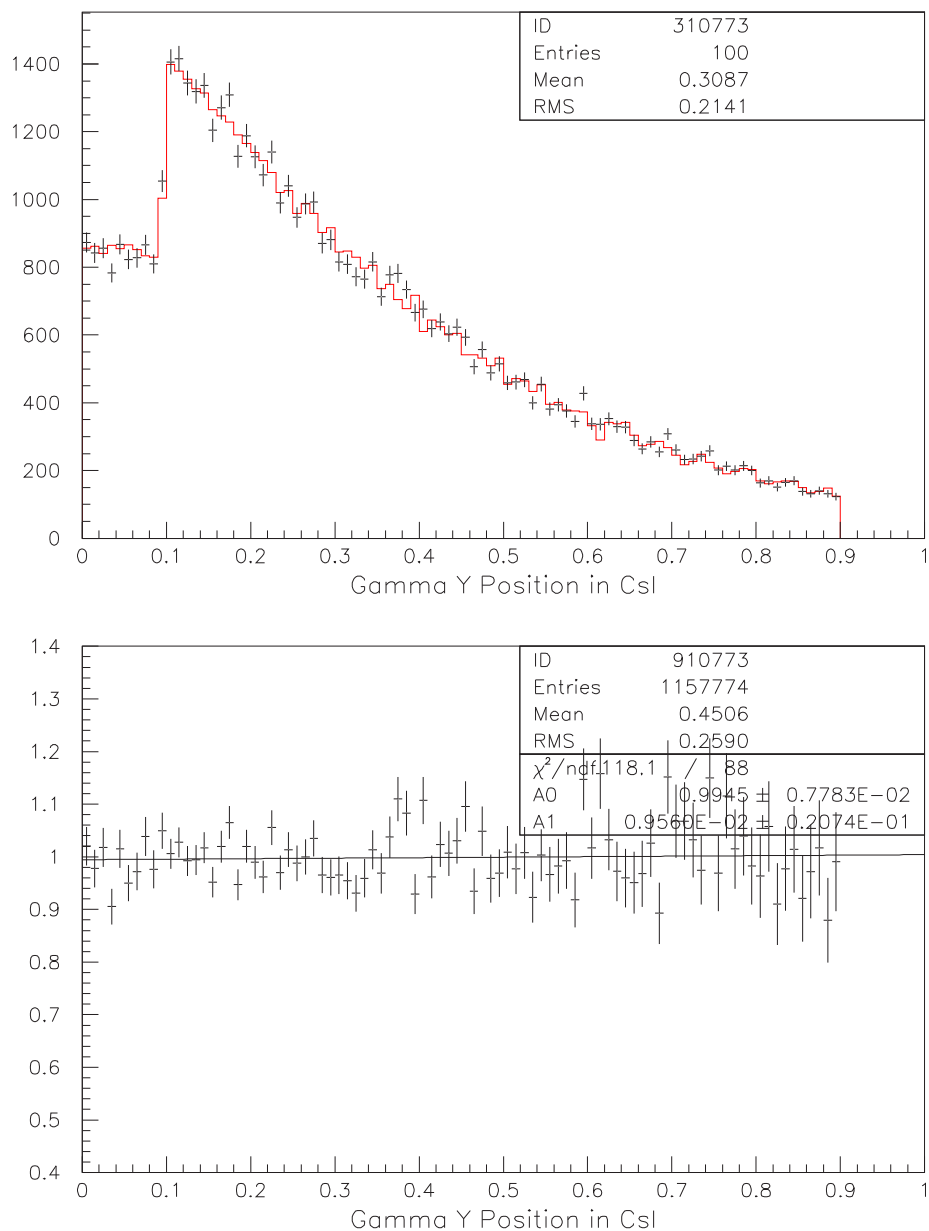


Figure 7.8: Photon Y position in the Calorimeter (data, Monte Carlo).
Upper plot: N_{events}/cm vs. $|Y|$ (m). Crosses represent data.
Lower plot: Data/MC ratio vs. $|Y|$ (m).

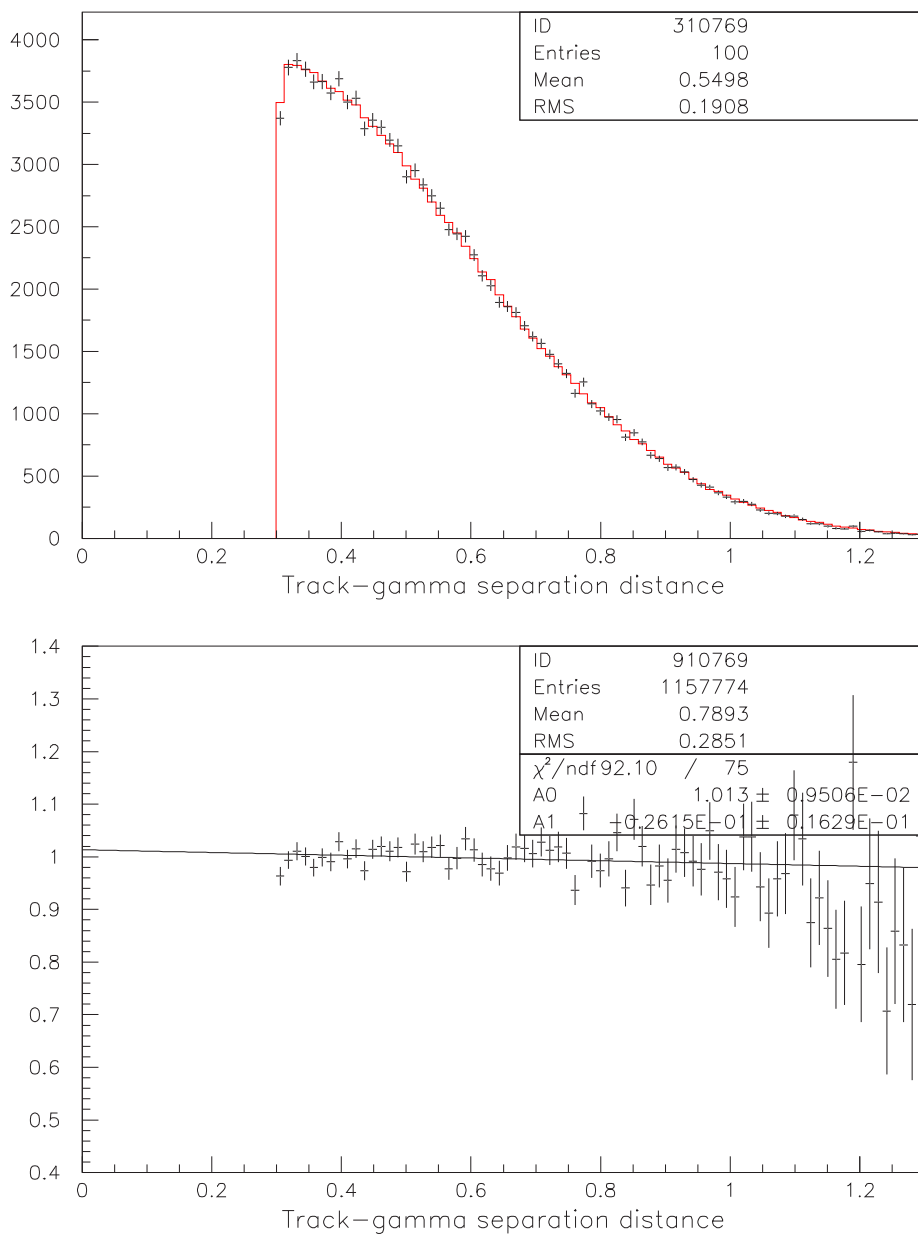


Figure 7.9: Track-photon separation in the calorimeter (data, Monte Carlo).
Upper plot: $N_{events}/(1.3 \text{ cm})$ vs. separation distance (m). Crosses are data.
Lower plot: Data/MC ratio vs. separation distance (m).

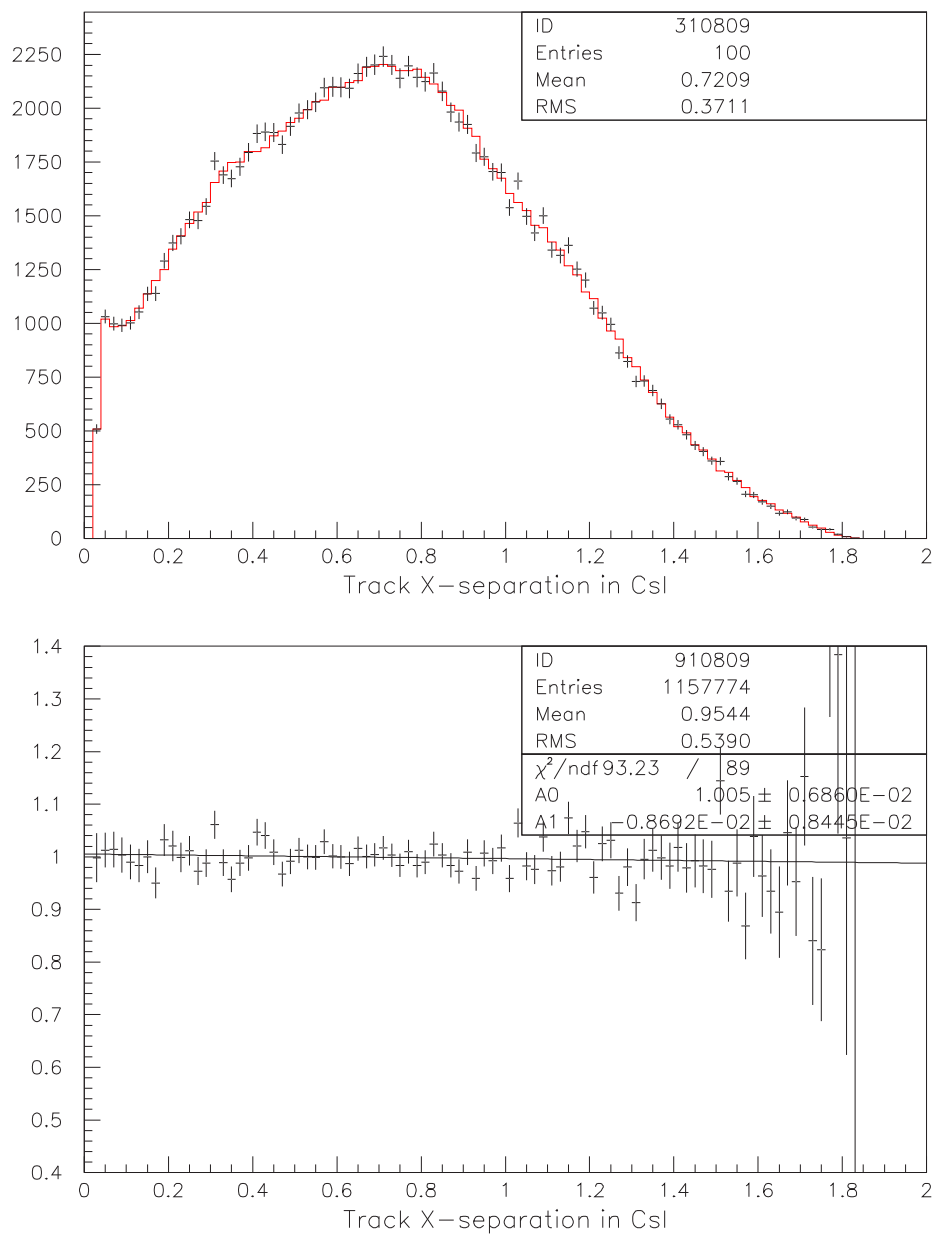


Figure 7.10: Track separation in the calorimeter (data, Monte Carlo).
Upper plot: $N_{events}/(2 \text{ cm})$ vs. track separation (m). Crosses are data.
Lower plot: Data/MC ratio vs. track separation (m).

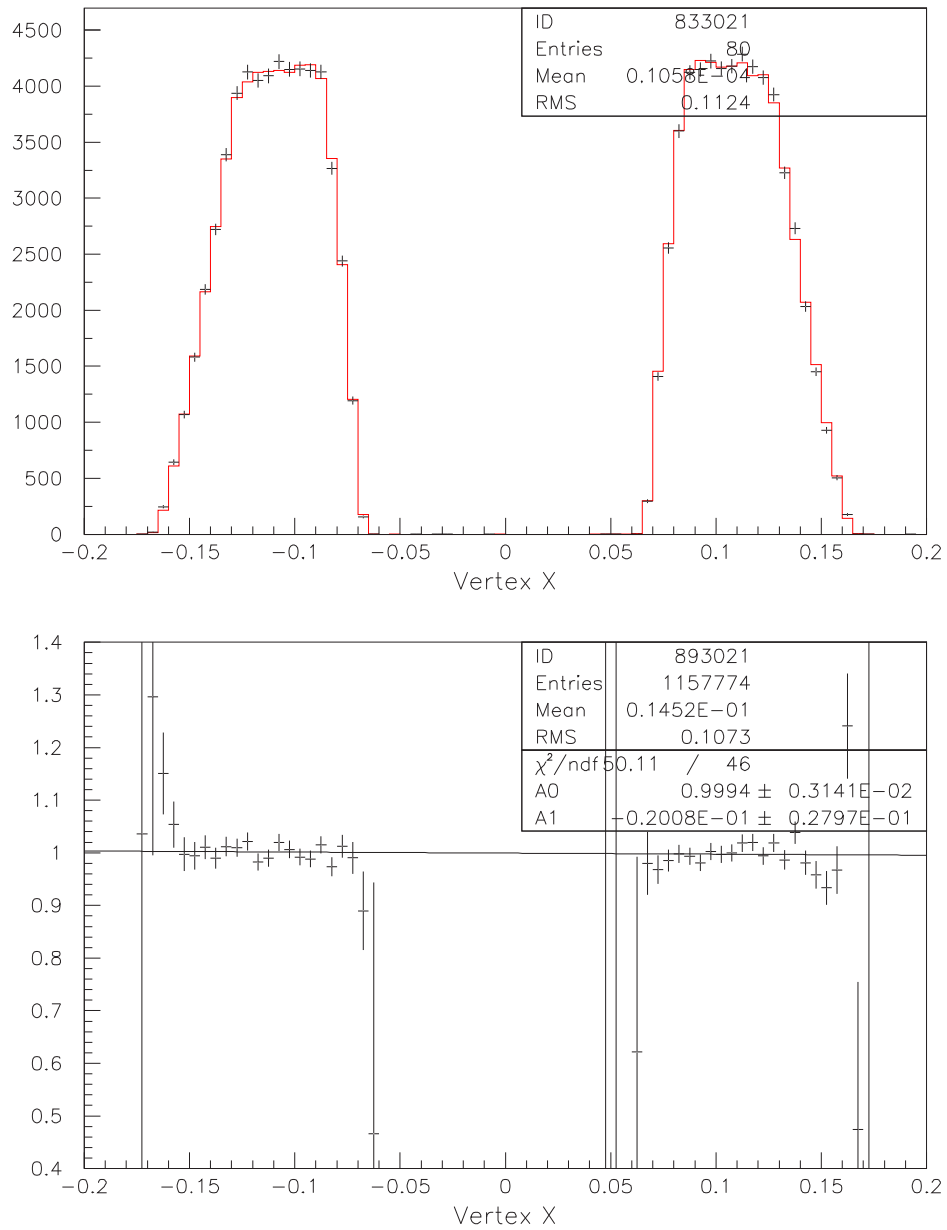


Figure 7.11: Vertex X position (data, Monte Carlo).

Upper plot: $N_{events}/(0.4 \text{ cm})$ vs. Vertex X (m). Crosses represent data.

Lower plot: Data/MC ratio vs. Vertex X (m).

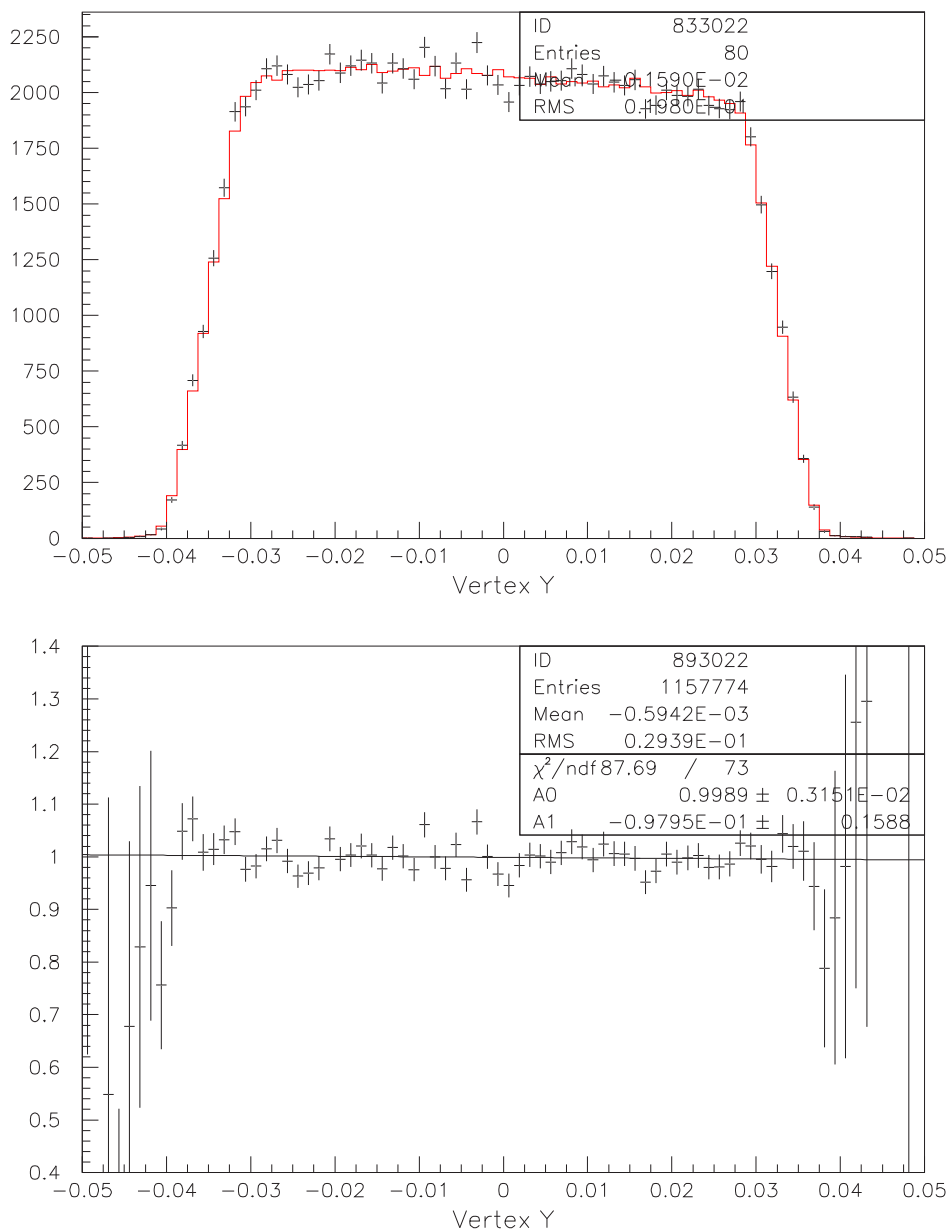


Figure 7.12: Vertex Y position (data, Monte Carlo).

Upper plot: N_{events}/cm vs. Vertex Y (m). Crosses represent data.

Lower plot: Data/MC ratio vs. Vertex Y (m).

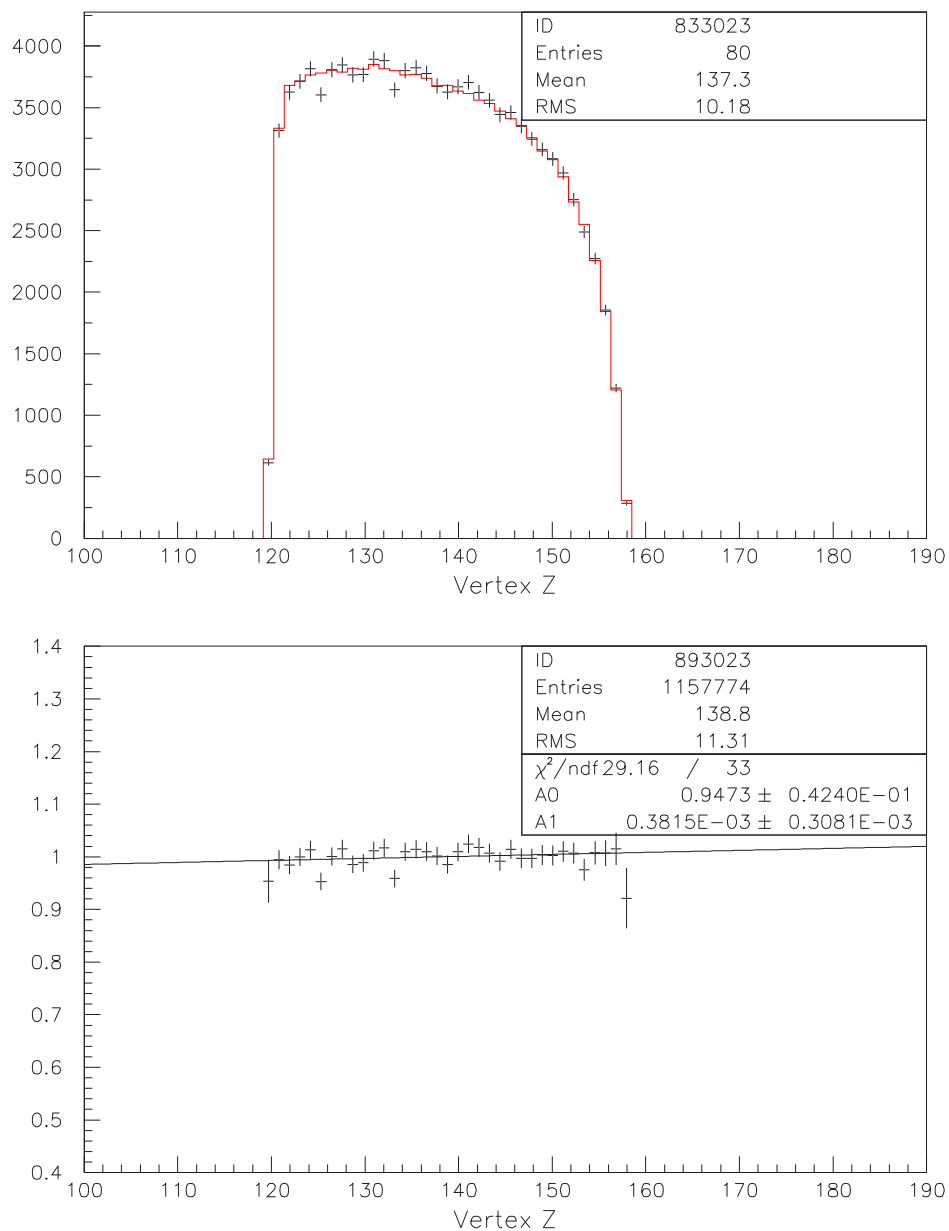


Figure 7.13: Vertex Z position (data, Monte Carlo).

Upper plot: $N_{events}/(0.9 \text{ cm})$ vs. Vertex Z (m). Crosses represent data.

Lower plot: Data/MC ratio vs. Vertex Z (m).

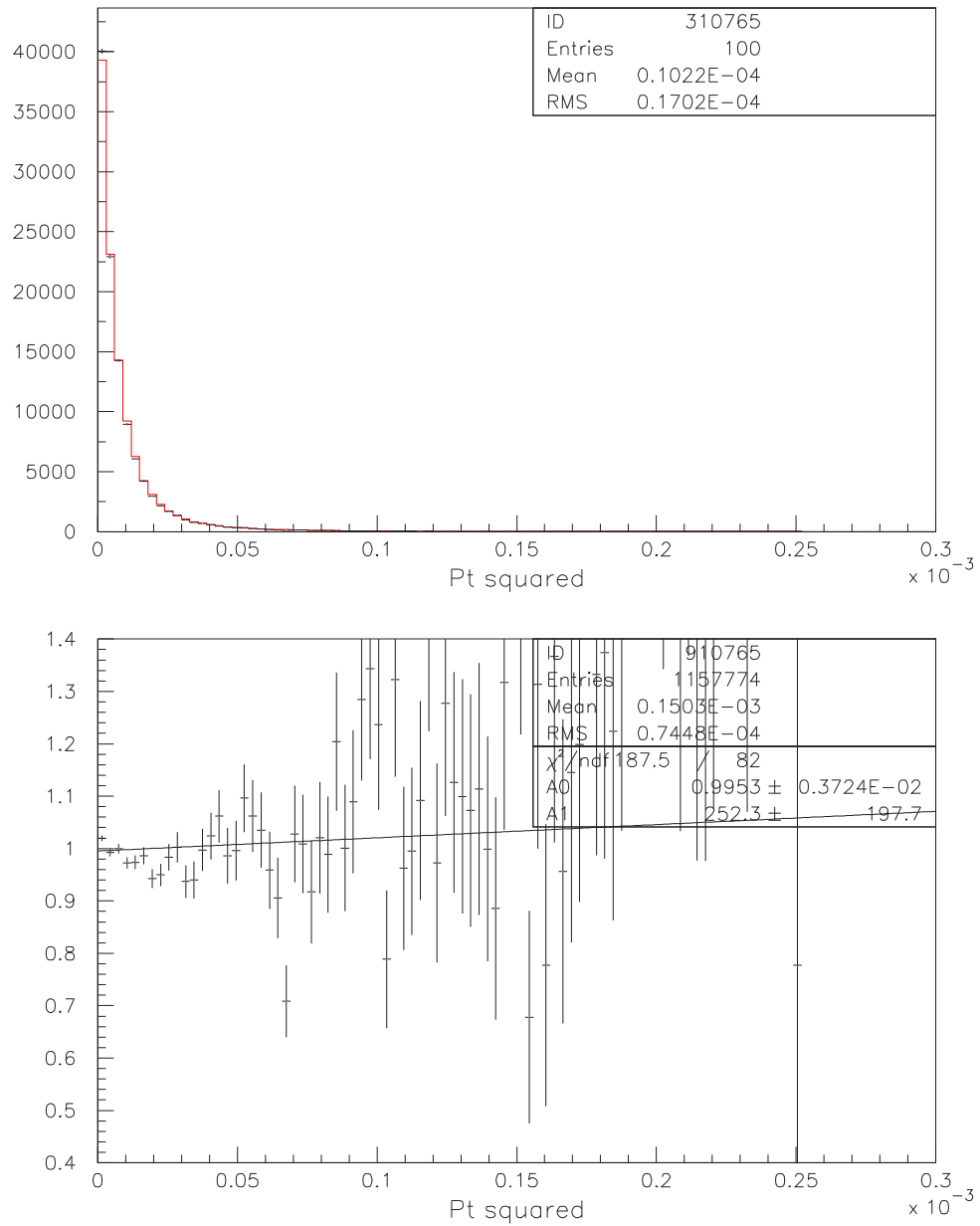


Figure 7.14: Kaon transverse momentum squared (data, Monte Carlo).
Upper plot: $N_{\text{events}}/(3 \times 10^{-6}(\text{GeV}/c)^2)$ vs. p_T^2 ($\text{GeV}/c)^2$. Crosses are data.
Lower plot: Data/MC ratio vs. p_T^2 ($\text{GeV}/c)^2$.

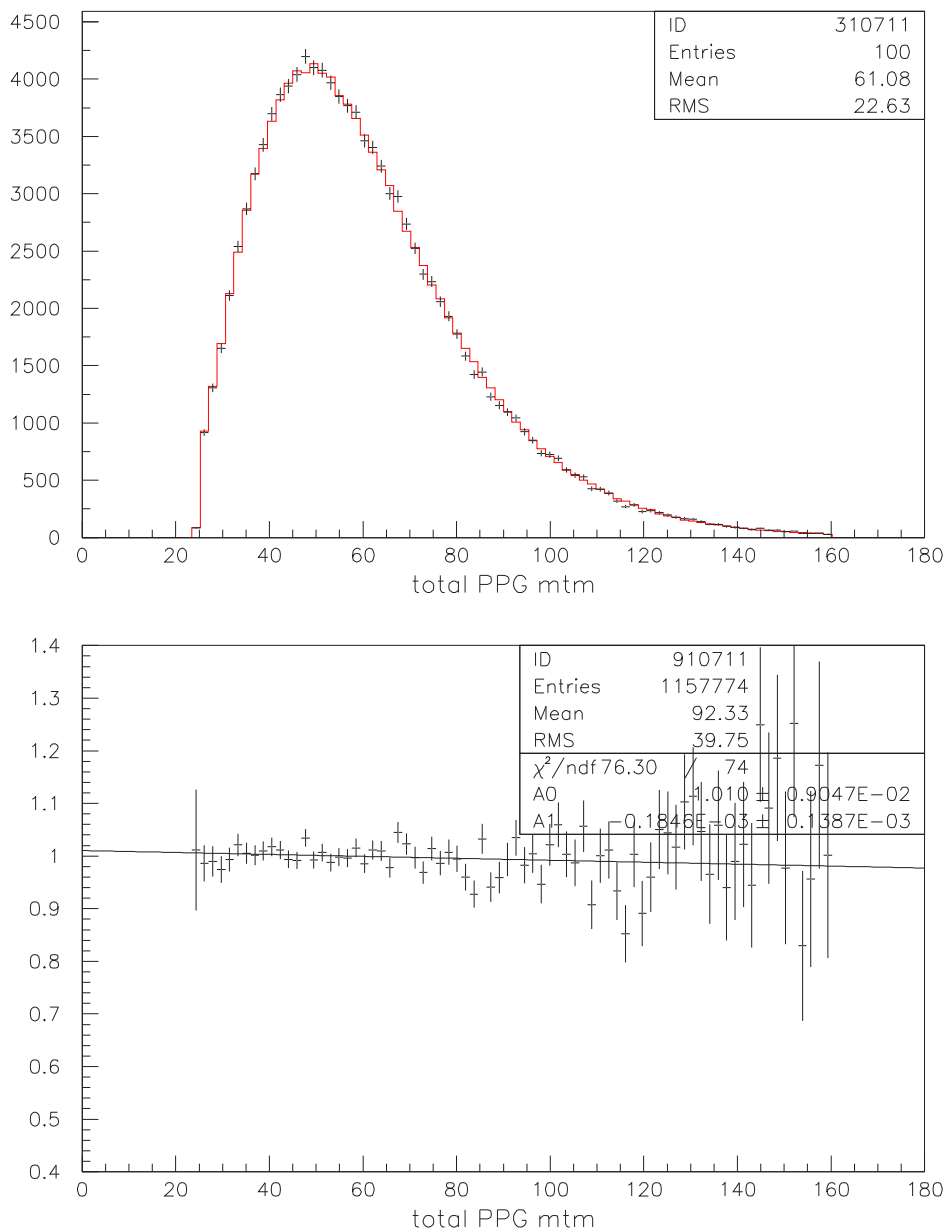


Figure 7.15: $\pi^+\pi^-\gamma$ combined momentum distribution (data, Monte Carlo).
Upper plot: $N_{events}/(1.8 \text{ GeV})$ vs. $P_{\pi^+\pi^-\gamma}$ (GeV). Crosses represent data.
Lower plot: Data/MC ratio vs. $P_{\pi^+\pi^-\gamma}$ (GeV).

Chapter 8

Extraction of Fit Parameters with Statistical Uncertainty

8.1 Extraction of the Best-fit Parameters

As per section 7.3.2, a nominal baseline Monte Carlo of $50N_{data}$ events was generated with input parameter values “in the vicinity” of the data ($\tilde{g}_{M1} = 1.20$, $\frac{a_1}{a_2} = -0.737$, and $G_{E1} = 0.04$). The Monte Carlo sample was run through the same triggers, crunch, and analysis code as the data. The phase space variables¹ (ω and $\cos\theta$) of the events passing the final cuts were written out to an output file, which in turn became the baseline distribution for the likelihood fitting and reweighting procedure.

The statistical error was then determined using a 3-D grid around the maximum log likelihood value, as described in section 7.3.3. A plot illustrating the locus of \tilde{g}_{M1} and $\frac{a_1}{a_2}$ grid values that produce a log-likelihood within 0.5 of the maximum is plotted in figure 8.1. Fitting the data in this manner produced results summarized in table 8.1.

Once the parameter values had been extracted, a new Monte Carlo was gener-

¹recall that ω was defined as the photon energy in the kaon CM frame, and $\cos\theta$ was defined as the angle between the π^+ and γ in the $\pi^+\pi^-$ CM frame.

Fit Parameter	Likelihood Best-fit	σ_{output} (stat)	$\sigma_{bin-size}$	σ_{net} (stat)
\tilde{g}_{M1}	1.229	0.035	0.003	0.035
$\frac{a_1}{a_2}$	-0.733	0.0072	0.0005	0.0072
G_{E1}	(0.00)	(≈ 0.07)	0.003	(≈ 0.07)

Table 8.1: Best-fit Parameter Values

ated using the new fit values as input. The phase space variable distributions that were then produced with this new Monte Carlo (figures 8.2 and 8.3) demonstrated an extremely high level of agreement with data.

Note that the value of G_{E1} and its statistical error are listed in paratheses, since the final G_{E1} will only be quoted as an upper limit, and its error bars will be determined more accurately via the method of Feldman and Cousins later in this chapter.

8.2 Determination of the statistical G_{E1} Upper Limit

Although the data fit routine produced an approximate statistical (1σ) upper limit on G_{E1} of ~ 0.07 , the fact that G_{E1} must be expressed as an upper limit, made it desirable to obtain a more conservative upper bound using the method of Feldman and Cousins [40]. To do this, nine data-sized Monte Carlos were generated using the best-fit values for \tilde{g}_{M1} and $\frac{a_1}{a_2}$ (i.e. $\tilde{g}_{M1} = 1.23$ and $\frac{a_1}{a_2} = -0.733$), and various values of G_{E1} , ranging from $G_{E1} = 0.11$ to $G_{E1} = 0.29$.

Each file was analyzed identically to the data, including analysis cuts, likelihood fitting, and error bar determination. The points were then plotted (figure 8.4) as Measured G_{E1} vs Generated G_{E1} , using 1.28 sigma error bars². A best-fit line was then made from the lower limits of the nine plotted points. This best-fit line

²A 1.28 sigma deviation in a Gaussian distribution encompasses 40% of events on each side of the mean. Therefore, 10% of events on each side of the mean are outside the 1.28 sigma range.

2-D Cross-Section of 3-D "Error Ellipsoid" (\tilde{g}_{M1} vs. $a1/a2$)

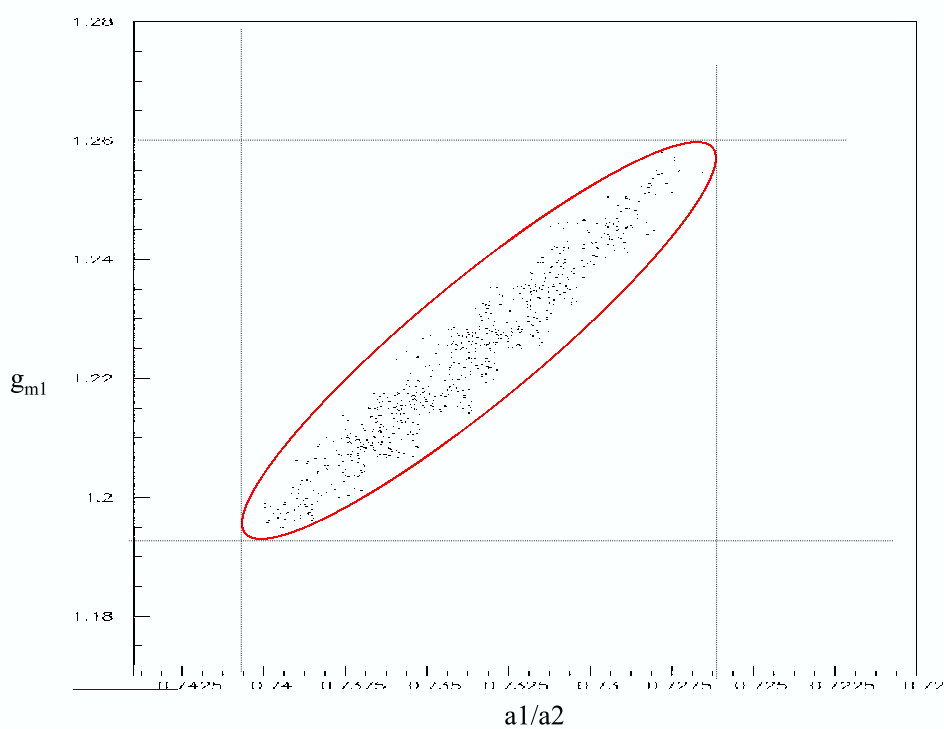


Figure 8.1: A scatterplot representing the 2-D cross-section (\tilde{g}_{M1} vs. $\frac{a1}{a2}$) of the 3-D "error ellipsoid" defined by parameter value combinations that produce log likelihoods within 0.5 of the maximum. An ellipse representing the approximate contour is drawn in for clarity.

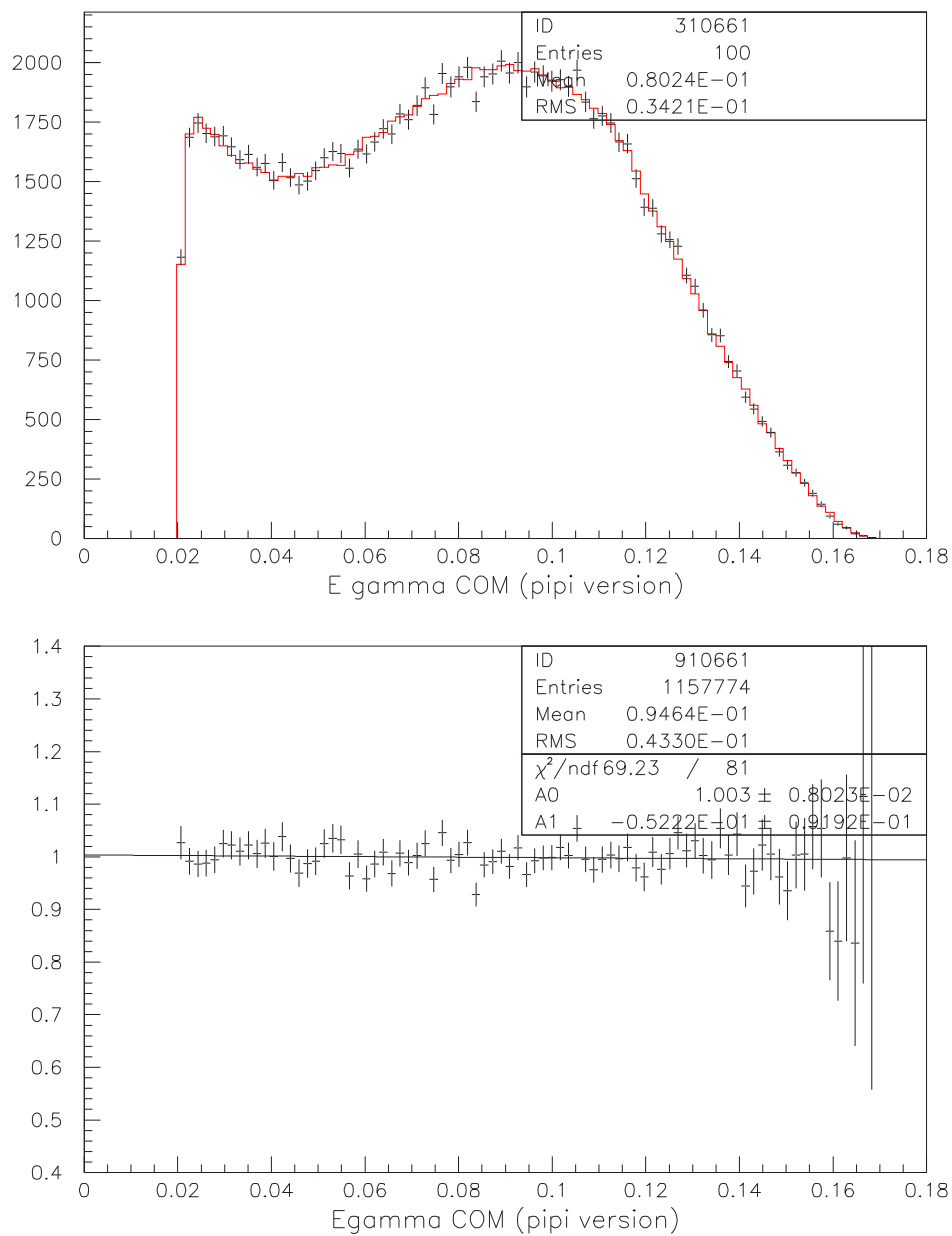


Figure 8.2: Distribution of phase space variable ω (data, Monte Carlo).
Upper plot: $N_{events}/(1.8 \text{ MeV})$ vs. ω (GeV). Crosses represent data.
Lower plot: Data/MC ratio vs. ω (GeV).

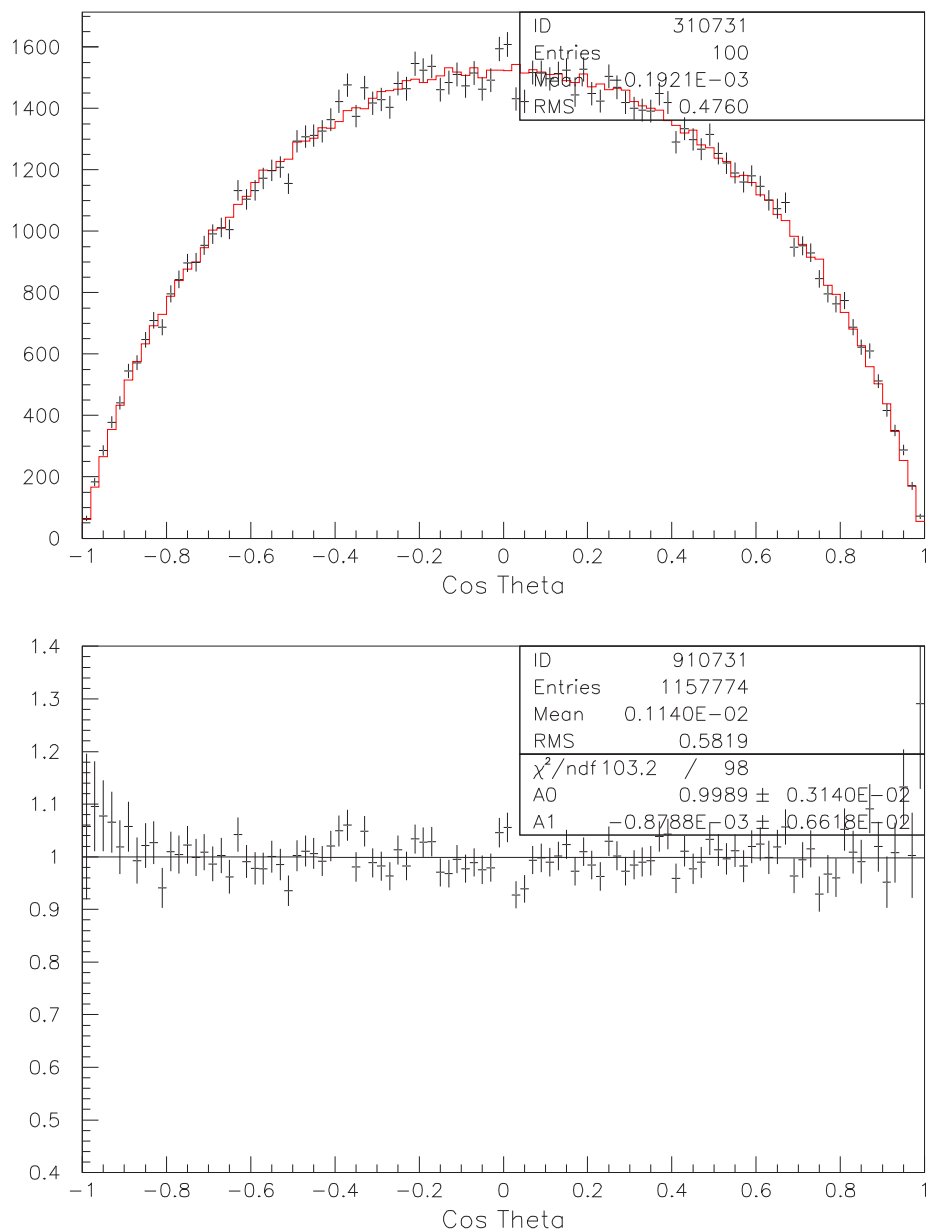


Figure 8.3: Distribution of phase space variable $\cos\theta$ (data, Monte Carlo).
Upper plot: $N_{events}/0.02$ vs. $\cos\theta$. Crosses represent data.
Lower plot: Data/MC ratio vs. $\cos\theta$.

denotes the 90% confidence level (CL) boundary, such that a given measurement of G_{E1} has a 90% probability of being above the line.

Since the best-fit regime in this analysis produced a measurement of $G_{E1} = 0.0$, the 90% CL upper limit was determined as the X-intercept of the best-fit line at 0.11.

8.3 Verification of the Likelihood Fit Procedure

Once the likelihood fitting code was written, extensive testing was performed to verify that it was implemented correctly. The initial study done to increase confidence in the measuring procedure used 18 individual, data-sized Monte Carlos that were generated over a fairly broad range parameter values (the generation values are summarized in table 8.2).

The absolute difference between the generated and measured values of the three parameters was plotted for each file. In order to determine the approximate statistical significance of the agreement, each data point is plotted relative to the grid-determined error³ on the nominal (i.e. actual data) best-fit. In other words, a given fit parameter value “X” ($X \equiv \{\tilde{g}_{M1}, \frac{a_1}{a_2}, G_{E1}\}$) is plotted as

$$\frac{|X_{generated} - X_{measured}|}{\sigma_{X(data)}} \quad (8.1)$$

Therefore, roughly speaking,⁴ 68% of the plotted plots should have a ratio ≤ 1.0 and 98% should have a ratio ≤ 2.0 . So, we therefore expected ~ 12 of the 18 datapoints to be fitted within 1σ of their generated values and $\sim 17-18$ of the

³see table 8.1

⁴Note that this was only an approximation, since, in reality, it was expected that different regions of phase space could be slightly more or slightly less sensitive to a given parameter. Therefore, the exact error bars associated with a given point on the plot might be slightly larger or slightly smaller than the error calculated for the data. Nevertheless, this discrepancy was believed to be irrelevant for the purposes of this study.

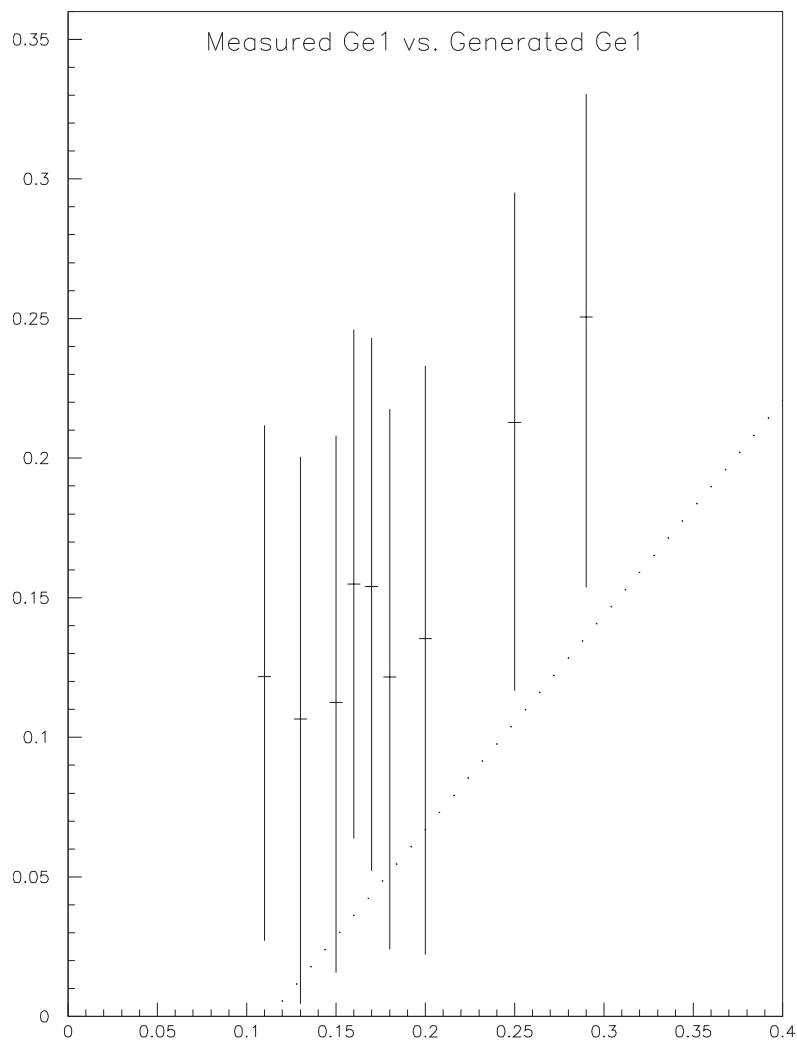


Figure 8.4: Feldman and Cousins upper limit plot of Measured G_{E1} vs Generated G_{E1} at 90% CL . Error bars plotted on individual points are 1.28σ in width.

Test MC ID	Generated \tilde{g}_{M1}	Generated $\frac{a_1}{a_2}$	Generated G_{E1}
1	1.00	-0.700	0.00
2	1.00	-0.740	0.00
3	1.00	-0.780	0.00
4	1.20	-0.700	0.00
5	1.20	-0.740	0.00
6	1.20	-0.780	0.00
7	1.45	-0.700	0.00
8	1.45	-0.740	0.00
9	1.45	-0.780	0.00
10	1.00	-0.700	0.07
11	1.00	-0.740	0.07
12	1.00	-0.780	0.07
13	1.20	-0.700	0.07
14	1.20	-0.740	0.07
15	1.20	-0.780	0.07
16	1.45	-0.700	0.07
17	1.45	-0.740	0.07
18	1.45	-0.780	0.07

Table 8.2: Generated parameter values for the 18 trial Monte Carlo files used in the initial likelihood fitter verification study.

The absolute difference between the generated and measured values of these test Monte Carlos are plotted in figures 8.5 through 8.7.

points to be fitted within 2σ . As one can see from figures 8.5 to 8.7, that was, in fact, what we observed.

To bolster the previous study and to obtain a much more quantitative measurement of the accuracy of the fit procedure, fits were made on sets of 25 to 50 data-sized Monte Carlo files. Individual files within a given set were all generated at the same parameter values, and each file in the set was fit using the same fit program as the data. The fit value average ($\langle X \rangle$), standard deviation (σ_X), and standard deviation on the average ($\sigma_{\langle X \rangle} = \sigma_X/N$) over the N samples ($N = 25$ or 50) were then calculated for each set. The results are summarized in tables 8.3 and 8.4. The accuracy of the fitting regime was then determined via the absolute difference (ΔX) between the input and measured values, given by

$$\Delta X = |X_{gen} - X_{measured}| \quad (8.2)$$

The absolute difference was then divided by the error on the measured average ($\sigma_{\langle X \rangle}$) to give statistical significance to the fit accuracy. The final results of the study (summarized in table 8.4) demonstrated that the fitter worked as designed, generally reproducing the input values, within 1 to 2 standard deviations of the average. However, since the results were generally worst-case just outside the 1σ limit of expected statistical fluctuations, the maximum deviations were assigned as systematic errors and were added to the list of errors in table 9.12 in the next chapter.

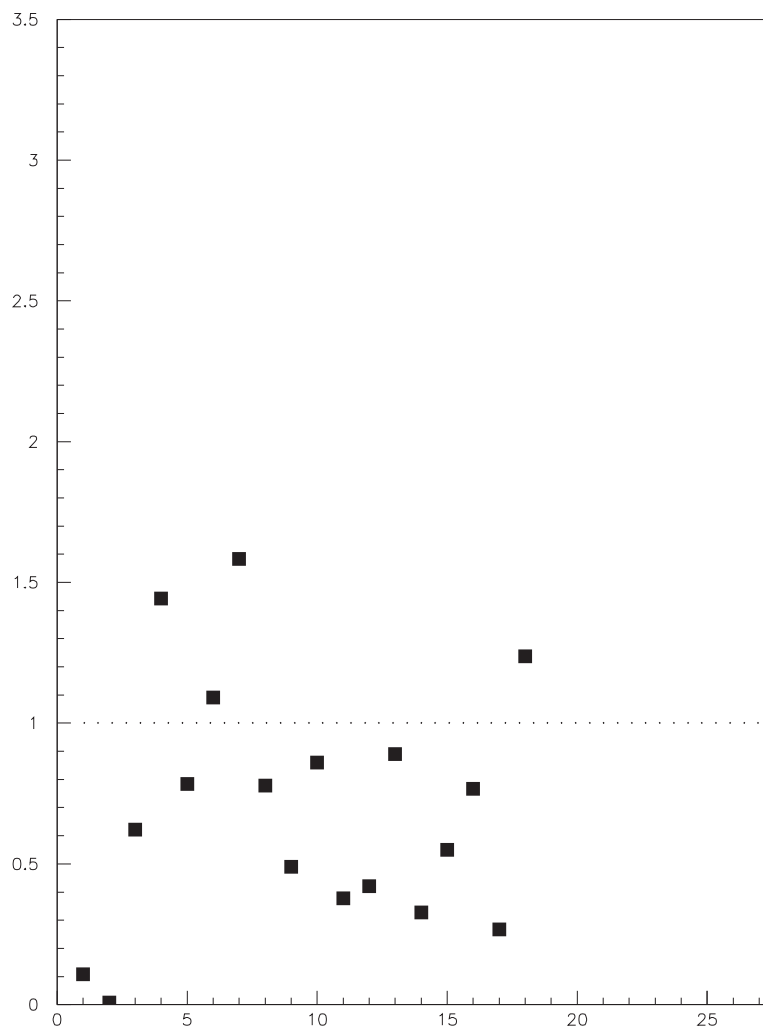


Figure 8.5: Deviation (in σ) between input and measured values of \tilde{g}_{M1} for 18 data-sized trial Monte Carlos. Plot is Sigma Deviation vs. Monte Carlo file number (1-18).

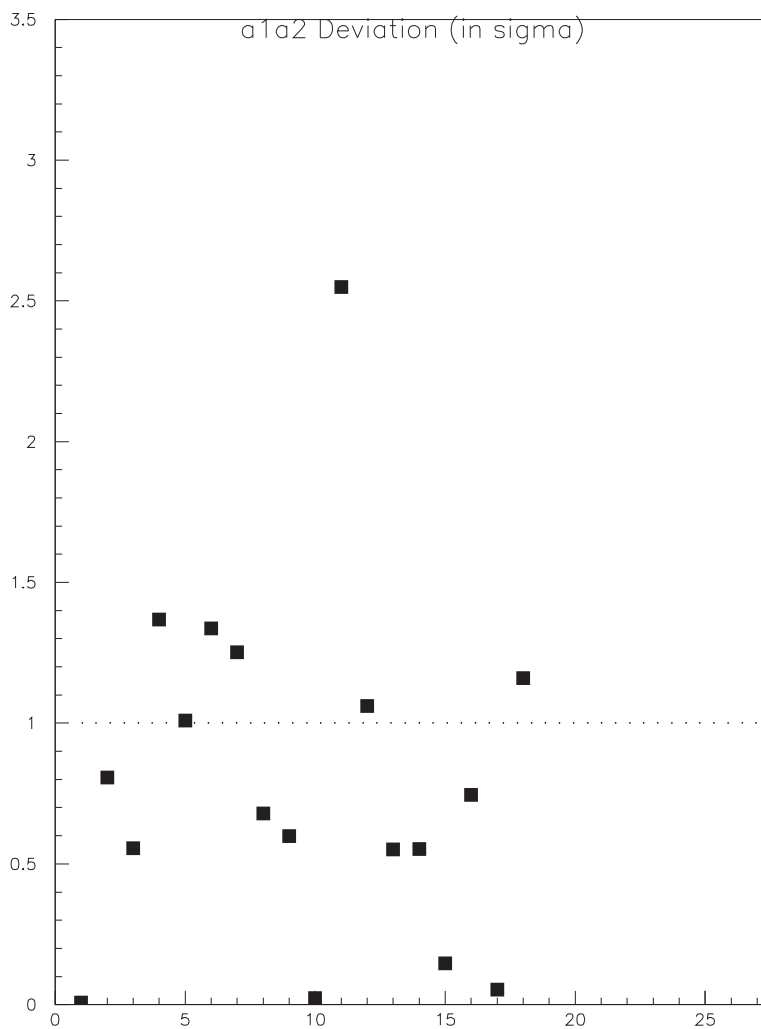


Figure 8.6: Deviation (in σ) between input and measured values of $\frac{a_1}{a_2}$ for 18 data-sized trial Monte Carlos. Plot is Sigma Deviation vs. Monte Carlo file number (1-18).

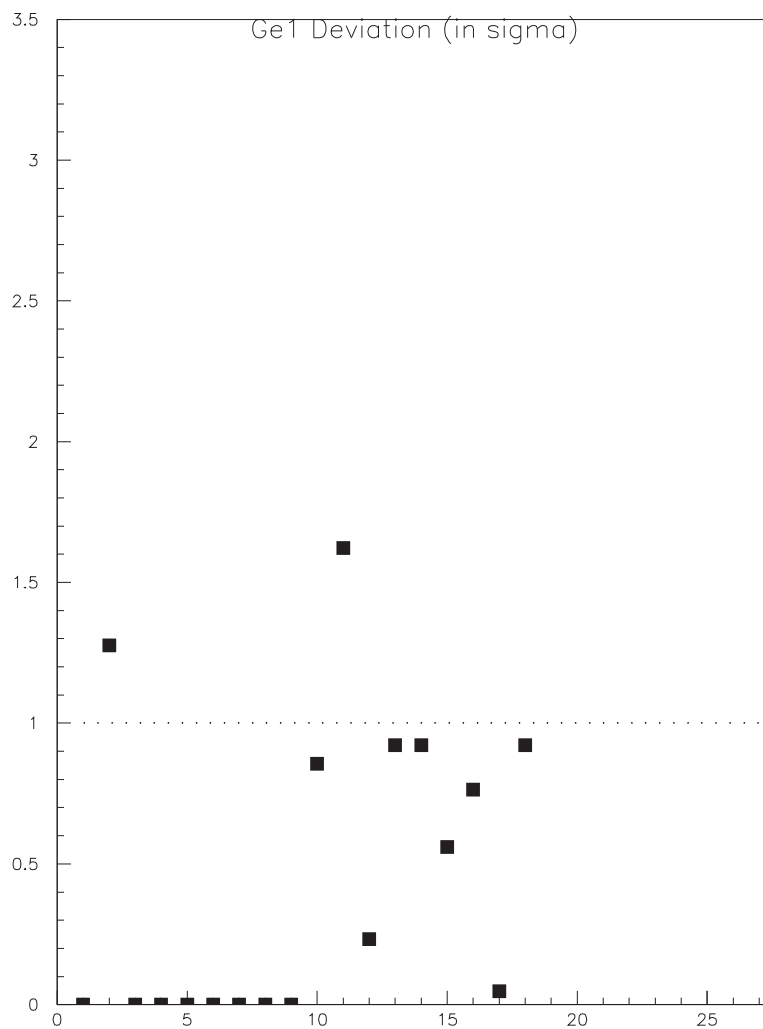


Figure 8.7: Deviation (in σ) between input and measured values of G_{E1} for 18 data-sized trial Monte Carlos. Plot is Sigma Deviation vs. Monte Carlo file number (1-18).

Set	N_{files}	Generated Values			Measured Values (Ave)			Error on the Average		
		\tilde{g}_{M1}	$\frac{a_1}{a_2}$	G_{E1}	\tilde{g}_{M1}	$\frac{a_1}{a_2}$	G_{E1}	$\sigma_{\langle \tilde{g}_{M1} \rangle}$	$\sigma_{\langle \frac{a_1}{a_2} \rangle}$	$\sigma_{\langle G_{E1} \rangle}$
set 1	50	1.20	-0.737	0.04	1.207	-0.7314	0.055	0.005	0.0012	0.009
set 2	25	1.05	-0.775	0.07	1.056	-0.7728	0.053	0.005	0.0016	0.009
set 3	25	1.20	-0.733	0.00	1.216	-0.7353	0.024	0.010	0.0023	0.008
set 4	25	1.08	-0.755	0.01	1.071	-0.7565	0.023	0.007	0.0018	0.008

Table 8.3: Comparison of input & generated values at 4 different selections of input values.

Sample Set	$\Delta X \equiv \langle X \rangle - X_{gen} $			$\sigma_{\langle X \rangle}$ Deviation		
	$ \Delta_{\tilde{g}_{M1}} $	$ \Delta_{\frac{a_1}{a_2}} $	$ \Delta_{G_{E1}} $	\tilde{g}_{M1}	$\frac{a_1}{a_2}$	G_{E1}
Set 1	0.007	0.0056	0.015	1.40	4.67	1.67
Set 2	0.006	0.0022	0.017	1.20	1.38	1.89
Set 3	0.014	0.0023	0.024	1.40	1.00	3.00
Set 4	0.009	0.0015	0.013	1.29	0.83	1.63
Max Shift	0.014	0.0056	0.024	-	-	-

Table 8.4: Sigma Deviation of Monte Carlo sample sets described in table 8.3.

Chapter 9

Systematics Studies

9.1 Systematic Uncertainty of the Likelihood Fit Program due to Different Baseline Monte Carlos

One of the most obvious systematic errors to determine was the extent to which the reweighting of a single, “baseline” Monte Carlo file biased the final answer. To study this effect, three Monte Carlo files were generated with the same input parameter values ($\tilde{g}_{M1} = 1.20$, $\frac{a_1}{a_2} = -0.737$, $G_{E1} = 0.04$) and the same number of events (50 times the data) as the nominal baseline file— in other words, the files differ from the nominal only by a random seed. The best-fit of the data sample was then recomputed using each of the three new baseline files in order to estimate the statistical fluctuations associated with the generation of a Monte Carlo with a given set of input parameter values. The results are summarized in table 9.1.

Making the assumption that the four jobs are relatively representative of the distribution of values, the standard deviation of the four fit results was taken as the statistical uncertainty on the generation of the nominal $50N_{data}$ event Monte Carlo. The variations, average, and standard deviations of the results are shown in table 9.1.

Baseline Monte Carlo	\tilde{g}_{M1}	$\frac{a_1}{a_2}$	G_{E1}
original (nominal) MC	1.22863603	-0.73295301	0.0000
new MC #1	1.23510277	-0.73167145	0.0000
new MC #2	1.22731066	-0.73350447	0.0000
new MC #3	1.22827411	-0.73339522	0.0035
ave	1.22983089	-0.73288104	0.0009
std dev	0.0030820	0.000728	0.0015

Table 9.1: Likelihood fit results for data fit by four Monte Carlo files generated at “nominal” input values that differ only by a random seed.

Generated Values				Δ from nominal fit result		
Baseline MC	\tilde{g}_{M1}	$\frac{a_1}{a_2}$	G_{E1}	$ \Delta_{\tilde{g}_{M1}} $	$ \Delta_{\frac{a_1}{a_2}} $	$ \Delta_{G_{E1}} $
(nominal)	1.20	-0.737	0.04	0.0000	0.0000	0.00
Baseline A	1.35	-0.733	0.04	0.0043	0.0008	0.00
Baseline B	1.05	-0.733	0.04	0.0093	0.0021	0.00
Baseline C	1.20	-0.710	0.04	0.0035	0.0010	0.00
Baseline D	1.20	-0.770	0.04	0.0073	0.0011	0.00
Baseline E	1.20	-0.733	0.12	0.0078	0.0012	0.00
Baseline F	1.05	-0.775	0.07	0.0006	0.0001	0.007
Baseline G	1.23	-0.733	0.30	0.0013	0.0009	0.013
Max Dev from nominal	-	-	-	0.0093	0.0021	0.013
Syst Error assigned	-	-	-	0.0093	0.0021	0.013

Table 9.2: Shift in fit parameter values due to the change in the baseline Monte Carlo used in the likelihood fit.

The data was then re-fit using seven other $50N_{data}$ event Monte Carlos with varying parameter values. The generated and measured values of each of the seven files is summarized in table 9.2. Since the maximum deviation in the fit parameters in table 9.2 was slightly greater than the corresponding statistical errors from table 9.1, we assigned the deviations as the systematic error associated with the choice of a particular baseline Monte Carlo file.

9.2 Systematic Error in the Kaon Momentum Slope

One of the most critical elements of this analysis was the ability of the Monte Carlo to simulate the kaon momentum spectrum. Figure 9.1 shows the agreement between data and Monte Carlo in this variable. A common method of kaon momentum correction is to directly reweight the events to make the data/MC slope flat and then base all other measurements relative to that correction. However, in this particular analysis, it was not possible to make use of this technique, since the phase space parameter that we wished to fit (the kaon COM photon energy, ω) was correlated with the kaon momentum.

Instead, in order to obtain the best possible agreement, the kaon momentum spectrum determined from the $K_L \rightarrow \pi^+\pi^-$ decay was input into the $K_L \rightarrow \pi^+\pi^-\gamma$ Monte Carlo generator. Thus the Monte Carlo was obtained independently from the $K_L \rightarrow \pi^+\pi^-\gamma$ data and therefore did not bias the determination of the final fit parameters from the $K_L \rightarrow \pi^+\pi^-\gamma$ mode. The slope (M) and y-intercept (b) of the kaon momentum data/MC ratio in Figure 9.1 are given by $M = (-1.85 \pm 1.39) \times 10^{-4}$ and $b = 1.010 \pm 0.009$, respectively.

Although the data/Monte Carlo ratio appeared to agree fairly well, it was not precisely the perfectly flat spectrum indicative of perfect data, Monte Carlo agreement. It was therefore necessary to determine the effect that this deviation from flatness had upon the final fit parameter values. To study this, the “baseline” Monte Carlo used in the likelihood fit had its kaon momentum spectrum reweighted by M and b, and the data was then refit using this reweighted Monte Carlo. The results are summarized in table 9.3. The systematic error assigned is the maximum deviation in each fit parameter from its nominal value ($\Delta_{\tilde{g}_{M1}} = 0.003$, $\Delta_{\frac{a_1}{a_2}} = 0.0004$, and $\Delta_{G_{E1}} = 0.005$).

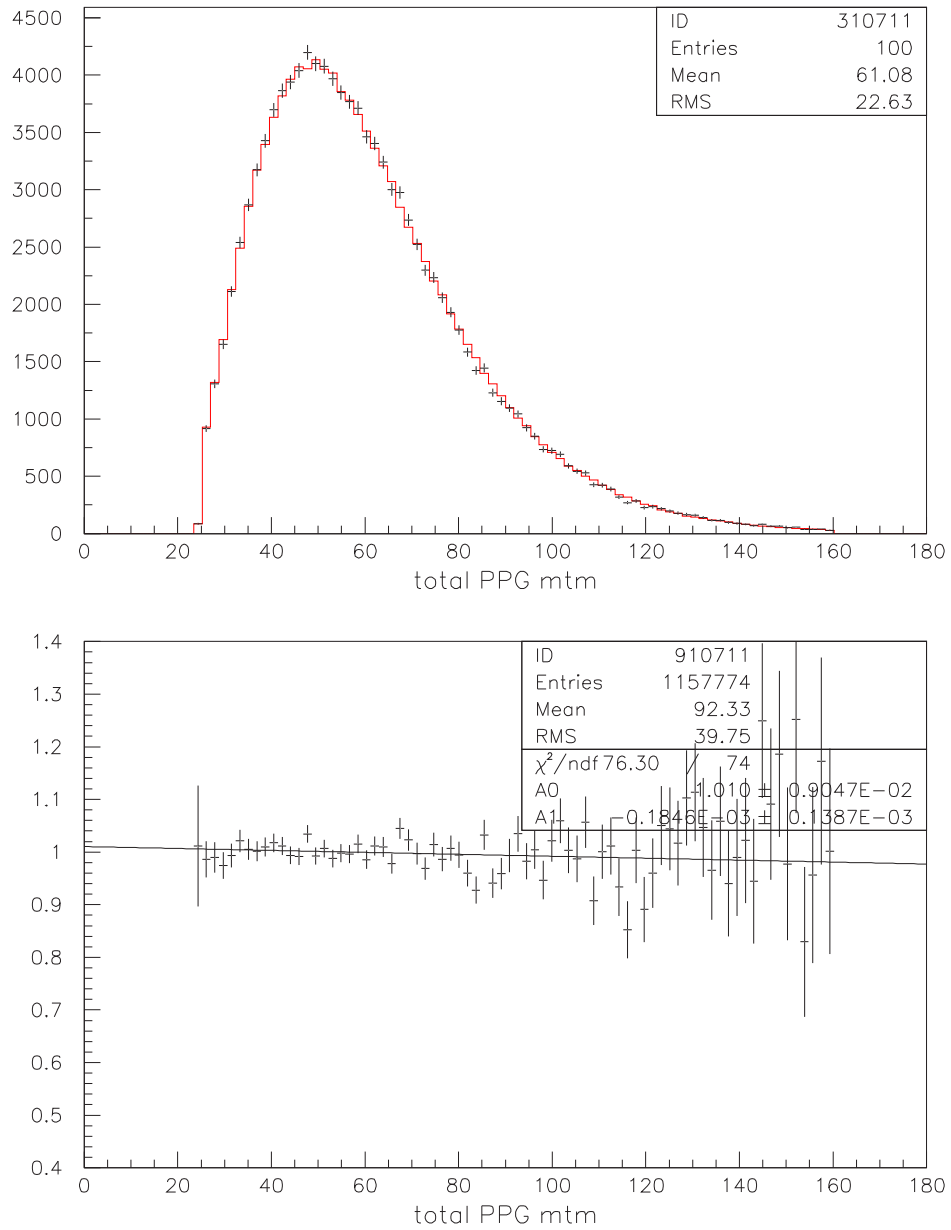


Figure 9.1: $\pi^+\pi^-\gamma$ combined momentum distribution (data, Monte Carlo).
Upper plot: $N_{\text{events}}/(1.8 \text{ GeV})$ vs. $P_{\pi^+\pi^-\gamma}$ (GeV). Crosses represent data.
Lower plot: Data/MC ratio vs. $P_{\pi^+\pi^-\gamma}$ (GeV).

Reweighting	$\Delta_{\tilde{g}_{M1}}$	$\Delta_{\frac{a_1}{a_2}}$	$\Delta_{G_{E1}}$
M, b	+0.0010	-0.00012	-0.002
M + σ_M , b + σ_b	-0.0009	+0.00011	+0.002
M - σ_M , b + σ_b	+0.0031	-0.00039	-0.005
M + σ_M , b - σ_b	-0.0009	+0.00011	+0.002
M - σ_M , b - σ_b	+0.0031	-0.00040	-0.005
Max Deviation from nominal	0.003	0.0004	0.005
Systematic Error Assigned	0.003	0.0004	0.005

Table 9.3: Systematic error on the kaon momentum slope

9.3 Systematic Error Due to Choice of Physics Analysis Cuts

One important consideration was to account for the possibility that a particular choice of analysis cuts in some way biases the final result by over-emphasizing (or under-emphasizing) a particular region of phase space or by somehow disturbing agreement of data and Monte Carlo. The size of this effect on a given parameter value “X” ($X = \{\tilde{g}_{M1}, \frac{a_1}{a_2}, G_{E1}\}$) was determined by varying the analysis cuts “in the vicinity” of the nominal cut choices and then recalculating the data best-fit results and error bars. Although the definition of “vicinity” was somewhat unique to each analysis cut variable, the regions of variation were generally constrained by crunch cuts, detector fiducial considerations, and the requirement that a sample produced by a tightened cut retain at least about a third of the events of the nominal data sample.

Once the measurements of the cut-modified samples was complete, the fit parameter shift (S) in the final result (where $S \equiv |X_{cut-varied} - X_{nominal}|$) was computed. If the parameter shift was larger than the expected statistical fluctuation (σ_S), then that shift was interpreted as a non-zero systematic error.

Note that this was a non-trivial process, since running the complete analysis

and error bar determination on a single choice of cuts required 1 to 4 weeks of CPU to complete.

One subtlety of this analysis was that the nominal and cut-varied samples were highly correlated. Therefore, the statistical error on the shift was smaller than the statistical error on the cut-varied sample itself. Specifically, the error on the shift was given by¹

$$\sigma_S = \sqrt{|\sigma_{cut-varied}^2 - \sigma_{nominal}^2|} \quad (9.1)$$

The final size of the systematic error (ΔS) was calculated using a dual case scenario. In Case I, the shift was within statistical fluctuations (i.e. $S \leq \sigma_S$), and hence no systematic error was assigned (i.e. $\Delta S = 0$). In Case II, the shift was outside the expected range of fluctuations ($S > \sigma_S$) and therefore was assigned an error ΔS such that the range $(-\Delta S, \Delta S)$ includes 68.3% of the area of a Gaussian with mean S and width σ_S :

$$\frac{1}{\sigma_S \sqrt{2\pi}} \int_{-\Delta S}^{\Delta S} dx \exp \left[\frac{-(x - S)^2}{2\sigma_S^2} \right] = 0.683 \quad (9.2)$$

Plots of the shift in parameter values vs. analysis cut choice are shown in figures (9.2) through (9.11). Error bars on individual data points represent the statistical error on the shift (σ_S). Horizontal dotted lines representing the size of the statistical error on the fit parameters from the nominal data fit (see table 8.1) are also included on each plot for scale.

Note that the data points at the nominal cut choice values have a small σ_S error bar assigned, even though the “nominal” and “cutvaried” samples for these instances are identical. This is because each data point includes an error bar re-

¹see Appendix B for a derivation of this result

flecting the uncertainty associated with the finite grid size used in the primary statistical error on the measurement. The assigned systematic errors are summarized in table 9.6.

It is important to note, however, that two analysis cut variables, the kaon momentum and vertex Z position, had error bars assigned in a manner that deviated slightly from the prescription previously described. These two particular distributions were highly correlated to both one another and to the distribution of the phase space itself. Therefore, any observed shift in a measured parameter could be due to a true systematic effect in the measurement technique or simply to the fact that the tightened cuts are confining the measured events to a limited region of phase space.

Recall, however, that the quality of data, Monte Carlo agreement in the kaon momentum spectrum (and hence essentially vertex Z as well) was already directly assessed in section 9.2, and a separate systematic error for this quantity was computed. Since the systematic calculated from that study was significantly smaller than the one derived from the variation of the kaon momentum cut, it was therefore concluded that the limited phase space was, in fact, the dominant contributor to the kaon momentum and vertex Z shifts observed in figures 9.7 and 9.9.

Based on this, it was concluded that blindly applying the previously described " ΔS prescription" to the kaon momentum and vertex Z plots would result in the assignation of unrealistically large systematic errors. As a result, the decision was made to shrink the relevant cut range "vicinity" for these two variables. For reference, a list of the original kaon momentum and vertex Z cut variations (and the sizes of the corresponding event samples) are included as table 9.4.

In practice, "shrinking the vicinity" meant that the ΔS prescription was only

Variable	Cut Selection				
	1	2	3	4	5
P_{Kaon} cut (GeV/c)	20.0	25.0	35.0	55.0	75.0
N_{events}	113051	112140	102297	60007	25682
$N_{events}/N_{nominal}$	1.01	1.0	0.91	0.53	0.23
Vertex Z cut (m)	110.0	120.0	130.0	140.0	N/A
N_{events}	118269	112140	79482	46128	N/A
$N_{events}/N_{nominal}$	1.05	1.0	0.71	0.41	N/A

Table 9.4: Number of events for each kaon momentum and vertex Z cut variation.

Analysis Variable	ΔS (Standard Procedure)			ΔS (Modified Procedure)		
	$\sigma_{\tilde{g}_{M1}}$	$\sigma_{\frac{a_1}{a_2}}$	$\sigma_{G_{E1}}$	$\sigma_{\tilde{g}_{M1}}$	$\sigma_{\frac{a_1}{a_2}}$	$\sigma_{G_{E1}}$
Kaon Momentum	0.082	0.016	0.0	0.029	0.0	0.0
Vertex Z	0.089	0.016	0.0	0.034	0.0056	0.0

Table 9.5: Effects of modified ΔS procedure on P_{kaon} and vertex Z

applied to the first 3 points on each of the two plots² (corresponding to minimum kaon momentum of 35 GeV and a minimum vertex Z of 130 m). The differences in systematic errors assigned in the standard and modified procedures are summarized in table 9.5 , and the final assigned systematic errors are included in table 9.6.

9.4 Background Effects

Because the $K_L \rightarrow \pi^+\pi^-\gamma$ branching ratio is relatively small ($\sim 5 \times 10^{-5}$), accurately assessing background effects from direct generation of all possible sources was difficult³. It was decided that the most practical way to measure these effects was to use the distribution of the “wings” of the kaon mass peak. The left wing region was defined as $0.47000 < M_{\pi^+\pi^-\gamma} < 0.48967$ GeV and the right wing region was defined as $0.50567 < M_{\pi^+\pi^-\gamma} < 0.55000$ GeV.

²For perspective, keep in mind that the fiducial decay volume ends at $Z \approx 160$ m.

³For example, it was difficult to accurately simulate events that were scattered off the regenerator into the vacuum beam.

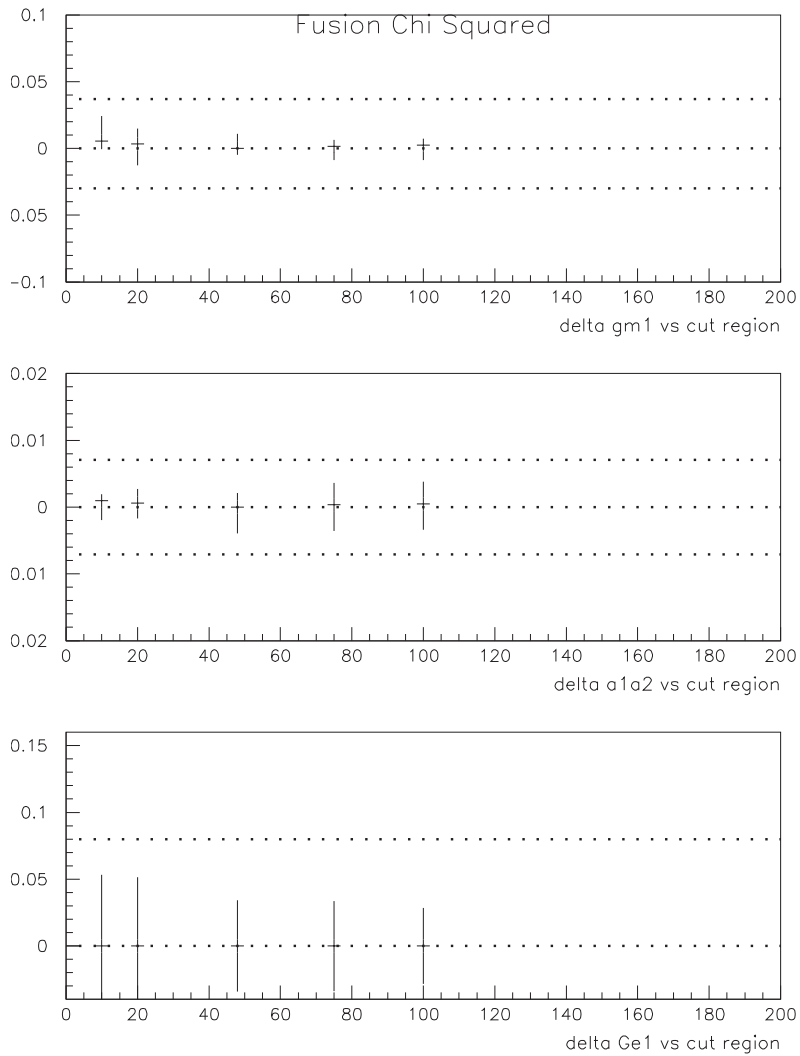


Figure 9.2: Fit parameter shift S vs. Fusion χ^2 Cut Selection
 (from top to bottom): \tilde{g}_{M1} , $\frac{a_1}{a_2}$, G_{E1}

Dotted lines are nominal data stat errors (table 8.1), included for scale.

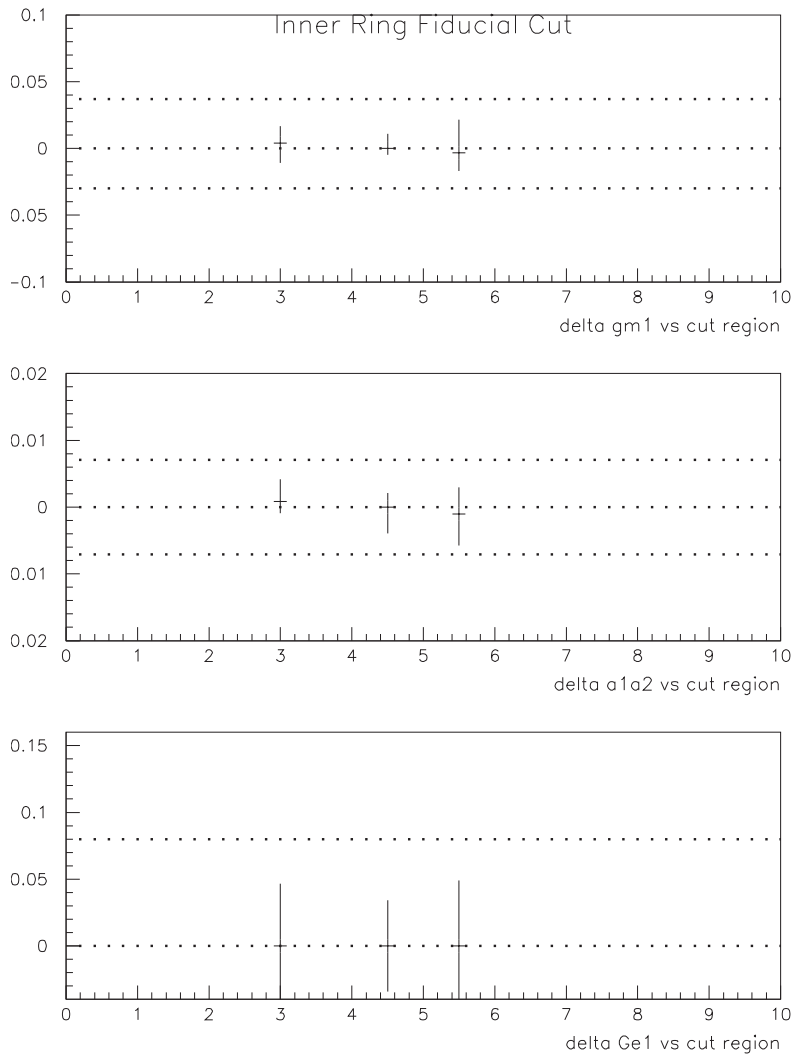


Figure 9.3: Fit parameter shift S vs. CsI Inner Fiducial Cut
 (from top to bottom): \tilde{g}_{M1} , $\frac{a_1}{a_2}$, G_{E1}
 Dotted lines are nominal data stat errors (table 8.1), included for scale.

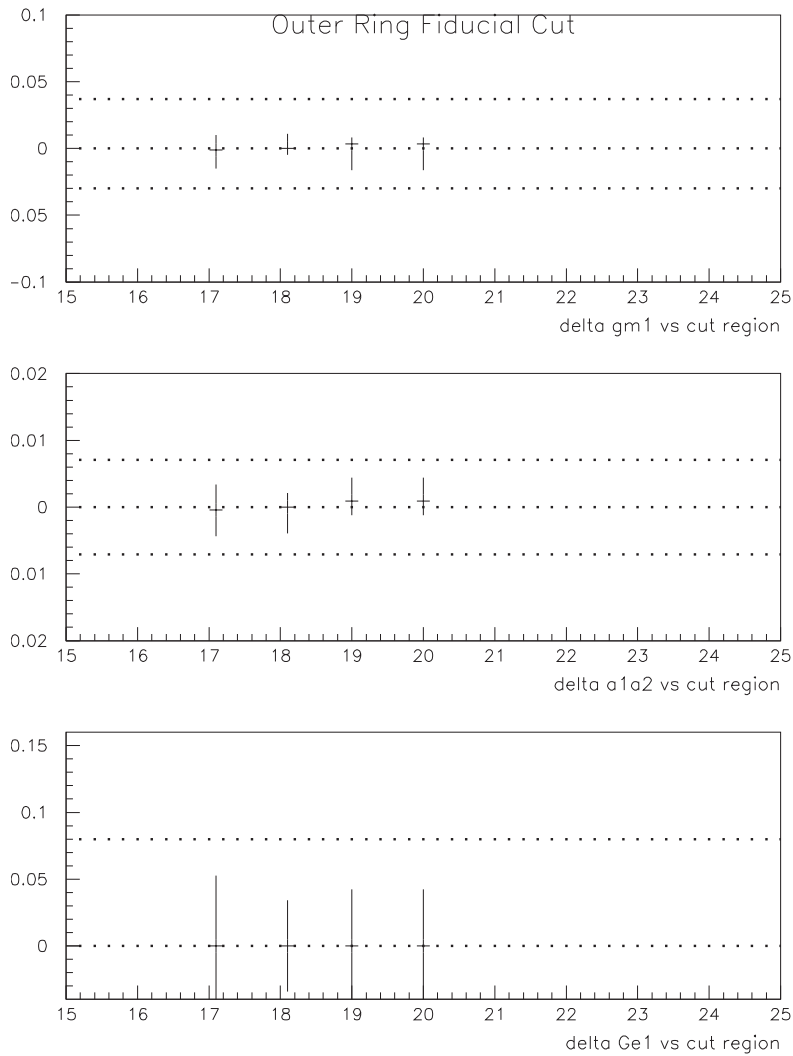


Figure 9.4: Fit parameter shift S vs. CsI Outer Fiducial Cut
(from top to bottom): \tilde{g}_{M1} , $\frac{a_1}{a_2}$, G_{E1}

Dotted lines are nominal data stat errors (table 8.1), included for scale.

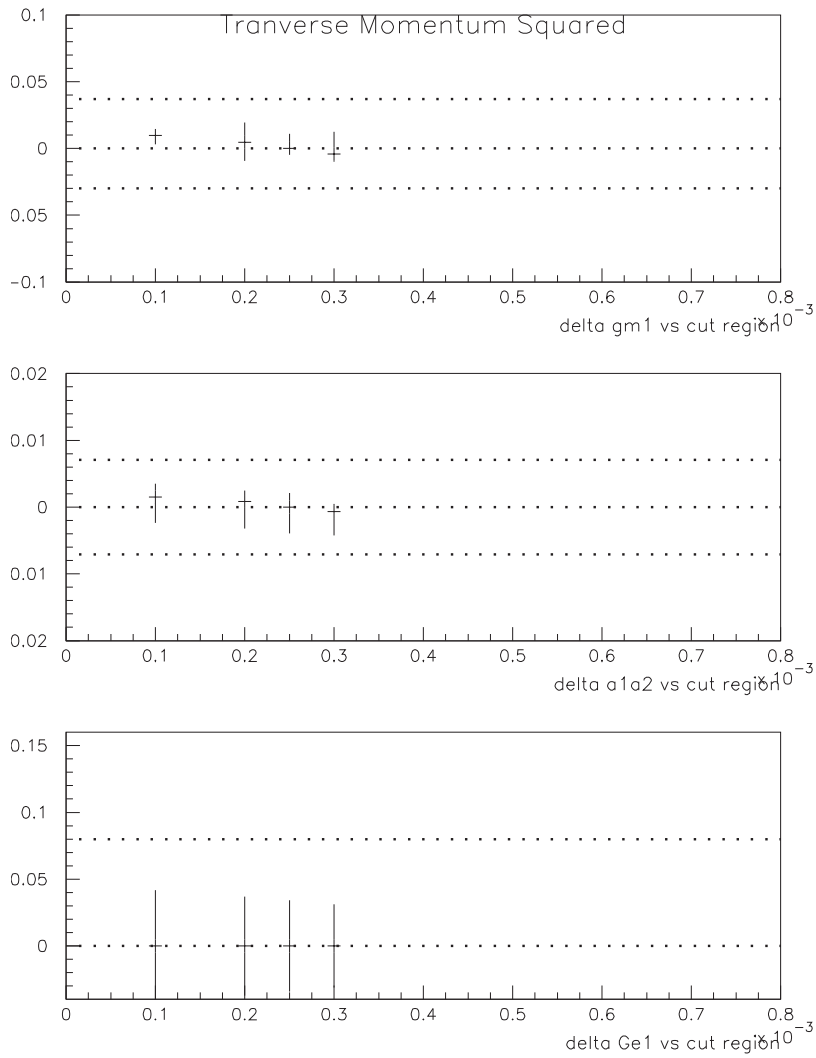


Figure 9.5: Fit parameter shift S vs. $P_{transverse}^2$ Cut $(GeV/c)^2$
 (from top to bottom): \tilde{g}_{M1} , $\frac{a_1}{a_2}$, G_{E1}

Dotted lines are nominal data stat errors (table 8.1), included for scale.

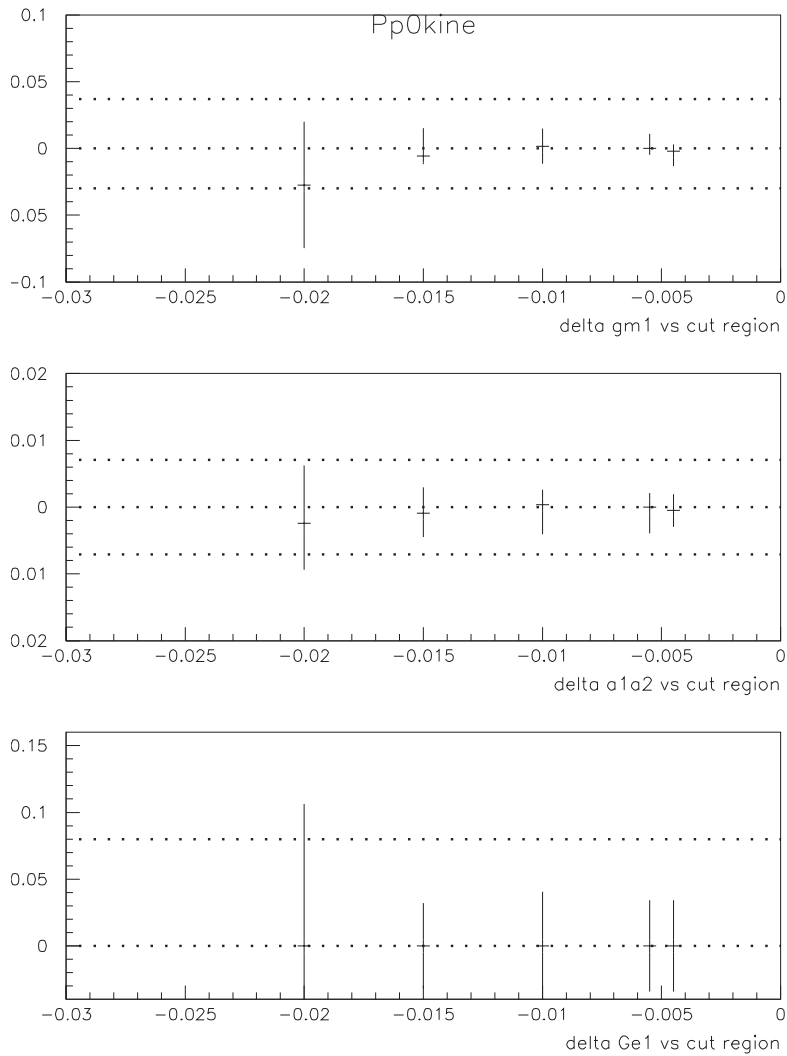


Figure 9.6: Fit parameter shift S vs. PP0KINE Cut $(GeV/c)^2$
 (from top to bottom): \tilde{g}_{M1} , $\frac{a_1}{a_2}$, G_{E1}
 Dotted lines are nominal data stat errors (table 8.1), included for scale.

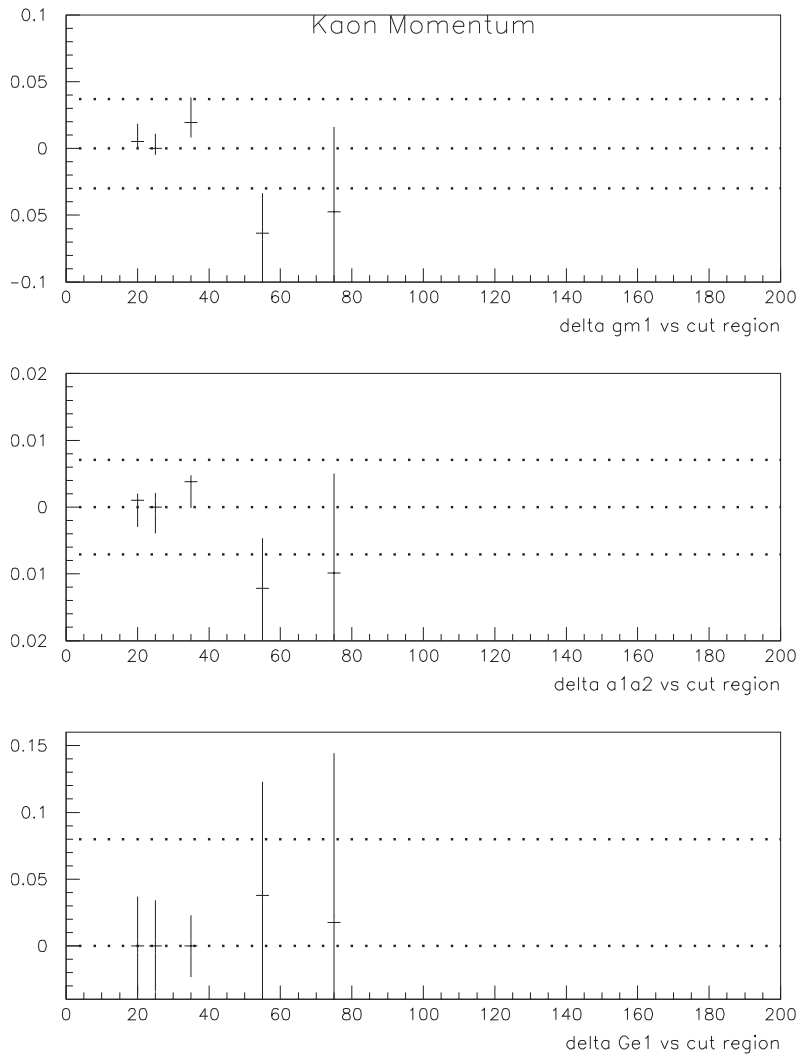


Figure 9.7: Fit parameter shift S vs. Kaon Momentum Cut (GeV)

(from top to bottom): \tilde{g}_{M1} , $\frac{a_1}{a_2}$, G_{E1}

Dotted lines are nominal data stat errors (table 8.1), included for scale.

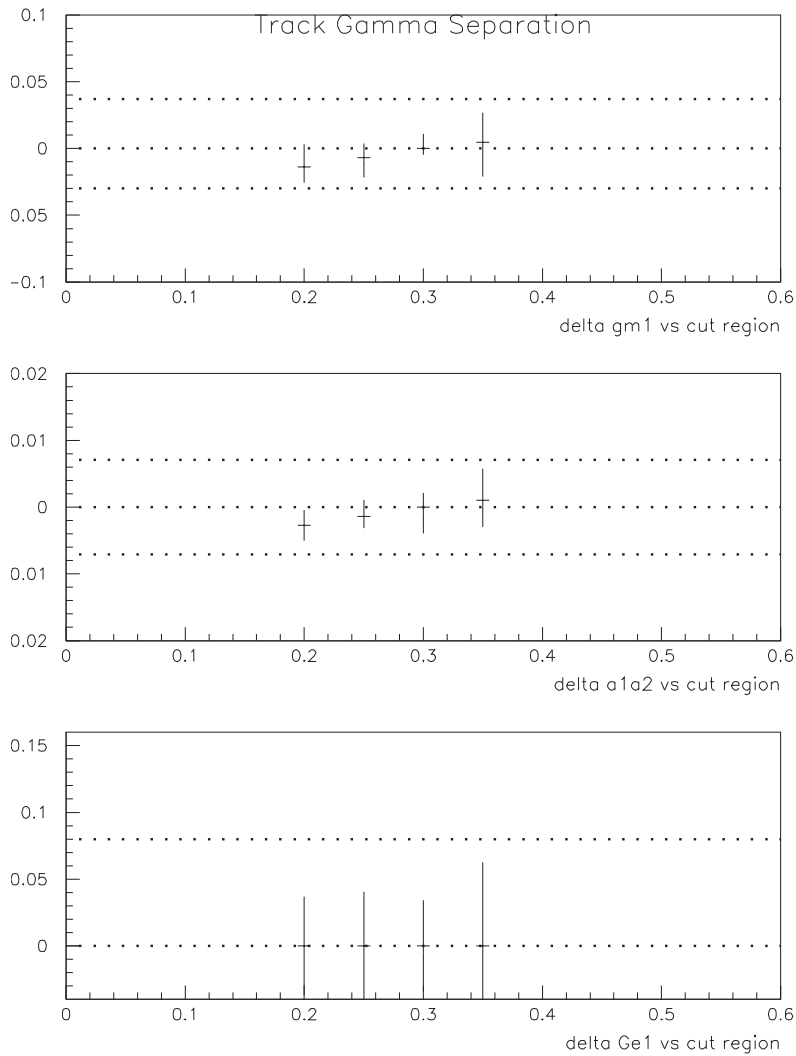


Figure 9.8: Fit parameter shift S vs. Track-Photon Separation Cut (meters)
 (from top to bottom): \tilde{g}_{M1} , $\frac{a_1}{a_2}$, G_{E1}
 Dotted lines are nominal data stat errors (table 8.1), included for scale.

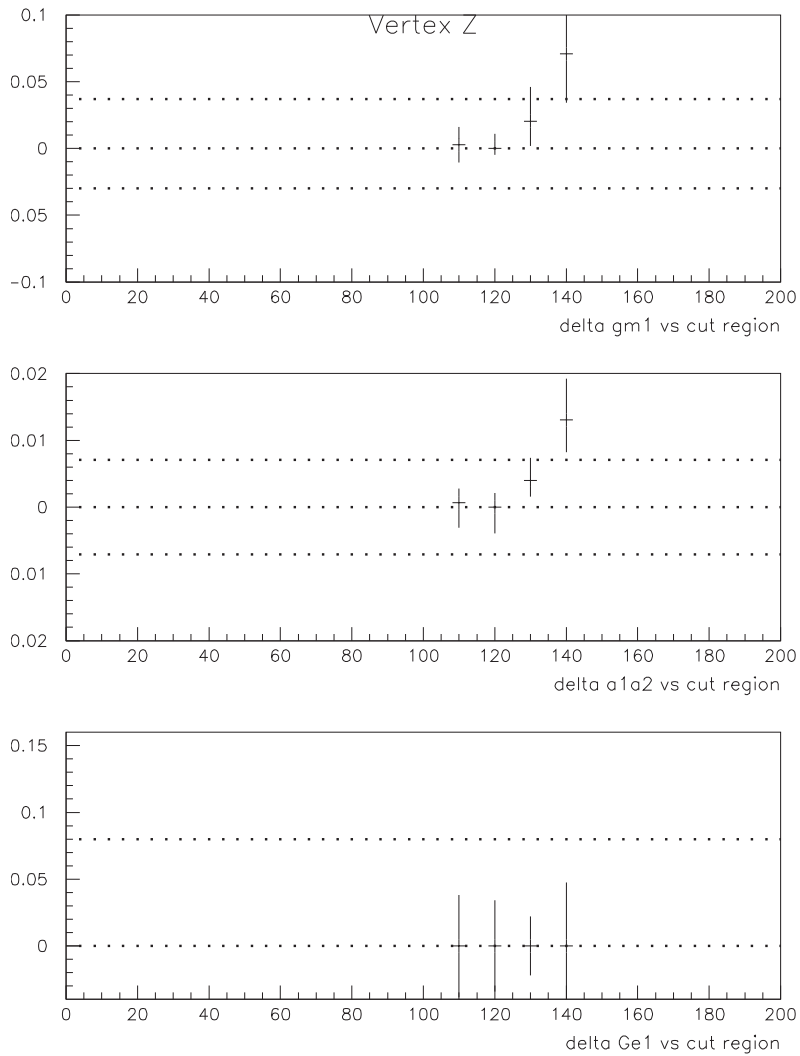


Figure 9.9: Fit parameter shift S vs. Vertex Z Cut (meters)
 (from top to bottom): \tilde{g}_{M1} , $\frac{a_1}{a_2}$, G_{E1}
 Dotted lines are nominal data stat errors (table 8.1), included for scale.

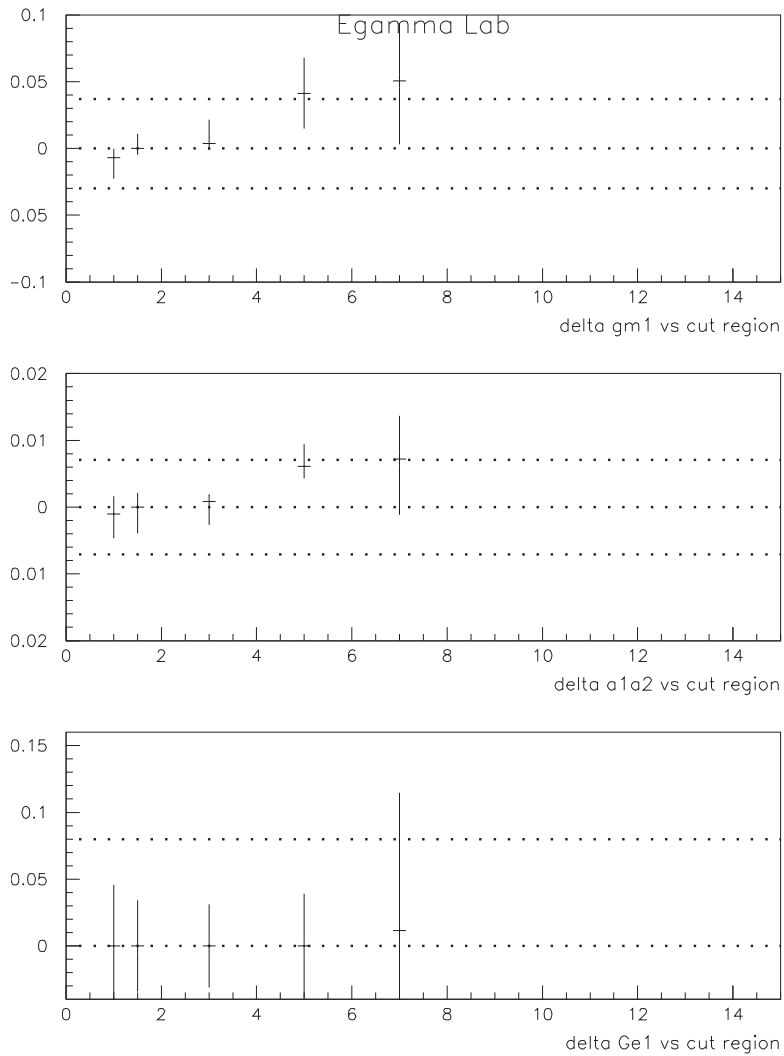


Figure 9.10: Fit parameter shift S vs. Lab Photon Energy Cut (GeV)
 (from top to bottom): \tilde{g}_{M1} , $\frac{a_1}{a_2}$, G_{E1}
 Dotted lines are nominal data stat errors (table 8.1), included for scale.

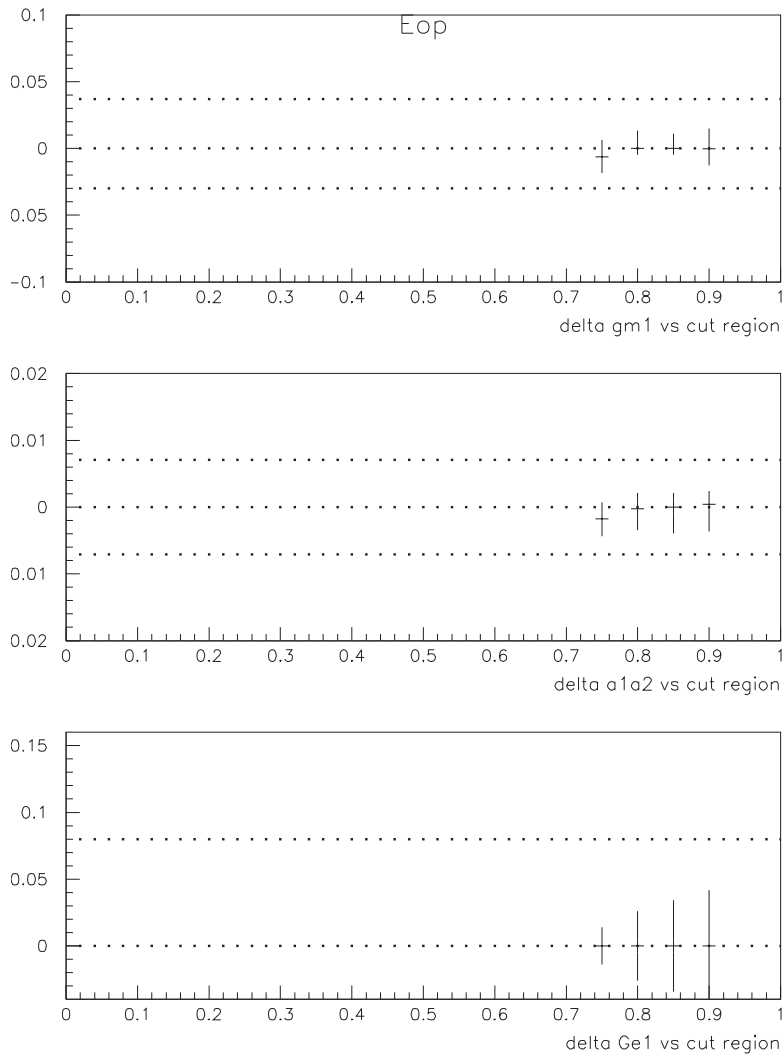


Figure 9.11: Fit parameter shift S vs. Pion Energy/Momentum Cut (c)
 (from top to bottom): \tilde{g}_{M1} , $\frac{a_1}{a_2}$, G_{E1}
 Dotted lines are nominal data stat errors (table 8.1), included for scale.

Varied Analysis Cut	$\sigma_{\tilde{g}_{M1}}$	$\sigma_{\frac{a_1}{a_2}}$	$\sigma_{G_{E1}}$
Fusion χ^2	0.0	0.0	0.0
Inner CsI Ring	0.0	0.0	0.0
Outer CsI Ring	0.0	0.0	0.0
P_t^2	0.012	0.0	0.0
pp0kine	0.0	0.0	0.0
P_{Kaon}	0.029	0.0	0.0
Track- γ sep	0.0	0.0	0.0
Vertex Z	0.034	0.0056	0.0
$E_\gamma^{(lab)}$	0.054	0.0077	0.0
pion E/p	0.0	0.0	0.0

Table 9.6: Systematic errors assigned from the variation of cuts

9.4.1 Fraction of Background in the $K_L \rightarrow \pi^+\pi^-\gamma$ Event Sample

To determine the size of the background, the combined $\pi^+\pi^-\gamma$ invariant mass was plotted with all cuts applied except the kaon mass cut. The distribution to the left and right of the events accepted in the final sample were fit with an exponential (i.e. a straight line on the log plot) to estimate the size of the background underneath the kaon mass peak.

The left-side wing fit predicted 789 background events inside the kaon mass cut, and the right-side wing fit predicted 618 events. Therefore, based on a final event size of $N_d = 112,140$ final events, this leads to a background of roughly 0.55% - 0.70%.

9.4.2 Effect of the Background on the Final Fit Result

Since the data was fit event by event (as opposed to a general histogram distribution), background subtraction was not possible. Therefore, it was necessary to determine to what extent the background in the event sample affected the final fit result.

MC Input	\tilde{g}_{M1}	$\frac{a_1}{a_2}$	G_{E1}
sample 1 shift	0.0325	0.0065	0.036
sample 2 shift	0.0339	0.0067	0.037
sample 3 shift	0.0355	0.0062	0.045
max shift	0.0355	0.0067	0.045
syst error assigned	0.0355	0.0067	0.045

Table 9.7: Effect of the addition of 800 wing events to the final data sample

To do this, instead of subtracting out the background, additional background events (from the wing regions) were added to the final event sample in order to simulate the effect of the existing background. 2400 wing-region events were divided into 3 independent 800-event samples, so that each sample contained slightly more events than the upper limit of the background estimate (789 events).

Each of the three samples were then separately combined with the nominal data sample and the combined samples were refit with the likelihood code. The deviation between the fit results for the nominal data sample (with no background added) and the fit results for each of the three wing-event-added sample was recorded. The background systematic error for each fit parameter (\tilde{g}_{M1} , $\frac{a_1}{a_2}$, G_{E1}) was determined as the maximum deviation out of the three trials. The results are summarized in table 9.7.

9.4.3 Contributions to the Background

The vast majority of background events are believed to come from the following four modes: $K_L \rightarrow \pi^+\pi^-\pi^0$, $K_L \rightarrow \pi^+\pi^-$, K_{e3} ($K_L \rightarrow \pi e \nu$), and $K_{\mu 3}$ ($K_L \rightarrow \pi \mu \nu$)

The $K_L \rightarrow \pi^+\pi^-\pi^0$ decay (where $\pi^0 \rightarrow \gamma\gamma$) was by far the primary target for background suppression in the analysis and was responsible for the rise to the left of the $K_L \rightarrow \pi^+\pi^-\gamma$ invariant mass in figure 9.12. Events from this decay can be mistaken for $K_L \rightarrow \pi^+\pi^-\gamma$ events when one photon was lost and/or when both pho-

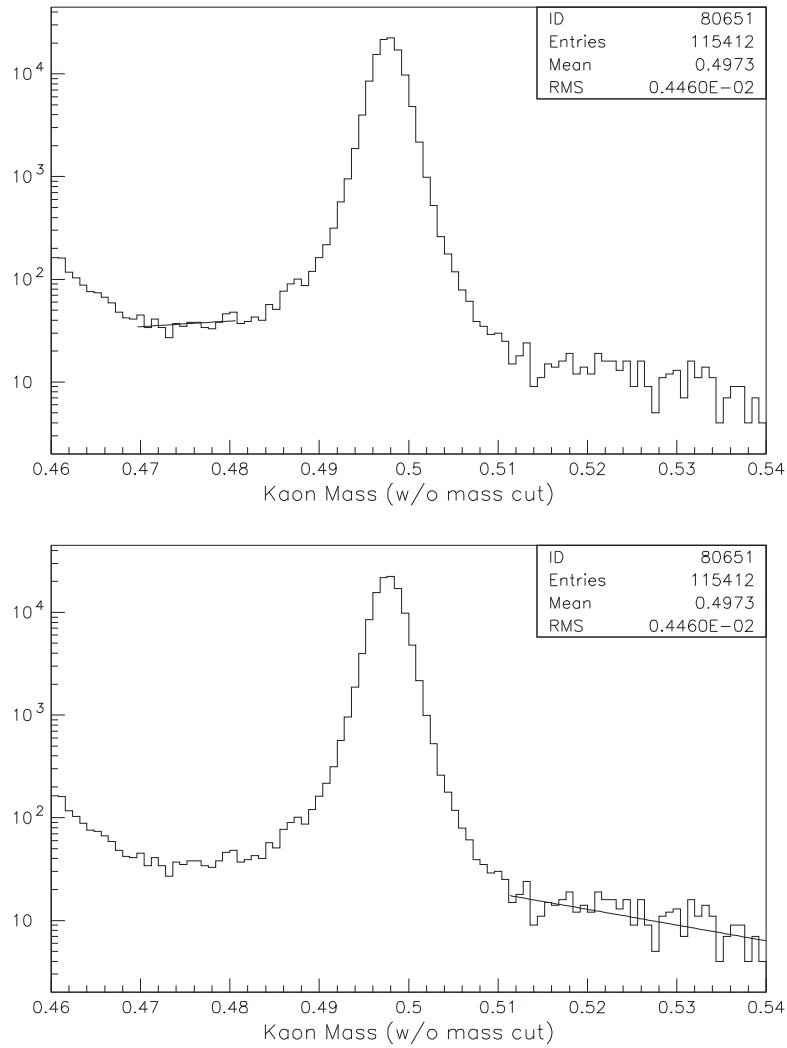


Figure 9.12: Left wing and right wing exponential fits to data. Plot is $\log(N_{events}/0.8 \text{ MeV})$ vs. $M_{\pi^+\pi^-\gamma}$ (GeV). The nominal kaon mass cuts are inhibited.

tons are lost and an accidental photon was reconstructed in their place. Although these types of events were heavily suppressed by the photon vetoes, the transverse momentum cut, and the kaon mass cut, the high $K_L \rightarrow \pi^+\pi^-\pi^0$ branching ratio ($\sim 2800 \times \Gamma_{K_L \rightarrow \pi^+\pi^-\gamma}$) still makes these events a fairly serious issue. Fortunately, the so-called “pp0kine” cut which cuts on the kinematics of this decay (see section 5.4.3) has proven highly successful in suppressing the $\pi^+\pi^-\pi^0$ background down to the size of the other backgrounds.

To verify the effectiveness of the $\pi^+\pi^-\pi^0$ suppression, a Monte Carlo sample equivalent to roughly one quarter of the net $K_L \rightarrow \pi^+\pi^-\pi^0$ flux present in the data was generated. This sample (consisting of ≈ 3 billion generated events!) took 2-3 months to generate, crunch (twice!), and filter.

Out of the 3 billion events, only 30 ± 6 events survived all analysis cuts! Scaling this up by a factor of 4 leads to an estimate of 120 ± 24 $K_L \rightarrow \pi^+\pi^-\pi^0$ background events in the final $\pi^+\pi^-\gamma$ event sample– a real testament to the effectiveness of the “pp0kine” cut!

Monte Carlo was also generated to examine the effect of events from the $K_L \rightarrow \pi^+\pi^-$ decay channel, which can be a background to $K_L \rightarrow \pi^+\pi^-\gamma$ when the two pions are combined with an accidental photon. Since the $K_L \rightarrow \pi^+\pi^-$ branching ratio is only about ~ 50 x that of $K_L \rightarrow \pi^+\pi^-\gamma$, it was possible to generate a fairly large sample ($\sim 80\%$ of the equivalent of a full data flux) of $K_L \rightarrow \pi^+\pi^-$ events to study. However, by the same token, the relatively small branching ratio also made it an unlikely candidate to be a major contributor to the background after kaon mass and transverse momentum suppression cuts were applied.

After all analysis cuts were applied to the $K_L \rightarrow \pi^+\pi^-$ Monte Carlo sample, a grand total of 1 ± 1 events remained. Scaling this up to a full flux leads to an estimate of 1.25 ± 1.25 $K_L \rightarrow \pi^+\pi^-$ background events.

The remaining ~ 600 events in the background are primarily due to the semi-leptonic modes, K_{e3} and $K_{\mu3}$. Events from these modes become background to $K_L \rightarrow \pi^+\pi^-\gamma$ when the charged lepton (the electron for K_{e3} and the muon for $K_{\mu3}$) is misidentified as a pion and an accidental photon is reconstructed in place of the neutrino⁴. Although these modes are highly suppressed by e.g. the kaon mass cut, the Energy/momentum cut, the muon vetoes, and the transverse momentum cut, they are nevertheless relevant because they have branching ratios that are $\sim 6000\text{-}9000$ x that of the signal mode (i.e. 2-3x higher, even, than $\Gamma_{K_L \rightarrow \pi^+\pi^-\pi^0}$).

Therefore a $\sim 10^{-8}$ suppression of the semi-leptonic modes would still allow sufficient event acceptance to account for the remaining background events observed from wing extrapolations.

9.5 Effects of Variations over Time

Since the 1997 data was taken over a time span of roughly three months, it was important to determine whether the measurement of the parameter values shifted over the course of the run.

To investigate this, the data was divided into three temporally consecutive and statistically independent subsamples (each one containing roughly a month's-worth of data running), and then plotted in figure 9.13. Since the observed parameter shifts of the three subsamples were all within statistical fluctuations, no systematic error was assigned for this effect.

⁴note that the neutrino is always unreconstructed, since the KTeV detector is not designed to detect neutrinos

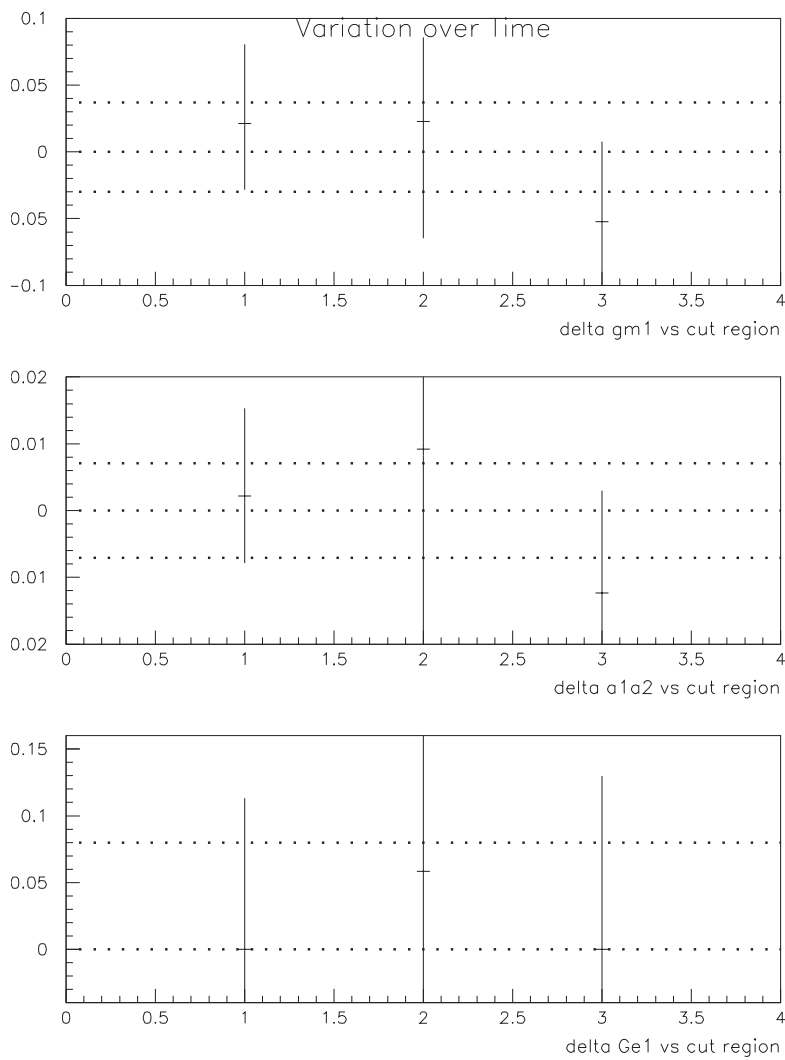


Figure 9.13: Variation of Parameter Values Over the Course of the 1997 Run

9.6 Effects of K_S Contamination

Since events with high kaon momentum (> 160 GeV) were excluded from the final event sample, K_S events were expected to only have a very minimal effect on the final answer. This assumption was tested using a $K_L \rightarrow \pi^+\pi^-\gamma$ Monte Carlo recently developed by M. Ronquest [41] for direct CP Violation studies that code allows the user to explicitly control K_L and K_S mixing during generation.

A total of 40 data-sized Monte Carlo files were generated using this Monte Carlo, 20 of which were pure- K_L samples and 20 of which include full K_L , K_S mixing. All 40 samples were generated at the same parameter values ($\tilde{g}_{M1} = 1.19$, $\frac{a_1}{a_2} = -0.740$, and $G_{E1} = 0.01$) and then run through the standard analysis and likelihood fit procedures in place of data.

The twenty pure- K_L samples were averaged together and the twenty K_L , K_S mixed samples were averaged together. The shift between the two mean values (S) was then interpreted as the size of the K_S contribution to the final result. That is:

$$S = | \langle X_{K_L} \rangle - \langle X_{Mix} \rangle | \quad (9.3)$$

where X_{K_L} is the best fit value of a given fit parameter “X” ($X = \{ \tilde{g}_{M1}, \frac{a_1}{a_2}, G_{E1} \}$) for a pure- K_L sample, and X_{Mix} is the corresponding quantity for a K_L , K_S mixed sample.

The statistical fluctuation on the shift (σ_S) is given by

$$\sigma_S = \sqrt{\sigma_{\langle X_{K_L} \rangle}^2 + \sigma_{\langle X_{Mix} \rangle}^2} \quad (9.4)$$

where

$$\sigma_{\langle X_{K_L} \rangle}^2 = \frac{\sigma_{X_{K_L}}^2}{N} \quad \text{and} \quad \sigma_{\langle X_{Mix} \rangle}^2 = \frac{\sigma_{X_{Mix}}^2}{N}$$

So equation (9.4) becomes

$$\sigma_S = \sqrt{\frac{\sigma_{X_{K_L}}^2}{N} + \frac{\sigma_{X_{Mix}}^2}{N}} \quad (9.5)$$

	\tilde{g}_{M1}	$\frac{a_1}{a_2}$	G_{E1}
$S \equiv \langle X_{K_L} \rangle - \langle X_{Mix} \rangle $	0.007	0.0019	0.013
$\sigma_{\langle X_{K_L} \rangle}$	0.009	0.0014	0.013
$\sigma_{\langle X_{Mix} \rangle}$	0.010	0.0021	0.012
σ_S	0.013	0.0025	0.018
Systematic Error Assigned (ΔS)	0.0	0.0	0.0

Table 9.8: Summary of kaon contamination study results

where $N = 20$ in this particular case. The results of the study are summarized in table 9.8.

Since the observed shift between the mean values was within statistical fluctuations for all three fit parameters, the effect of K_S contamination on the final answer was deemed negligible within the range of statistical sensitivity, and a systematic error of $\Delta S = 0.0$ was assigned for each of the three parameters.

9.7 Uncertainties on Constant Parameters Input In the Matrix Element

The accuracy of the Matrix Element Probability Function depends critically upon the accuracy of parameter values measured by previous experiments, such as η_{+-} , that are input as constants into the expression for the differential decay rate (equations 1.48 and 1.52).

The largest errors arise from the uncertainty on the measurements of η_{+-} and the $\pi^+\pi^-$ phase shifts, δ_0^0 and δ_1^1 . The effect of these uncertainties on the final answer was ascertained by generating new “baseline” Monte Carlo with the same fit parameter values as the nominal ($\tilde{g}_{M1} = 1.20$, $\frac{a_1}{a_2} = -0.737$, $G_{E1} = 0.04$), but with a given input parameter (η_{+-} , δ_0^0 , δ_1^1) increased or decreased by 1σ .

9.7.1 Effect of the Uncertainty in η_{+-}

The amplitude of the Inner Bremsstrahlung term in equation 1.48 is proportional to the CP-Violation parameter η_{+-} , where η_{+-} is defined as

$$\eta_{+-} = \epsilon \left(1 + \frac{\epsilon'}{\epsilon} \right) \approx \epsilon \quad (9.6)$$

and $\epsilon = (2.282 + / - 0.017) \times 10^{-3}$ [42]

The effect that this uncertainty in the η_{+-} value had on the final measurement of the fit parameters $(\tilde{g}_{M1}, \frac{a_1}{a_2}, G_{E1})$ was determined by generating new “baseline” Monte Carlos identical to the nominal baseline, except with η_{+-} shifted by $\pm 1\sigma$.

The data was then refit with these new Monte Carlos and the maximum observed shifts for each fit parameter from the nominal data fit was interpreted as the effect of the η_{+-} uncertainty on the final answer. These maximum shifts were then compared to the expected statistical fluctuation on Monte Carlo files that differed only by a random seed (see table 9.1), and any shift greater than the statistical fluctuation was assigned as the systematic error due to uncertainty in η_{+-} . The result is summarized in table 9.9.

9.7.2 Effect of the Uncertainty in the Pion Phase Shifts

The expressions for the pion scattering phase shifts $\delta_0^0(M_X^2)$ and $\delta_1^1(M_{\pi\pi}^2)$ in the $K_L \rightarrow \pi^+\pi^-\gamma$ differential decay rate are calculated using the Colangelo et al. parameterization [43], which can be summarized for a particle of mass M_X as

$$\tan \delta_0^0(M_X^2) = \sqrt{1 - \frac{4M_\pi^2}{M_X^2}} (A_0^0 + B_0^0 q^2 + \dots) \left(\frac{4M_\pi^2 - s_0^0}{M_X^2 - s_0^0} \right) \quad (9.7a)$$

$$\tan \delta_1^1(M_X^2) = \sqrt{1 - \frac{4M_\pi^2}{M_X^2}} [(q^2)(A_1^1 + \dots)] \left(\frac{4M_\pi^2 - s_1^1}{M_X^2 - s_1^1} \right) \quad (9.7b)$$

where

$$q^2(M_X^2) = \frac{1}{4} \left(\frac{M_X^2}{M_\pi^2} \right) - 1 \quad (9.8)$$

$$\begin{aligned} A_0^0 &= 0.220 + / - 0.005 \\ B_0^0 &= 0.268 + / - 0.006 & s_0^0 &= 36.77 M_\pi^2 \\ A_1^1 &= 0.0379 + / - 0.0005 & s_1^1 &= 30.72 M_\pi^2 \end{aligned}$$

By varying the constants A_0^0 and B_0^0 in equation 9.7 by 1σ in either direction and looking for the maximum deviation, the error in $\delta_0^0(M_K^2)$ can be expressed as

$$\delta_0^0(M_K^2) = 0.684 \pm 0.012 \quad (9.9)$$

However, since $M_{\pi\pi} = M_K(M_K - 2\omega)$, $M_{\pi\pi}$ is intrinsically a function of the phase space variable ω (the photon energy in the kaon center of mass frame), it was therefore not possible to compute a single value for δ_1^1 in the same way as δ_0^0 .

As a result, the “baseline” Monte Carlo was varied by $\delta_1^1 = \delta_1^1(M_{\pi\pi}, A_1^1 \pm \sigma_{A_1^1})$, rather than trying to calculate δ_1^1 and $\sigma_{\delta_1^1}$ explicitly.

A systematic error due to changes in δ_0^0 and δ_1^1 is assigned in a manner totally analogous to the method described for η_{+-} . Table 9.9 summarizes the results for all three Monte Carlo input quantities (δ_0^0 , δ_1^1 , and η_{+-}).

9.8 Uncertainty in Event Reconstruction Resolution

A very good estimate of the effect that detector reconstruction resolution has on the final fit values can be obtained by fitting a given Monte Carlo sample twice: once using the generated (“MCLIST”) values of the phase space variables (ω , $\cos\theta$) and once using the values produced after event reconstruction for each event.

This type of fit was done on the same sets of Monte Carlo used in section 8.3 in the previous chapter. An average and standard deviation for the MCLIST fits

Monte Carlo Input Parameter	\tilde{g}_{M1}	$\frac{a_1}{a_2}$	G_{E1}
$\delta_0^0 + \sigma_{\delta_0^0}$ shift	0.0111	0.00209	0.0000
$\delta_0^0 - \sigma_{\delta_0^0}$ shift	0.0031	0.00052	0.0000
$\delta_1^1(A_1^1 + \sigma_{A_1^1})$ shift	0.0000	0.00040	0.0000
$\delta_1^1(A_1^1 - \sigma_{A_1^1})$ shift	0.0053	0.00049	0.0000
$\eta_{+-} + \sigma_{\eta_{+-}}$ shift	0.0171	0.00136	0.0000
$\eta_{+-} - \sigma_{\eta_{+-}}$ shift	0.0017	0.00114	0.0000
<hr/>			
δ_0^0 max deviation	0.0111	0.00209	0.0000
δ_1^1 max deviation	0.0053	0.00049	0.0000
η_{+-} max deviation	0.0171	0.00136	0.0000
<hr/>			
δ_0^0 syst error assigned	0.0111	0.00209	0.0000
δ_1^1 syst error assigned	0.0053	0.00000	0.0000
η_{+-} syst error assigned	0.0171	0.00136	0.0000

Table 9.9: Effect of the uncertainty of Monte Carlo input constants on the final result

and then a second average and standard deviation for the reconstructed fits was computed for each given set (see tables 9.10 and 9.11). The shift in the average value of a fit parameter can then be interpreted as a systematic error due to uncertainty in event reconstruction. Note that because the reconstructed values are used throughout analysis and event selection (i.e. the MCLIST values are only looked up just before they are output to the likelihood fit program), both the MCLIST fit and the reconstructed fit use an identical set of events. This ensures that the observed parameter shifts were due solely to the choice of MCLIST or reconstructed values for the phase space variables.

9.9 Summary of Systematic Errors

The complete list of systematic error study results is summarized in table 9.12. Significant contributors to the net systematic error included the errors in the likelihood fit procedure, reconstruction of the phase space variable values, background

MC	Fit Ave (MCLIST)			Fit Ave (Recon)			Shift		
	\tilde{g}_{M1}	$\frac{a_1}{a_2}$	G_{E1}	\tilde{g}_{M1}	$\frac{a_1}{a_2}$	G_{E1}	$ \Delta_{\tilde{g}_{M1}} $	$ \Delta_{\frac{a_1}{a_2}} $	$ \Delta_{G_{E1}} $
set 1	1.207	-0.7314	0.055	1.228	-0.7324	0.017	0.021	0.0010	0.038
set 2	1.056	-0.7728	0.053	1.078	-0.7694	0.016	0.022	0.0034	0.037
set 3	1.216	-0.7353	0.024	1.238	-0.7322	0.005	0.022	0.0031	0.019
set 4	1.071	-0.7565	0.023	1.094	-0.7523	0.003	0.023	0.0042	0.020
Max Dev	-	-	-	-	-	-	0.023	0.0042	0.038
Syst Err	-	-	-	-	-	-	0.023	0.0042	0.038

Table 9.10: Deviation between generated and reconstructed parameter values for a given Monte Carlo file. Monte Carlo sample sets are the same as those used in table 8.3.

MC	Fit Ave (MCLIST)			Fit Ave (Recon)			σ_{shift}		
	$\sigma_{\langle\tilde{g}_{M1}\rangle}$	$\sigma_{\langle\frac{a_1}{a_2}\rangle}$	$\sigma_{\langle G_{E1}\rangle}$	$\sigma_{\langle\tilde{g}_{M1}\rangle}$	$\sigma_{\langle\frac{a_1}{a_2}\rangle}$	$\sigma_{\langle G_{E1}\rangle}$	\tilde{g}_{M1}	$\frac{a_1}{a_2}$	G_{E1}
1	0.005	0.0012	0.009	0.005	0.0009	0.004	0.007	0.0015	0.010
2	0.005	0.0016	0.009	0.005	0.0014	0.004	0.007	0.0021	0.010
3	0.010	0.0023	0.008	0.010	0.0021	0.003	0.014	0.0031	0.009
4	0.007	0.0018	0.008	0.007	0.0017	0.002	0.010	0.0025	0.008

Table 9.11: Statistical errors on the four trial Monte Carlo sets from table 9.10

effects, and analysis cut selections for the lab photon energy, kaon momentum, and Z vertex.

systematic	$\sigma_{\tilde{g}_{M1}}$	$\sigma_{\frac{a_1}{a_2}}$	$\sigma_{G_{E1}}$
Baseline MC Bias	0.0093	0.0021	0.013
Kaon Momentum Slope	0.0031	0.0004	0.005
Background	0.0355	0.0067	0.045
Fusion χ^2	0.0	0.0	0.0
Inner CsI Ring	0.0	0.0	0.0
Outer CsI Ring	0.0	0.0	0.0
P_t^2	0.012	0.0	0.0
pp0kine	0.0	0.0	0.0
P_{Kaon}	0.029	0.0	0.0
Track- γ sep	0.0	0.0	0.0
Vertex Z	0.034	0.0056	0.0
$E_\gamma^{(lab)}$	0.054	0.0077	0.0
pion E/p	0.0	0.0	0.0
Time (run #)	0.0	0.0	0.0
K_S contamination	0.0	0.0	0.0
Likelihood Fitter	0.014	0.0056	0.024
$(\omega, \cos \theta)$ reconstruction	0.023	0.0042	0.038
η_{+-} in MC	0.0171	0.0014	0.000
δ_0^0 phase in MC	0.0111	0.0021	0.000
δ_1^1 phase in MC	0.0053	0.0000	0.000
Net Systematic Error	0.087	0.014	0.065

Table 9.12: Summary of Systematic Errors

Chapter 10

Conclusion

The E1 contribution to the $K_L \rightarrow \pi^+\pi^-\gamma$ decay proved to be beyond the sensitivity of this measurement. As a result, the magnitude of the g_{E1} amplitude was reported as the 90% confidence level upper limit

$$|g_{E1}| < 0.14 \text{ (90\% CL) (stat, syst combined).}$$

This result and the companion UVa search¹ for the E1 transition in the 1999 $K_L \rightarrow \pi^+\pi^-e^+e^-$ decay data [44] are the first experimentally measured upper limits for this parameter.

In addition to the $|g_{E1}|$ upper limit, the two M1 form factor parameters, \tilde{g}_{M1} and $\frac{a_1}{a_2}$, were also measured to a high degree of precision. The results for these two parameters are as follows:

$$\tilde{g}_{M1} = 1.229 \pm 0.035 \text{ (stat)} \pm 0.087 \text{ (syst)}$$

$$\frac{a_1}{a_2} = -0.733 \pm 0.007 \text{ (stat)} \pm 0.014 \text{ (syst)}$$

¹completed in parallel with this analysis

The measurement of $\frac{a_1}{a_2}$ agrees well with the result from the previously published KTeV $K_L \rightarrow \pi^+\pi^-\gamma$ decay measurement [45]. That result, obtained from ~ 8600 events in the 1996 E832 data, produced the following value of $\frac{a_1}{a_2}$:

$$\frac{a_1}{a_2} = -0.737 \pm 0.026 \text{ (stat)} \pm 0.022 \text{ (syst)}$$

Moreover, both the \tilde{g}_{M1} and $\frac{a_1}{a_2}$ form factors are in very good agreement with the numbers published by KTeV from the analysis of the closely related $K_L \rightarrow \pi^+\pi^-e^+e^-$ decay² during the 1997 E799 experiment [46]:

$$\tilde{g}_{M1} = 1.35_{-0.17}^{+0.20} \text{ (stat)} \pm 0.04 \text{ (syst)}$$

$$\frac{a_1}{a_2} = -0.720 \pm 0.028 \text{ (stat)} \pm 0.009 \text{ (syst)}$$

²i.e. $K_L \rightarrow \pi^+\pi^-\gamma^*$, where γ^* is a virtual photon

Appendix A

Expressing the $\pi^+\pi^-$ Invariant Mass as a Function of the Phase Space Variable ω

To see that $M_{\pi\pi} = M_{\pi\pi}(\omega)$, where ω is defined to be the photon energy in the kaon COM, we can invoke the invariance of the kaon 4-vector momentum P:

$$P^\mu P_\mu = M_K^2 \quad (\text{A.1})$$

Expanding out the 4-vector dot product in terms of the three daughter particles,

$$(E_+ + E_- + E_\gamma)^2 - \left[\vec{k} + (\vec{p}_+ + \vec{p}_-) \right]^2 = M_K^2 \quad (\text{A.2})$$

But, using eq 1.33 and the fact that $(\vec{p}_+ + \vec{p}_-) = 0$ by definition in the $\pi^+\pi^-$ CM frame, equation A.2 reduces to

$$\left[2 \left(\frac{M_{\pi\pi}}{2} \right) + E_\gamma \right]^2 - |\vec{k}|^2 = M_K^2 \quad (\text{A.3})$$

If we now expand the first term and note that $|\vec{k}| = E_\gamma$ this becomes

$$(M_{\pi\pi}^2 + 2M_{\pi\pi}E_\gamma + E_\gamma^2) - E_\gamma^2 = M_K^2 \quad (\text{A.4})$$

Finally, plugging in equation 1.36 for E_γ and simplifying, equation A.4 becomes

$$M_{\pi\pi}^2 = M_K^2 - 2\omega M_K \quad (\text{A.5})$$

Or, equivalently,

$$\omega = \frac{M_K^2 - M_{\pi\pi}^2}{2M_K} \quad (\text{A.6})$$

Appendix B

The Statistical Error on a Correlated Sample

Consider a situation where the data sample (\equiv sample “ S_0 ”), which has N_0 events after all nominal cuts have been applied, has a particular cut tightened such that a new sample (“ S_1 ”) with N_1 final events (where $N_1 < N_0$) is produced. The statistical uncertainty on the S_1 sample ($\equiv \sigma_1$) is then calculated. However, the subtlety here is that, since the S_0 and S_1 samples are correlated, the expected statistical change in transforming from S_0 to S_1 must be less than σ_1 .

To calculate the correct error on the shift of a value between the two correlated samples (S_0 and S_1), we define a third set of events (“ S_ϵ ”) such that $S_\epsilon \cap S_1 = 0$ and hence $N_\epsilon \equiv N_0 - N_1$. This means that subsamples S_ϵ and S_1 are statistically independent, and hence the standard relations will apply.

In other words, if a given fit parameter “ α ” is measured to be $\alpha = \alpha_0$ using the nominal (S_0) data events, but is measured to be $\alpha = \alpha_1$ using the tighter-cut S_1 events, then there is a shift $\delta \equiv \alpha_0 - \alpha_1$, and we need to determine the statistical error (σ_δ) on this shift in terms of σ_0 and σ_1 . In order to do this, however, we must first rewrite the shift δ in terms of the independent samples S_1 and S_ϵ .

B.0.1 Expressing the Parameter Shift in Terms of Statistically Independent Samples

To do this, we define weights for each of the three samples such that

$$w_0 = \frac{1}{\sigma_0^2} \quad (\text{B.1a})$$

$$w_1 = \frac{1}{\sigma_1^2} \quad (\text{B.1b})$$

$$w_\epsilon = \frac{1}{\sigma_\epsilon^2} \quad (\text{B.1c})$$

where

$$w_0 = w_1 + w_\epsilon \quad (\text{B.2})$$

The nominal fit value α_0 can then be expressed as a weighted average

$$\alpha_0 = \frac{\alpha_1 w_1 + \alpha_\epsilon w_\epsilon}{w_1 + w_\epsilon} \quad (\text{B.3})$$

and hence the shift δ can be written

$$\delta \equiv \alpha_0 - \alpha_1 = \frac{\alpha_1 w_1 + \alpha_\epsilon w_\epsilon}{w_1 + w_\epsilon} - \alpha_1 \quad (\text{B.4})$$

Combining the two terms with a common denominator gives

$$\delta = \frac{\alpha_1 w_1 + \alpha_\epsilon w_\epsilon - (\alpha_1 w_1 + \alpha_1 w_\epsilon)}{w_1 + w_\epsilon} \quad (\text{B.5})$$

cancelling like terms, this reduces to

$$\delta = \frac{w_\epsilon}{w_1 + w_\epsilon} (\alpha_\epsilon - \alpha_1) \quad (\text{B.6})$$

Plugging equations B.1 back in for the weights, we get

$$\delta = \left(1 + \frac{\sigma_\epsilon^2}{\sigma_1^2}\right)^{-1} (\alpha_\epsilon - \alpha_1) \quad (\text{B.7})$$

But, from equations B.1 and B.2 we can also show that

$$\sigma_\epsilon^2 = \frac{\sigma_0^2 \sigma_1^2}{\sigma_1^2 - \sigma_0^2} \quad (\text{B.8})$$

So, substituting B.8 into B.7 and rearranging, we end up with

$$\delta = \gamma(\alpha_\epsilon - \alpha_1) \quad (\text{B.9})$$

where

$$\gamma \equiv 1 - \frac{\sigma_0^2}{\sigma_1^2} \quad (\text{B.10})$$

B.0.2 Calculation of the Error on the Shift

To find the error on the shift, we first note that the error ΔF for any arbitrary $F = F(A, B)$ can be written¹

$$\Delta F = \left[\left(\frac{\partial F}{\partial A} \right)^2 (\Delta A)^2 + \left(\frac{\partial F}{\partial B} \right)^2 (\Delta B)^2 \right]^{\frac{1}{2}} \quad (\text{B.11})$$

Therefore, for the specific case of $\delta = \delta(\alpha_\epsilon, \alpha_1)$, given by equation B.9, we can write

$$\sigma_\delta = \gamma \left[(1)(\sigma_\epsilon^2) + (1)(\sigma_1^2) \right]^{\frac{1}{2}} \quad (\text{B.12})$$

As an aside, note that γ was treated as a constant during the differentiation. To justify this, recall that for any sample of size N , $\sigma_N^2 = \frac{\bar{\sigma}^2}{N}$ where $\bar{\sigma}$ is the error on one event.

Therefore $\sigma_0^2 = \frac{\bar{\sigma}^2}{N_0}$ and $\sigma_1^2 = \frac{\bar{\sigma}^2}{N_1}$, and hence equation B.10 can be written

$$\gamma = 1 - \frac{\frac{\bar{\sigma}^2}{N_0}}{\frac{\bar{\sigma}^2}{N_1}} = 1 - \frac{N_1}{N_0} \quad (\text{B.13})$$

which is a constant for any given N_0 and N_1 .

We now use equations B.10 and B.8 to reexpress equation B.12 as

$$\sigma_\delta = \left(1 - \frac{\sigma_0^2}{\sigma_1^2} \right) \left[\left(\frac{\sigma_0^2 \sigma_1^2}{\sigma_1^2 - \sigma_0^2} \right) + \sigma_1^2 \right]^{\frac{1}{2}} \quad (\text{B.14})$$

¹assuming that A and B are statistically independent variables

Combining terms under a common denominator,

$$\sigma_\delta = \left(\frac{\sigma_1^2 - \sigma_0^2}{\sigma_1^2} \right) \left(\frac{\sigma_1^2}{\sqrt{\sigma_1^2 - \sigma_0^2}} \right) \quad (\text{B.15})$$

which simplifies to our final expression of

$$\sigma_\delta = \sqrt{\sigma_1^2 - \sigma_0^2} \quad (\text{B.16})$$

Bibliography

- [1] J. Christenson et al. *Phys Rev. Lett.* **13**, 138. (1964)
- [2] F. Halzen and A. Martin. *Quarks and Leptons*. John Wiley & Sons Inc, 1984.
- [3] M. Gell-Mann and A. Pais. *Phys Rev.* **97**, 1387. (1955)
- [4] Q. Ho-Kim and X. Pham. *Elementary Particles and Their Interactions*. Springer-Verlag, 1998.
- [5] R. Sachs. *The Physics of Time Reversal*. The University of Chicago Press, 1987.
- [6] Y.C.R Lin and G. Valencia. *Phys Rev.* **D37**, 143. (1988).
- [7] L.M. Sehgal and M. Wanninger. *Phys Rev.* **D46**, 1035. (1992).
- [8] L.M. Sehgal and P. Heiliger. *Phys Rev.* **D48**, 4146. (1993).
- [9] M. Peskin and D. Schroeder. *An Introduction to Quantum Field Theory*. Westview Press, 1995.
- [10] B. DeWit. *Field Theory in Particle Physics*. Elsevier Science, 1986.
- [11] L.M. Sehgal and J. van Leusen. *Phys Rev. Lett.* **83**, 4983. (1999).
- [12] J. Tandean and G. Valencia. *Phys Rev.* **D62**, 116007. (2000).

- [13] K. Hanagaki. PhD Thesis, Osaka University, 1998.
- [14] V. Bocean et al. Technical Report TM-2046, Fermilab, 1998.
- [15] A. Roodman. The KTeV Pure CsI Calorimeter. *Proceedings of the VII International Conference on Calorimetry, Tucson, Arizona*. World Scientific, 1998.
- [16] P. Shawhan. PhD Thesis, University of Chicago, 2000.
- [17] J. Hamm. PhD Thesis, University of Arizona, 2002.
- [18] J. Graham. PhD Thesis, University of Chicago, 2001.
- [19] G.B. Quinn. PhD Thesis, University of Chicago, 2000.
- [20] E. Zimmerman, PhD Thesis, University of Chicago, 1999.
- [21] R. Yarema et al. KTeV Internal Note # 203, 1994.
- [22] T. Barker, P. Mikelson. KTeV Internal Note # 198, 1994.
- [23] P. Mikelson. KTeV Internal Note # 347, 1995.
- [24] C. Bown, E. Cheu. KTeV Internal Note # 240, 1994.
- [25] P. Mikelson. PhD Thesis, University of Colorado, 1999.
- [26] P. Shawhan. KTeV Internal Note # 257, 1994.
- [27] C. Bown et al. *Nucl. Instrum. Metho.* **B412**, 248. (1996).
- [28] C. Bown et al. KTeV Internal Note # 487, 1997.
- [29] V. O'Dell, T. Yamanaka. KTeV Internal Note # 184, 1994.
- [30] P. Shawhan, R. Kessler. KTeV Internal Note # 210, 1994.

- [31] I. Albuquerque et al. KTeV Internal Note # 318, 1995.
- [32] T. Alexopoulos et al. KTeV Internal Note # 207, 1994.
- [33] R. Kessler. $K_L \rightarrow \pi^+\pi^-\gamma$ *Level 3, Crunch, and MC*. KTeV Internal Document, January, 2003.
- [34] A.J. Malensek. Fermilab Report FN-341, Fermilab, 1982.
- [35] A. Roodman. KTeV Internal Note # 317, 1995.
- [36] V. Prasad, PhD Thesis, University of Chicago, 2002.
- [37] R. Brun et al., *GEANT User's Guide*. CERN, Geneva (1985).
- [38] W. Press et al. *Numerical Recipes in Fortran*. Cambridge University Press, 1992.
- [39] Particle Data Group Review of Particle Physics. *Phys Rev. Lett.* **B592** (2004)
- [40] G. Feldman and R. Cousins. *Phys Rev.* **D57**, 3873. (1998).
- [41] M. Ronquest, University of Virginia. Personal Communication.
- [42] Particle Data Group Review of Particle Physics. *Phys Rev.* **D66** (2002)
- [43] G. Colangelo et al. *Nuc Phys* . **B603**, 125. (2001).
- [44] A. Golossanov, PhD Thesis, University of Virginia, 2004.
- [45] A. Alavi-Harati et al. *Phys Rev. Lett.* **86**, 761. (2001).
- [46] A. Alavi-Harati et al. *Phys Rev. Lett.* **84**, 408. (2000).